REPORT DOCUMENTATION PAGE

Form Approved
OMB NO. 0704-0188

1. AGENCY USE ONLY *(Leave blank)*	2. REPORT DATE	3. REPORT TYPE AND DATES COVERED
	Sept 96	Final 1 Mar 96 - 28 Feb 97

4. TITLE AND SUBTITLE
Workshop on Rough Surface Scattering and Related Phenomena

5. FUNDING NUMBERS
DAAH04-96-1-0039

6. AUTHOR(S)
Alexei A. Maradudin

7. PERFORMING ORGANIZATION NAMES(S) AND ADDRESS(ES)
Univ. of California
Irvine, California 92697

8. PERFORMING ORGANIZATION REPORT NUMBER

9. SPONSORING / MONITORING AGENCY NAME(S) AND ADDRESS(ES)
U.S. Army Research Office
P.O. Box 12211
Research Triangle Park,, NC 27709-2211

10. SPONSORING / MONITORING AGENCY REPORT NUMBER
ARO 35186.1-PH-CF

11. SUPPLEMENTARY NOTES
The views, opinions and/or findings contained in this report are those of the author(s) and should not be construed as an official Department of the Army position, policy or decision, unless so designated by other documentation.

12a. DISTRIBUTION / AVAILABILITY STATEMENT
Approved for public release; distribution unlimited.

13. ABSTRACT *(Maximum 200 words)*

This proposal for 15k is to support conference expenses (ground transportation, lodging and select meals) for participants attending "Workshop on Rough Surface Scattering and Related Phenomena," to be held in Napa Valley, California, June 24-27, 1996. It is intended that there be no more than about 25 participants.

The topics to be covered in this workshop fall into three categories. The first is the direct scattering problem: given a rough surface, what is the scattered field? The surface in question can bound a homogeneous medium or, more interestingly, an inhomogeneous medium. Reports on new physical phenomena in scattering from such surfaces, as well as methodological advances in calculations of this scattering, will be sought.

The second category is the inverse scattering problem: given some kind of (specified) scattering data, can one reconstruct the surface from which the scattering occurred, or can one extract information about the statistical properties of the surface (e.g. the power spectrum of a randomly rough surface)? Again, reports on methodological advances will be sought.

The third topic is near-field optical microscopy, with an emphasis on the possibilities of resolving surface structures, topographical and/or optical, with dimensions much smaller than the wavelength of the incident light.

14. SUBJECT TERMS	15. NUMBER IF PAGES
Rough Surface Scattering	16. PRICE CODE

17. SECURITY CLASSIFICATION OR REPORT	18. SECURITY CLASSIFICATION OF THIS PAGE	19. SECURITY CLASSIFICATION OF ABSTRACT	20. LIMITATION OF ABSTRACT
UNCLASSIFIED	UNCLASSIFIED	UNCLASSIFIED	UL

Workshop on Rough Surface Scattering and Related Phenomena

Napa Valley Lodge, Yountville, California
June 23-June 28, 1996

Supported by:

Army Research Office
Office of Naval Research
UC Irvine Institute for Surface and Interface Science
UC Irvine School of Physical Sciences
UC Irvine Department of Physics and Astronomy

Workshop on Rough Surface Scattering and Related Phenomena
Napa Valley Lodge, Yountville, California
June 23-June 28, 1996

Monday, June 24, 1996

Session I. Chair: A. A. Maradudin

8:50 AM **Welcoming Comments**

9:00 AM **G. S. Brown** (*Virginia Polytechnic Institute*) Recent Surface Scattering Research at the Electromagnetic Interactions Laboratory

10:00 AM **P. Tran** (*Naval Air Warfare Center Weapons Division*) The Calculation of the Scattering of Electromagnetic Waves from a Two-Dimensional Surface Using the method of Ordered Multiple Interaction

11:00 AM **W. Chew** (*University of Illinois, Urbana-Champaign*) Fast Simulation of Electrogmagnetic Scattering from Two-Dimensional Random Rough Surfaces

12:00 PM **K. A. O'Donnell** (*Georgia Institute of Technology*) Observations of Scattering Effects due to Plasmon Polariton Excitation on Rough Metal Surfaces

1:00 PM **LUNCH**

Session II. Chair: A. Ishimaru

2:30 PM **J. DeSanto** (*Colorado School of Mines*) Electromagnetic Integral Equations for Rough Surface Scattering

3:30 PM **H. Ogura** (*Kyoto University*) Backscattering Enhancement and Localization Effect in the Scattering From a Random Rough Metal Surface - Stochastic Functional Approach

4:30 PM **A. A. Maradudin** (*University of California, Irvine*) X-Ray Scattering From a Randomly Rough Surface

5:30 PM **V. Freilikher** (*Bar-Ilan University*) Coherent Effects in Closed Systems with Rough Boundaries

Tuesday, June 25, 1996

Session III. Chair: M. Cheney

9:00 AM **Y. Kuga** (*University of Washington*) Detection of a Buried Target in a Random Medium Using Angular Correlation Function

10:00 AM **A. R. McGurn** (*Western Michigan University*) Speckle Correlations and Inverse Scattering Methods for 1-d and 2-d Randomly Rough Metal Surfaces

11:00 AM **D. Maystre** (*Universite D'Aix-Marseilles I*) The inverse scattering problem for rough surfaces from both deterministic and statistical points of view

12:00 PM **A. Ishimaru** (*University of Washington*) Angular, Frequency, Time and Polarization Correlations of Waves Scattered by Rough Surfaces and Applications to Surface Profile Determination and Object Detection

1:00 PM **LUNCH**

Session IV. Chair: H. Ogura

2:30 PM **Zu-Han Gu** (*Surface Optics Corporation*) Angular Correlation Function of Speckle Patterns Scattered from a One-dimensional Rough Dielectric Film on a Glass Substrate

3:30 PM **T. A. Leskova** (*Institute of Spectroscopy, Russia*) Multiple Scattering Effects in the Second Harmonic Generation of Light in Reflection from a Randomly Rough Metal Surface

Brief Presentations. Chair: W. Chew

4:30 PM **S. Mainguy** (*Centre d'Etudes Scientifiques et Techniques d'Aquitaine*) Scattering of Infrared Waves by Two-Dimensional Randomly Rough Dielectric Surfaces: Comparison Between BRDF Measurements and Numerical Simulations

4:55 PM **E. Chaikina** (*Centro de Investigacion Cientifica y Educacion Superior de Ensenada*) Diffuse Scattering from One-Dimensional Randomly Rough Metal Surfaces

5:20 PM **A. Shchegrov** (*University of California, Irvine*) Resonant Scattering of Electromagnetic Waves From a Rectangular Groove on a Perfectly Conducting Surface

5:45 PM **E. Kanzieper** (*Bar-Ilan University*) Statistics of Eigenmodes in Microwave Cavities with Rough Boundaries

Wednesday, June 26, 1996

Session V. Chair: D. Maystre

9:00 AM **M. Vaez-Iravani** (*Tencor Instruments*) Near Field Microscopy of Rough Surfaces

10:00 AM **E. R. Méndez** (*Instituto de Ciencia de Materiales de Madrid, CSIC*) Numerical Study of a Scatter-Probe Near Field Optical Microscope

11:00 AM **J.-J. Greffet** (*Ecole Centrale Paris, CNRS*) Recent Progress in the Analysis of Image Formation in Near-Field Optical Microscopy

12:00 PM **M. Nieto-Vesperinas** (*Universidad Autonoma*) Light Scattering from Bodies either in Front or Behind Corrugated Interfaces

1:00 PM **Lunch**

6:00 PM ***Reception***
7:15 PM ***Banquet***

Thursday, June 27, 1996

Session V. Chair: J. De Santo

9:00 AM **C.J.R. Sheppard** (*University of Sydney*) Scattering and Imaging of Rough Surfaces

10:00 AM **J. Sylvester** (*University of Washington*) Nonlinear and Linear Inverse Scattering

11:00 AM **M. Cheney** (*Rensselaer Polytechnic Institute*) Inverse Problems for a Perturbed Dissipative Half-Space

12:00 PM **A. Yodh** (*University of Pennsylvania*) Imaging in Optical Turbid Media with Diffuse Waves

1:00 PM **Lunch**

Brief Presentations. Chair: M. Nieto-Vesperinas

2:30 PM **A. Madrazo** (*Instituto de Ciencia de Materiales*) Electromagnetic Wave Scattering from a Body Buried Near a Random Rough Surface

2:55 PM **B. Capbern** (*Centre d'Etudes Scientifiques d'Aquitaine*) Scattering of Infrared Radiation by Heterogeneous Medium under a Rough Surface

3:20 PM **I. Novikov** (*University of California, Irvine*) The Stokes Matrix in Conical Scattering From One-Dimensional Perfectly Conducting Random Surfaces

3:45 PM **Canonical Problems -**
K. A. O'Donnell and E. R. Mendez

4:10 PM **W. A. Flood - Closing Remarks**

5:00 PM ***Wine Tasting***

Recent Surface Scattering Research at the ElectroMagnetic Interactions Laboratory

Gary S. Brown
ElectroMagnetic Interactions Laboratory
Bradley Department of Electrical Engineering
Virginia Polytechnic Institute & State University
Blacksburg, VA 24061-0111

The purpose of this presentation is to provide a brief update on some of the major surface scattering research that is being conducted by the ElectroMagnetic Interactions Laboratory (EMIL) of the Bradley Department of Electrical Engineering, Virginia Polytechnic Institute and State University. This material is specifically intended to highlight two of the most important programs of the EMIL; one deals with numerically efficient means for computing scattering from rough surfaces while the second is a multifaceted approach to understanding subsurface scattering.

Recently, researchers at EMIL [1] and Logicon-RDA [2] have developed slightly different versions of a new way to deal numerically with scattering from one-dimensional, rough, perfect electric conducting extended surface. From a physicist's point of view, the new approach is based on rearranging the integral equation for the electric current induced on the surface by the incident field in such a way that the new Born term contains a good deal of resummation of multiple scattering taking place on the surface. This same procedure is viewed by the mathematician as a preconditioning process. Regardless of the name one associates with the recasting process, the most important point is that it provides a new integral equation whose Born term is easily computed without the need to invert large matrices, its computation goes as N^2 rather than N^3, and higher iterates can be as easily computed as the Born term. N is the number of points along the surface where the current is sampled. It has also been previously shown that the Born term, while not error free, contains an element of error which is usually not large and is randomly located on the rough surface. Consequently, when averages are taken to find, for example, the incoherent scattered power, the random location of the errors on the surface tends to *reduce* the effect of the errors on the scattered power. This leads to a robustness of the Born term that is rather surprising.

Since developing what we now call the Method of Ordered Multiple Interactions (MOMI), a number of other features of the method have been investigated and these will be reported during the presentation. First, a number of computations for scattering from a sinusoidal surface have been carried out to better understand those instances when the region of interaction on the surface is considerably larger than the area illuminated by the incident field. For sinusoidal surfaces, extended regions of current support were found to coincide with the production of a Bragg line which just grazes the surface in either the forward or backward directions [3]. The Bragg line appears to give rise to "diffraction propagation" wherein the energy carried by the grazing Bragg line is reconstituted by diffraction at the peaks of the sinusoidal surface. This appears to be the source for the large region of current support on the surface, i.e., much larger than predicted by the extent of the incident field. Another important aspect of MOMI is its very robust behavior relative to convergence. There are some very well documented cases in the literature where an iterative solution of the "usual" integral equation for the current induced on a perfect conducting rough surface fails to converge. MOMI has been applied to these cases and found to converge rather rapidly without any indications of difficulty. In fact, the convergence of MOMI appears to be closely allied with the number of "back-and-forth" multiple scatterings taking place on the surface. Since there are a finite number of such scattering events on the surface, convergence is guaranteed with MOMI. Stated another way, one can say that since MOMI recasts the basic integral equation into a form that is more closely allied with the actual back-and-forth multiple scattering processes that take place on the surface and since

the number of these events *must be finite* (assuming no resonances), convergence of MOMI is guaranteed. This fact will be illustrated through an analysis of scattering by a resonant wave packet on an otherwise flat surface. Finally, we will discuss the role of current sampling density as we presently understand it. Our results to-date indicate that sampling density is dictated by the angles of incidence and scattering and the subwavelength scales of roughness on the surface. Not surprisingly, we have found that MOMI will predict the correct scattering from the surface which can be reconstructed from the samples and that as grazing incidence and backscatter is approached, the results become very sensitive to the very high frequency content of the surface roughness spectrum.

The other aspect of EMIL's current research to be discussed will be the modeling of both surface and subsurface volume scattering with particular emphasis on predicting incoherent short pulse returns from penetrable surfaces. The particular problem to be addressed is that of the incoherent scattering of a short pulse emitted by a nadir-looking radar flying above a snow covered surface [4]. In this case there are two components to the scattering process. The first is the conventional surface scattering part which may be totally characterized by a scattering cross section per unit scattering area; this quantity, in turn, may be extracted from measured data by appeal to the radar equation. The part of the scattered power that is due to the volume inhomogenieties buried in the snow is much more difficult to determine because, unlike the surface component, it cannot be so easily extracted from measured data. That is, the volume contribution not only depends upon where the scattering is coming from but also *how it got there*! Since this effect can be analytically modeled only for a few cases, we are forced into dealing with *effective parameters*. In spite of this, we have developed an incoherent short pulse scattering model which accounts for the surface scattering and the volume scattering from the subsurface snow inhomogneieties including the possibility of ice layers which are know to exist [5]. It should be emphasized that this model is not a "first principles" model; that is, it does not relate the scattered pulse shape to the detailed physical structure of the snow. Rather, it is a parameterized model which makes use of electrophysical parameters such as the scattering cross section per unit scattering area of the surface, the effective extinction coefficient of the snow volume, the scattering cross section per unit scattering volume of the snow volume, etc. The motivation for such a model is to be able to characterize the
scattering by as few parameters as possible; these parameters can then be exposed to a detailed study to see what physical processes affect them.

Having developed a model for what is causing the incoherent scattering of short pulses from snow, the next step is to expose the model to the data and determine if the results are in concert with what is known to exist in the snow. This was done for two microwave frequencies and the results will be shown to be very consistent with our physical knowledge of the snow and ice. That is, in regions of Greenland where the temperature is sufficiently high as to support melting, scattering data showed no volume scattered component. In regions where the snow is known to be very dry, the great bulk of the scattered power was attributable to volume scattering. Finally, there are regions where subsurface layers of ice (or some dielectrically denser material) appear in the scattering data.

As a final topic, the implications of this surface-volume scattering research will be discussed.

REFERENCES

1. Kapp, D.A. & G.S. Brown,"A New Numerical Method for Rough-Surface Scattering Calculations, *IEEE Trans. Antennas & Propagation,* Vol. 44, pp. 711-721, 1996.

2. Holliday, D., L.L. DeRaad & S.J. St-Cyr, "Forward-Backward: A New Method for Computing Low-Grazing Angle Scattering," *IEEE Trans. Antennas & Propagation,* Vol. 44, pp. 722-729, 1996.

3. Kapp, D.A. & G.S. Brown,"A New Method to Calculate Scattering from Rough Surfaces at Low Grazing angles," presented before the Progress in Electromagnetics Research Symposium (PIERS), Seattle, WA, 24 - 28 July, 1995.

4. Newkirk, M.H. & G.S. Brown, "A Waveform Model for Surface and Volume Scattering from Ice and Snow," *IEEE Trans. Geoscience & Remote Sensing*, Vol. 34, pp. 444 - 456, 1996.

5. Adams, R.J. & G.S. Brown,"A Model for Altimeter Returns from Penetrable Geophysical Media," to be submitted, 1996.

The Calculation of the Scattering of Electromagnetic Waves from a Two-Dimensional Surface Using the Method of Ordered Multiple Interaction

P. Tran

Code 474400D

Research and Technology Division

Naval Air Warfare Center Weapons Division

China Lake, Ca 93555

The scattering of electromagnetic radiation by a surface is often solved by the use of the Method of Moment in which the integral equation obeyed by the surface current is converted into a matrix equation. This matrix equation is then solved by inversion. Once the surface current is known, the scattered radiation can be computed. Matrix inversion scales as N^3 where N is the number of unknowns, and therefore it is limited to problem with small dimension. This practically eliminates it as a method of choice for the problem of EM waves scattering from a two-dimensional surface. An alternative to matrix inversion is iterative method such as the simple Neumann iteration which only scales as N^2. Even with the slower scaling, iterative methods still require long computation time when the scattering surface is two dimensional. Furthermore, the iterative solution can converge slowly or not at all (as in the case of the Neumann iteration for surface with large slope).

Recently, Kapp and Brown [1] introduced a reformulation of the matrix equation which they named the Method of Ordered Multiple Interaction (MOMI). Through numerical calculation of the scattering of EM waves from a one-dimensional perfectly conducting surface with slope up to 40°, they found no problem with the convergence, and the convergence is very fast; in many cases that they considered one iteration is

sufficient. The new matrix equation is obtained by breaking the original kernel **K** into a sum of a lower and an upper triangular matrix,

$$\mathbf{J} = \mathbf{J}^{inc} + \mathbf{KJ} = \mathbf{J}^{inc} + (\mathbf{U}+\mathbf{L})\mathbf{J}. \tag{1}$$

Note that the diagonal elements of **K** are zero. This equation can be rewritten as

$$\mathbf{J} = (\mathbf{I}-\mathbf{U})^{-1}(\mathbf{I}-\mathbf{L})^{-1}\mathbf{J}^{inc} + (\mathbf{I}-\mathbf{U})^{-1}(\mathbf{I}-\mathbf{L})^{-1}\mathbf{LUJ} \tag{2}$$

or

$$\mathbf{J} = (\mathbf{I}-\mathbf{L})^{-1}(\mathbf{I}-\mathbf{U})^{-1}\mathbf{J}^{inc} + (\mathbf{I}-\mathbf{L})^{-1}(\mathbf{I}-\mathbf{U})^{-1}\mathbf{ULJ}. \tag{3}$$

This new equation is then iterated. Although the inverse of (**I-U**) and (**I-L**) must be calculated for the Born term as well as for subsequent iteration, they can be done with $O(N^2)$ operations by backsubstitution. The new Born term already contains terms that describe scattering processes in which the wave is scattered continuously in one direction before being scattered again continuously in the other direction (hence the name MOMI), and therefore it is a more accurate approximation than the Born term in the regular Neumann iteration. If one needs to go beyond it, the current at the *n*th iteration is (using the eq. (3)),

$$\mathbf{J}_n = \left[(\mathbf{I}-\mathbf{L})^{-1}(\mathbf{I}-\mathbf{U})^{-1}\mathbf{UL}\right]^n(\mathbf{I}-\mathbf{L})^{-1}(\mathbf{I}-\mathbf{U})^{-1}\mathbf{J}^{inc} \tag{4}$$

With the help of the identities $\mathbf{L}(\mathbf{I}-\mathbf{L})^{-1} = (\mathbf{I}-\mathbf{L})^{-1} - \mathbf{I}$ and $(\mathbf{I}-\mathbf{U})^{-1}\mathbf{U} = (\mathbf{I}-\mathbf{U})^{-1} - \mathbf{I}$, the matrix multiplication **UL** can be eliminated, and each iteration can be done with $O(N^2)$ operations. The higher order terms have a simple physical interpretation for one-dimensional surface. The *n*th term includes all the multiple scattering processes that have up to $[1 + 2^n]$ changes in direction. From this we can see that the method should converge quickly if the dominant scattering processes on the surface are those that have few

changes in direction. For two-dimensional surface, this picture is lost because of the mapping of the surface into a one-dimensional vector destroys the meaning of direction.

In this presentation, I will describe the calculation of EM wave scattering from a perfectly conducting two-dimensional surface using the MOMI formulation. The motivation for such a calculation is the ability to study polarization effects. Since the calculation for two-dimensional surface is very time consuming, it is worthwhile to map out the convergence properties of the method as a function of the surface parameters (rms height σ and correlation length a) to optimize computation time. This is done for a gaussian random surface with gaussian correlation. Surfaces with correlation length $a \leq 3.0\lambda$ and slope, rms height/correlation length (σ/a), ≤ 1 were studied. I find that the method has no convergence difficulty except at or near $\sigma = a = 1.0\lambda$. Away from this region, convergence is achieved after 6 iterations in the worst case. I also looked at various incident angles (up to 75°) and polarization, and the convergence is quite insensitive to these parameters.

Around the resonant region ($\sigma = a = 1.0\lambda$), the method converges slowly. The scattered field fluctuates around some true value, and the amplitude of the fluctuation decreases slowly with each iteration. The fluctuation is reduced if one goes away from the resonant condition by 0.2λ in either σ or a. The fact that this problem is worst at $\sigma = a = 1.0\lambda$ is suggestive of some kind of resonance where multiple back and forth scattering is occuring (or possible shape resonance) causing the slow convergence of the method. To identify the areas that are the cause of the fluctuation, I examined the current distribution on two surfaces that have different convergent behavior. The surfaces are topologically equivalent at different roughness scale. Both surface has $a = 1.0\lambda$, but one surface has $\sigma = 1.0\lambda$ and the other has $\sigma = 0.8\lambda$. The surface with $\sigma = 1.0\lambda$ has, in certain areas, current intensity twice as high as those at $\sigma = 0.8\lambda$. I also found that different realizations of a surface with the same statistics may or may not have convergence difficulty. A possible explanation for this is that the topology of the surface is important. Again comparison of

the surface current on these surfaces may help identifying the important topological features. Since the surface is statistical in nature, many realizations must be examined to come to a definite conclusion in this regard.

The CPU time for calculating the scattering from a 64x64 and 128x128 point surface (8192 and 32768 unknowns) is 22 seconds and 5 minutes and 36 seconds per iteration, respectively, on one processor of a CRAY C90. The scaling is extemely close to N^2. Extrapolating this, it will take roughly 1.5 hours of CPU time per iteration for a 256x256 point surface. Further reduction of CPU time may be possible because the MOMI is a highly parallel algorithm.

[1] D. A. Kapp and G. S. Brown, "A New Numerical Method for Rough Surface Scattering Calculations", submitted to IEEE Trans. Antennas & Propagat.

Fast Simulation of Electromagnetic Scattering from Two-Dimensional Random Rough Surfaces †

W.C. Chew, R.L. Wagner, and J.M. Song

Center for Computational Electromagnetics
Department of Electrical and Computer Engineering
University of Illinois
Urbana, IL 61801-2991

1. Introduction

The problem of calculating the statistical properties of electromagnetic scattering from random rough surfaces has received considerable attention in recent years. As described by Ishimaru [1], one of the most interesting phenomena associated with rough-surface scattering is the occurrence of backscattering enhancement. Many authors have contributed to the development of approximate analytical theories for rough-surface scattering [2-8]. Significant experimental work has also been carried out on rough-surface scattering [9-11]. Because of the limited region of validity (in terms of surface-roughness parameters) of the approximate analytical approaches mentioned above, much work has been done using Monte Carlo simulation in conjunction with rigorous computational electromagnetic simulation techniques [12-19]. The three-dimensional vector wave scattering problem presents a great computational challenge. This paper describes our efforts to address this demanding problem for the rough-surface scattering example. This work can also be used to simulate the effect of rough surface on surface plasmon mode [20], or surface plasmon polariton related to Anderson localization [21,22].

2. An FMM-FFT Algorithm for Rough-Surface Scattering

This section presents a new algorithm developed for the efficient solution of the MOM matrix equation associated with the rough-surface scattering problem. The fast multipole method (FMM) [23-29] provides a very efficient and robust method for solving the MOM matrix equation. The FMM is a technique for fast computation of a matrix-vector multiply and is used in conjunction with an iterative matrix solver such as the conjugate-gradient (CG) method. Here we present a modification of the FMM designed to take advantage of the special geometry of the rough-surface scattering problem, in which the scatterer is nearly planar.

A detailed physical description of the FMM is given in the literature [23-27]. As noted in [23] and [26], the FMM may be expressed mathematically as a sparse decomposition of the MOM impedance matrix

$$\mathbf{Z} = \mathbf{Z}' + \mathbf{UTV}. \tag{21}$$

In the FMM, current elements on the scatterer are grouped together in groups of size M. In the above representation of $\mathbf{Z}$, $\mathbf{Z}'$ represents the interaction between groups that are near neighbors spatially. The matrix $\mathbf{V}$ computes the far-field radiation pattern of each group, tabulated at a discrete set of K

† This work was supported by the Office of Naval Research under grant N00014-95-1-0872, the National Science Foundation under grant NSF ECS 93-02145, and the Army Research Office under grant DAAH04-93-G-0430.

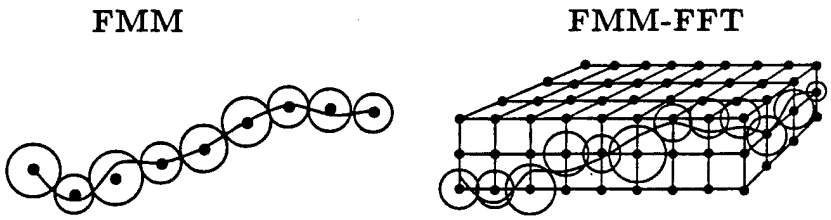

Figure 1. Illustration of the different grouping strategies employed by the FMM and FMM-FFT methods. In the FMM, the locations of the group centers are chosen to minimize the diameter of each group. In the FMM-FFT, the group centers are constrained to lie on a regular three-dimensional lattice.

directions around the unit sphere. The matrix $\mathbf{T}$ translates the K radiated field terms from each transmitting group to each receiving group elsewhere on the surface, which is the key to the efficiency of the FMM. Finally, the received radiation pattern at each group is transformed by the matrix $\mathbf{U}$ into the spatial domain fields on the surface of the scatterer.

Normally in the single-stage FMM, the group size M is chosen to be $M \sim \sqrt{N}$, where N is the total number of surface current unknowns. The resulting cost of a matrix-vector multiply is $O(N^{3/2})$ instead of the N^2 operations required for a dense matrix-vector multiply. Memory usage for this algorithm is also $O(N^{3/2})$ [27].

One possibility to further accelerate this algorithm is to implement a multi-level version of the FMM, in which the scatterer is subdivided recursively into smaller and smaller groups, and the FMM is applied in a nested manner. This method, called the multi-level fast multipole algorithm (MLFMA), has been implemented previously by several researchers [25,28,29]. This method reduces the cost of a matrix-vector multiply, and the associated memory usage, to $O(N \log N)$.

The new algorithm developed here is based on the FMM, and is designed to take advantage of the nearly planar geometry of the rough surface. The main idea is the following: choose the group size M to be a small constant, independent of the problem size (the number of groups is thus proportional to N), and place the FMM group centers on a regular three-dimensional lattice. Then the discretized translation operator $\mathbf{T}$ becomes convolutional and may be applied in $O(N \log N)$ operations using the FFT. The memory requirement of this solution strategy is of $O(N)$.

There is some inefficiency in the FMM-FFT algorithm due to the fact that the original problem, in which the unknowns are arranged on a two-dimensional surface, has now been embedded in a three-dimensional grid. This procedure has the effect of making N_{3D}, the number of grid points in the three-dimensional lattice, significantly larger than the number of FMM groups. This effect is clearly larger for surfaces with greater RMS surface height σ. However, the method is valid (i.e., will produce correct results) for *any* roughness parameters.

Furthermore, since the translation operation is a linear convolution, the grid data must be zero padded by a factor of two in each spatial dimension

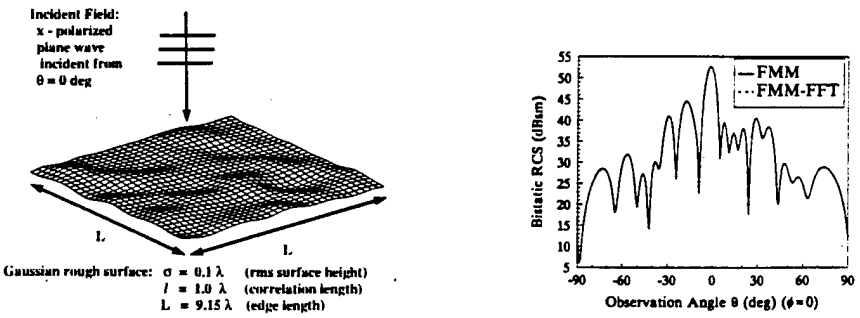

(a) (b)

Figure 2. A test case comparing the FMM and the FMM-FFT. The geometry is shown in (a), the results in (b). The results overlay one another.

to avoid unwanted edge effects due to the circular convolution computed via FFT. For a three-dimensional grid, this zero padding increases the effective FFT size by a factor of eight.

3. Numerical Results

As an initial test case, consider a Gaussian rough surface with edge length $L = 9.15\lambda$, RMS surface height $\sigma = 0.1\lambda$, and transverse correlation length $l = 1.0\lambda$. The incident field is a normally incident plane wave, polarized in the x direction. The problem was discretized with seven unknowns per wavelength in the x-y plane (i.e., $\triangle = \lambda/7$, where $\triangle$ is the discretization length in the x-y plane) for a total of $N = 8,064$ surface current unknowns. The conjugate-gradient solution was stopped at a relative residual error of 10^{-3}, requiring a total of 76 CG iterations. The geometry and scattered field are shown in Figure 2. As seen, the radar cross section (RCS) results obtained using the FMM and the FMM-FFT overlay one another exactly. The FMM code used to generate these results is the single-stage code described in detail in [27]. This code also served as the starting point for developing the FMM-FFT code used here.

The computational requirements are larger for rougher surfaces. To circumvent this difficulty, we have used the MLFMA for the case $\sigma = 0.7\lambda$, $l = 1.5\lambda$. All parameters, except the surface roughness, are the same as for the previous example. Most notably, the memory required for the MLFMA is only 30 MB, significantly less than any of the previous methods. Second, the matrix fill time for the MLFMA is 11 min, again much less than for the other methods. The time for a matrix-vector multiply for this problem using the MLFMA is 82 sec, which is less time than is required by the brute-force MOM approach. Thus, the MLFMA is the only one of the computer codes discussed here that is suitable for modeling large-scale rough surfaces in the backscattering enhancement regime, using a typical engineering workstation.

The total solution time using the MLFMA, however, is still fairly large due to the large number of CG iterations (146) needed to achieve a relative residual error of 10^{-3}. The CG iteration converges more slowly for rougher surfaces, which is consistent with the findings of other researchers [13,18].

The first Monte Carlo simulation was performed using rough-surface pa-

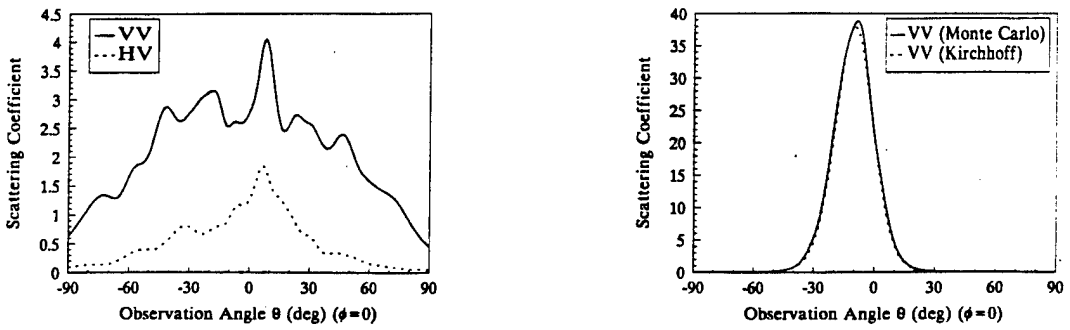

(a) (b)

Figure 3. (a) Monte Carlo simulation of the bistatic scattering coefficient γ for a rough surface with RMS height $\sigma = 0.7\lambda$ and transverse correlation length $l = 1.5\lambda$. The angle of incidence is $(\theta = 10°, \phi = 0°)$. (b) Same but with RMS height $\sigma = 0.07\lambda$. Also shown are the results of the Kirchhoff theory.

rameters $\sigma = 0.7\lambda$, $l = 1.5\lambda$, $L = 9.15\lambda$, $\triangle = \lambda/7$, and $N = 8,064$. The incident field is a vertically polarized Gaussian beam of half-width $W = 2.3\lambda$ incident from $(\theta = 10°, \phi = 0°)$. The MLFMA program was used to calculate the scattering from a total of 100 randomly generated rough surfaces. On the HP9000/715/50 workstation, the matrix fill time for each surface was 6 min, and the average solve time was 41 min; an average of 27 CG iterations were required to achieve a relative residual error of CGTOL $= 10^{-1}$. Thus, the total simulation time was 100×47 min $= 78$ hr of CPU time. The program used 30 MB of memory.

The results of the first Monte Carlo simulation are shown in Figure 3a. There is a pronounced peak of the scattering coefficient in the backscattering direction, $(\theta = 10°, \phi = 0°)$. This backscattering enhancement effect is quite strong in both the co-polarized scattering (VV) and the cross-polarized (HV) scattering. This result contrasts strongly with the second Monte Carlo simulation, discussed below.

The surface roughness parameters for the second simulation were $\sigma = 0.07\lambda$ and $l = 1.5\lambda$. The results of this simulation, along with the results of the approximate analytical Kirchhoff theory [2], are shown in Figure 3b. There is excellent agreement between the two solution methods.

4. Conclusions

In this paper, we have addressed the challenging goal of solving large-scale random rough-surface scattering problems using an MOM/Monte Carlo approach combined with efficient computational strategies.

A new FMM-FFT algorithm has been developed and investigated. This algorithm requires $O(N)$ memory and $O(N \log N)$ CPU time per matrix-vector multiply. The resulting computer code has been shown to be very efficient for surfaces with small RMS surface height, outperforming other fast algorithms such as the FMM and the MLFMA. While the FMM-FFT is most

efficient for small-scale roughness, the algorithm is also applicable to problems with large-scale roughness. An advantage of the FMM-FFT is the relatively simple structure of the algorithm. Since much of the computational burden is placed on the calculation of FFTs, machine-specific subroutine libraries can be used to implement the algorithm efficiently.

For problems with larger RMS surface heights, the MLFMA was found to provide superior performance. The main advantages of the MLFMA are its small memory usage and moderate matrix fill time. The algorithm requires $O(N \log N)$ memory and $O(N \log N)$ CPU time per matrix-vector multiply.

References

[1] A. Ishimaru, "Backscattering enhancement: from radar cross sections to electron and light localizations to rough-surface scattering," *IEEE Antennas Propagat. Mag.*, vol. 33, no. 5, pp. 7-11, October 1991.

[2] J. A. Kong, *Electromagnetic Wave Theory.* New York: Wiley, 1986.

[3] S. O. Rice, "Reflection of electromagnetic waves from slightly rough surfaces," *Commun. Pure Appl. Math.*, vol. 4, pp. 351-378, 1951.

[4] G. R. Valenzuela, "Depolarization of EM waves by slightly rounded surfaces," *IEEE Trans. Antennas Propagat.*, vol. 15, pp. 552-557, 1967.

[5] J. C. Leader, "Bidirectional scattering of electromagnetic waves from rough surfaces," *J. Appl. Phys.*, vol. 42, no. 12, pp. 4808-4816, November 1971.

[6] E. Bahar and B. S. Lee, "Full wave solutions for rough-surface bistatic radar cross sections: comparison with small perturbation, physical optics, numerical, and experimental results," *Radio Science*, vol. 29, no. 2, pp. 407-429, March-April 1994.

[7] R. E. Collin, "Scattering of an incident Gaussian beam by a perfectly conducting rough surface," *IEEE Trans. Antennas Propagat.*, vol. 42, no. 1, pp. 70-74, January 1994.

[8] A. A. Maradudin and E. R. Méndez, "Enhanced backscattering of light from weakly rough, random metal surfaces," *Appl. Opt.*, vol. 32, no. 19, pp. 3335-3343, July 1993.

[9] E. R. Méndez and K. A. O'Donnell, "Scattering experiments with smoothly varying random rough surfaces and their interpretation," in *Scattering in Volumes and Surfaces*, M. Nieto-Vesperinas and J. C. Dainty, Eds. Amsterdam: North-Holland, pp. 125-141, 1990.

[10] J. C. Dainty, M. -J. Kim, and A. J. Sant, "Measurements of angular scattering by randomly rough metal and dielectric surfaces," in *Scattering in Volumes and Surfaces*, M. Nieto-Vesperinas and J. C. Dainty, Eds. Amsterdam: North-Holland, pp. 143-155, 1990.

[11] Y. Kuga, J. S. Colburn, and P. Phu, "Millimeter-wave scattering from one-dimensional random rough surfaces of different surface correlation functions," *Waves in Random Media*, vol. 3, pp. 101-110, 1993.

[12] N. Garcia and E. Stoll, "Monte Carlo calculation for electromagnetic-wave scattering from random rough surfaces," *Phys. Rev. Lett.*, vol. 52, no. 20, pp. 1798-1801, May 1984.

[13] R. Devayya and D. J. Wingham, "The numerical calculation of rough-surface scattering by the conjugate gradient method," *IEEE Geosci. Remote Sensing*, vol. 30, no. 3, pp. 645-648, May 1992.

[14] L. Li, C. H. Chan, L. Tsang, K. Pak, and P. Phu, "Monte Carlo simulations and backscattering enhancement of random metallic rough surfaces at optical frequencies," *J. Electromagn. Waves and Appl.*, vol. 8, no. 3, pp. 277-293, 1994.

[15] L. Tsang, C. H. Chan, K. Pak, and H. Sangani, "Monte-Carlo simulations of large-scale problems of random rough-surface scattering and applications to grazing incidence with the BMIA/canonical grid method," *IEEE Trans. Antennas Propagat.*, vol. 43, no. 8, pp. 851-859, August 1995.

[16] P. Tran and A. A. Maradudin, "Scattering of a scalar beam from a two-dimensional randomly rough hard wall: Dirichlet and Neumann boundary conditions," *Appl. Opt.*, vol. 32, no. 15, pp. 2848-2851, May 1993.

[17] L. Tsang, C. H. Chan, and K. Pak, "Backscattering enhancement of a two-dimensional, random rough surface (three-dimensional scattering) based on Monte Carlo simulations," *J. Opt. Soc. Am. A*, vol. 11, no. 2, pp. 711-715, February 1994.

[18] P. Tran and A. A. Maradudin, "The scattering of electromagnetic waves from a randomly rough 2D metallic surface," *Opt. Commun.*, vol. 110, pp. 269-273, August 15, 1994.

[19] A. K. Fung, M. R. Shah, and S. Tjuatja, "Numerical simulation of scattering from three-dimensional randomly rough surfaces," *IEEE Geosci. Remote Sensing*, vol. 32, no. 5, pp. 986-994, September 1994.

[20] W. C. Chew, *Waves and Fields in Inhomogeneous Media.* New York: Van Nostrand Reinhold, 1990.

[21] E. Burstein, A. Hartstein, J. Schoenwald, A. A. Maradudin, D. L. Mills, and R. F. Wallis, "Surface polaritons - electromagnetic waves at interfaces," in *Polaritons*, E. Burstein and F. de Martini, Eds. London: Pergamon, pp. 89-108, 1974.

[22] D. Maystre and M. Saillard, "Localization of light by randomly rough surfaces: concept of localiton," *J. Opt. Soc. Am. A*, vol. 11, no. 2, pp. 680-690, February 1994.

[23] R. Coifman, V. Rokhlin, and S. Wandzura, "The fast multipole method for the wave equation: a pedestrian prescription," *IEEE Antennas Propagat. Mag.*, vol. 35, no. 3, pp. 7-12, June 1993.

[24] C. C. Lu and W. C. Chew, "Fast algorithm for solving hybrid integral equations," *IEE Proc.-H*, vol. 140, no. 6, pp. 455-460, December 1993.

[25] C. C. Lu and W. C. Chew, "A multilevel algorithm for solving boundary integral equations of wave scattering," *Microwave Opt. Technol. Lett.*, vol. 7, no. 10, pp. 466-470, July 1994.

[26] R. L. Wagner and W. C. Chew, "A ray-propagation fast multipole algorithm," *Microwave Opt. Technol. Lett.*, vol. 7, no. 10, pp. 435-438, July 1994.

[27] J. M. Song and W. C. Chew, "Fast multipole solution using parametric geometry," *Microwave Opt. Technol. Lett.*, vol. 7, no. 16, pp. 760-765, November 1994.

[28] J. M. Song and W. C. Chew, "Multilevel fast-multipole algorithm for solving combined field integral equations of electromagnetic scattering," *Microwave Opt. Technol. Lett.*, vol. 10, no. 1, pp. 14-19, September 1995.

[29] B. Dembart and E. Yip, "A 3D fast multipole method for electromagnetics with multiple levels," *11th Annual Review of Progress in Applied Computational Electromagnetics*, pp. 621-628, March 1995.

[30] R. J. Larsen and M. L. Marx, *An Introduction to Mathematical Statistics and its Applications*," 2nd ed. Englewood Cliffs, NJ: Prentice-Hall, 1986.

Observations of Scattering Effects due to Plasmon Polariton Excitation on Rough Metal Surfaces

K. A. O'Donnell, C. S. West, and M.E. Knotts, The School of Physics, Georgia Institute of Technology, Atlanta, Georgia 30332-0430, USA.

Over the years, many theoretical studies have considered the consequences of the excitation of surface plasmon polaritons on metal surfaces with random roughness [1-6]. Examples of effects predicted include backscattering enhancement [1,2], diffuse light bands [3], polarization effects with two-dimensional roughness [4], enhanced absorption [5], or more subtle effects arising from band gaps [6]. However, this work had generally not been adequately balanced by controlled experimental studies to the extent that a considerable number of the predicted effects had not even been observed. Why has this been the case? For experimentalists, it is not usually the scattering measurements themselves that are so difficult. Instead, many of the experimental possibilities have been severely limited simply because the fabrication of many types of surface roughness has been well beyond experimental capabilities. For one example, to this day no experiment has succeeded in observing polariton-related backscattering enhancement under the conditions it was first predicted to occur over ten years ago [1,2]. The surface parameters required were stated clearly and, from the lack of an experimental response, one can only conclude that it has not been possible to fabricate such a surface.

It is nonetheless possible to fabricate rough metal surfaces that, while not identical to those of theoretical studies above, are otherwise adequate to produce the desired effects. In particular, we employ optical methods to fabricate rough surfaces of known and controllable statistics in photoresist. In one of our techniques [7], a photoresist-coated glass plate is exposed to a large number N of sinusoidal fringe patterns of different periods and random relative phase; the individual exposures represent Fourier components that, for large N ($500 \leq N \leq 7500$ in practice), produce an effectively random roughness having Gaussian height statistics. This Fourier technique has been used to produce, for simplicity, a roughness power spectrum $S(k)$ that is of constant height between two limits, but nearly zero for all other wavenumbers k. A second technique we have developed [8] involves scanning a fine-scaled speckle pattern as the plate is exposed; this technique produces a

spectrum $S(k)$ that is of nearly Gaussian form centered on $k = 0$. Further, a photoresist plate can first be exposed to a strong sinusoidal fringe pattern, and then exposed to either of the two roughness-producing processes discussed above. In this case, the resulting surface is effectively a diffraction grating with an additional random roughness. After a photoresist plate has been exposed with the chosen technique, it is developed, coated with an optically thick layer (200 nm) of gold, is characterized with a stylus profilometer, and is finally ready for use in scattering studies.

We present scattering measurements in the case of a surface with a rectangular roughness spectrum, centered on nonzero wavenumber, with an rms roughness of 15 nm. Experiments are conducted at a variety of wavelengths from 543 to 674 nm, and it is shown that backscattering enhancement may be observed as long as the polariton wavenumber falls where $S(k)$ is nonzero. Further, if the polariton wavenumber is near one of the spectral limits, at various incidence angles one may observe either (a) no polariton-related scatter, (b) diffuse scatter due to the excitation of surface waves travelling in only one direction, or (c) scatter arising from counterpropagating plasmon polaritons. It is only for incidence angles satisfying the latter case that strong backscattering enhancement is observed.

In further experiments, it is possible to completely isolate the scattering processes that produce backscattering enhancement. In particular, it is shown that a surface having but two appropriate Fourier components allows the coherent interference responsible for backscattering enhancement to be observed directly. In particular, if one Fourier component launches a plasmon polariton, and the second component launches a counterpropagating plasmon polariton, a diffracted order that coincides with the backscattering direction is observed to sharply increase in power. By considering effects seen as the source wavelength is tuned through the critical wavelength that provides this simultaneous excitation, it is shown that the observations are consistent with the constructive interference of two isolated time-reversed paths.

The case of a sinusoidal grating with an additive roughness is also addressed experimentally. We observe distinct peaks at fixed scattering angle that are the diffuse light bands that had been noted in qualitative observations over twenty years ago [3]. It is discussed that these bands arise from plasmon polariton excitation produced by the random roughness; the excited polaritons are then outwardly coupled by the grating to create the

bands. It is demonstrated that the bands may take on various forms including a maximum, minimum, or an s-shaped curve. Further, the polarization-dependence of the diffuse bands is nontrivial and may be addressed through the Mueller matrix elements.

If the period of the roughened grating is appropriate to provide coupling of one surface wave to its counterpropagating counterpart, it is well-known that a gap appears in the polariton dispersion relation. It was discussed in numerical work by Michel [6] that, as the illumination is tuned through the frequency for which the gap appears, a single surface may produce three distinct effects. First, the diffuse light bands should be observed when the grating provides coupling to propagating waves, then suppression of polariton-related scatter should be seen within the band gap, and finally the appearance of backscattering enhancement should be observed. We provide direct experimental measurements of these three effects with a single well-characterized surface, and discuss other unusual behavior present in both the diffuse scatter and in the specular reflection.

References

1. A. R. McGurn, A. A. Maradudin, and V. Celli, *Phys. Rev. B* **31**, 4866-4871 (1985).

2. V. Celli, A. A. Maradudin, A. M. Marvin, and A. R. McGurn, *J. Opt. Soc. Am. A* **2**, 2225-2239 (1985).

3. V. L. Brudny and R. A. Depine, *J. Mod. Optics* **40**, 427-439 (1993) and references therein.

4. A. R. McGurn and A. A. Maradudin, *J. Opt. Soc. Am. B* **4**, 910 - 926 (1987).

5. J. A. Sanchez-Gil and M. Nieto-Vesperinas, *Phys. Rev. B* **45**, 8623-8633 (1992).

6. T. R. Michel, *J. Opt. Soc. Am. A* **11**, 1874-1885 (1994).

7. C. S. West and K. A. O'Donnell, *J. Opt. Soc. Am. A* **12**, 390-397 (1995).

8. T. R. Michel, M. E. Knotts and K. A. O'Donnell, *J. Opt. Soc. Am. A* **12**, 548-559 (1995).

A Canonical Scattering Problem

(Experimental data will be made available for all cases below; results show backscattering effects from surface plasmon polaritons)

A gold surface has surface statistics consistent with a Gaussian process and an rms roughness σ of 15.4 nm. The surface power spectrum $\Phi(k)$ has the unusual form shown: it exhibits a linear decay from a maximum at wavenumber $k = 0$ until it reaches zero at $k = 4.50 \times 10^{-3}$ nm^{-1}, $\Phi(k)$ then remains zero until it attains a constant value for k between 8.56×10^{-3} nm^{-1} and 13.3×10^{-3} nm^{-1}. The latter rectangular part contains 92% of the area of $\Phi(k)$, while the linear part near $k = 0$ contains 8% of the area.

The mean diffusely scattered intensities I_α are to be determined for any of three cases (with $\alpha = s$ or p, illumination wavelength λ, incidence angle θ_i, and scattering angle θ_s):

Case A: I_s and I_p, for $\lambda = 674$ nm, $\theta_i = 4°$, with θ_s on (-90°, 90°).
Case B: I_s and I_p, for $\lambda = 543$ nm, $\theta_i = 0°$, with θ_s on (-90°, 90°).
Case C: I_p for $\lambda = 674$ nm, $\theta_i = 6°$, 10°, 19°, and 24°, with θ_s on (-30°, 30°).

Normalization of I_α is the usual convention (unit area would imply perfect diffuse reflectance), and assume dielectric constants to be $\varepsilon = -13.3 + 1.03i$ ($\lambda = 674$ nm), or $\varepsilon = -5.00 + 2.13i$ ($\lambda = 543$ nm). Plots of I_α should be scaled such that 10° = 1.0 cm on the horizontal axis, and 0.10 dimensionless intensity units = 4.0 cm on the vertical axis for Cases A and B. Expand the horizontal axis to 10° = 3.0 cm for Case C.

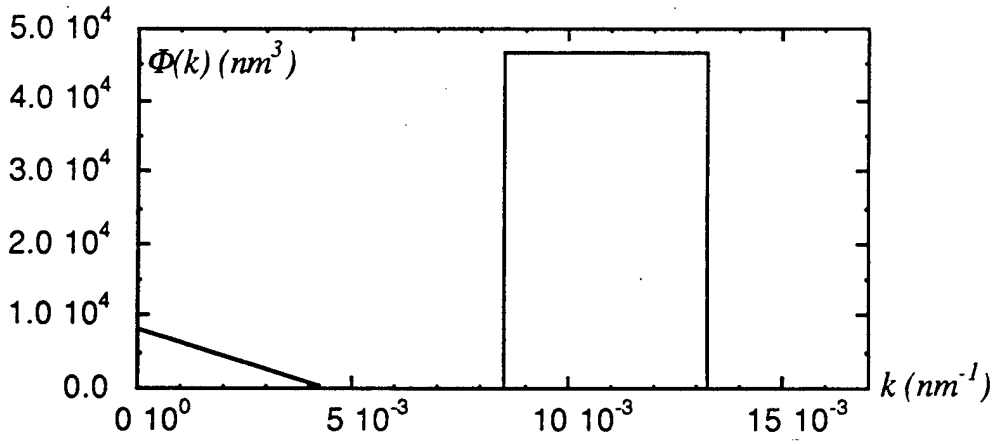

The roughness spectrum $\Phi(k)$; the vertical scale shown is such that $\sigma^2 = \int_0^\infty S(k)\,dk$.

ELECTROMAGNETIC INTEGRAL EQUATIONS FOR ROUGH SURFACE SCATTERING

John A. DeSanto
Department of Mathematical and Computer Sciences
Colorado School of Mines
Golden, CO 80401
Ph: (303) 273-3036
Fax: (303) 273-3875
E-mail: jdesanto@mines.edu

1. OUTLINE

The exact description of electromagnetic waves scattering from a rough surface separating two dielectrics is usually in terms of a boundary integral equation in coordinate space. Several versions of boundary integral equations are available. Starting with Green's theorem on say the electric field and the scalar free-space Green's function yields a Helmholtz integral representation for the electric field using boundary unknowns of the electric field and its normal derivative. This is a transitional stage in derivations since the boundary conditions are in terms of currents. The unknowns are replaced using identities relating them to the currents and charge densities and the resulting representation is that due to Stratton and Chu. Further, taking the curl of the Stratton-Chu equations yields the Franz equations which are representations solely in terms of tangential boundary currents. Integral equations result in the limit as the exterior coordinate variable approaches the surface. Depending on the formulation, finite part integrals may result, and computational techniques have been developed to treat these cases. Common examples resulting from this are the Electric Field Integral Equations (EFIE) and the Magnetic Field Integral Equation (MFIE).

In this discussion we return to the original formulation in terms of the electric field and its normal derivative on the boundary. We develop continuity conditions for the normal derivative of the electric field using the continuity conditions for the current. An additional term results which can be integrated by parts and folded into the term multiplying the electric field on the boundary. The result is a 6 x 6 system of equations for the six boundary unknowns (electric field vector and its normal derivative). Broken up into four 3 x 3 block matrices, the advantage of the system is that three of the blocks are diagonal. The entire coupling resides in one 3 x 3 block.

2. SCALAR CASE

Consider a rough interface $z = h(x_t)$ (where $x_t = (x, y)$) separating media of different densities ρ_j (ratio $\rho = \rho_2/\rho_1$) existing in regions V_j ($j = 1$ is $z>h$ and $j = 2$ is $z<h$). The scalar fields in each region satisfy Helmholtz equations with different wave numbers k_j. The formalism uses Green's theorem in each region with free-space Green's functions G_j corresponding to each half-space, continuity of the fields (ψ) and their normal derivatives (N) at the interface, and the limits of the field representations as the field point approaches the surface h. The equations are

$$\frac{1}{2}\psi(\vec{x}_h') = \psi^{(0)}(\vec{x}_h') + \int\int n_j \partial_j G_1(\vec{x}_h', \vec{x}_h)\psi(\vec{x}_h)dx_t, - \int\int G_1(\vec{x}_h', \vec{x}_h)N(\vec{x}_h)dx_t \quad (1)$$

and

$$\frac{1}{2}\psi(\vec{x}_h') = \rho\int\int G_2(\vec{x}_h', \vec{x}_h)N(\vec{x}_h)dx_t - \int\int n_j \partial_j G_2(\vec{x}_h', \vec{x}_h)\psi(\vec{x}_h)dx_t, \quad (2)$$

(the integrals involving the normal derivatives of G_1 and G_2 use the direct values of these functions). The result is two coupled integral equations for the two boundary unknowns ψ and N. They can be thought of as second-kind equations for ψ and first-kind on N [1, 2]. Other equations can be generated by taking the normal derivative of the field representations and then passing to the surface limit. These yield hypersingular equations on N and first kind on ψ [3]. Alternative versions of the latter equations are available due to Maue [4] and Mitzner [5]. For scattering from bounded bodies, linear combinations of these equations yield equations unique at all frequencies [6, 7]. For our case this is not necessary since the surface is assumed to be of infinite extent. The result is two coupled equations on the boundary unknowns.

3. CANONICAL ELECTROMAGNETIC CASE

Equations analogous to those for the scalar case can be derived for each component of the electric and magnetic fields. To continue the development requires continuity conditions on, say, the electrical field (which are known via the displacement continuity results) and continuity conditions on the normal derivative of the electric field (which are not standard boundary unknowns).

The development of the canonical formalism due to Stratton and Chu [8, 9] rewrites the above boundary unknowns in terms of the normal components of the electric and magnetic fields (2 terms) and the tangential boundary currents (4 terms). The continuity of the four currents implies the continuity of the normal components. The result is four coupled integral equations on the currents. The equations resulting from the electric and magnetic field representations are referred to as the electric field integral equation (EFIE), a first kind equation, and the magnetic field integral equation (MFIE) which is second kind [10, 11]. Each contains two boundary unknowns.

An alternative to the Stratton-Chu formalism is to take the curl of the Stratton-Chu field equations and then take the surface limit. The gradient terms in the equations vanish (they contain the normal components of the fields). The resulting equations are alternative versions of the EFIE and MFIE but the kernels have higher order singularities. These were published by Franz [12] and the derivation from Stratton-Chu was given by Hönl et al [13]. They were previously used by us in the rough surface scattering problem in conjunction with diagram techniques [14].

4. ALTERNATIVE EQUATIONS

We return to the original Green's theorem results analogous to the scalar case. The problem with the equations was the lack of a continuity condition on the normal derivative of the electric field. Using the continuity of the currents a quasi-continuity condition on the normal derivatives can be derived. It contains a remainder term consisting of tangential surface derivatives which can be integrated by parts and the result combined with the electric field unknown under the integral. For the electric fields the displacement and current continuity conditions can be written in the form (summation convention, ε is the ratio of dielectric constants)

$$E_i^{(2)}(\vec{x}_h) = A_{ij}(\vec{x}_t)E_j^{(1)}(\vec{x}_h), \tag{3}$$

where

$$A_{ij}(\vec{x}_t) = \delta_{ij} + (\varepsilon^{-1} - 1)\hat{n}_i\hat{n}_j, \tag{4}$$

The resulting equations are analogous to the scalar equations. They are

$$\begin{aligned} \frac{1}{2}E_i(\vec{x}_h') &= E_i^{(0)}(\vec{x}_h') + \int\int n_j\partial_j G_1(\vec{x}_h', \vec{x}_h)E_i(\vec{x}_h)dx_t \\ &\quad - \int\int G_1(\vec{x}_h', \vec{x}_h)N_i(\vec{x}_h)dx_t, \end{aligned} \tag{5}$$

and

$$\begin{aligned} \frac{1}{2}A_{ij}(\vec{x}_t')E_j(\vec{x}_h') &= \mu\int\int G_2(\vec{x}_h', \vec{x}_h)N_i(\vec{x}_h)dx_t \\ &\quad + \int\int K_{ij}(\vec{x}_h', \vec{x}_h)E_j(\vec{x}_h)dx_t. \end{aligned} \tag{6}$$

The equations are in terms of the boundary electric field (E_i) and its normal derivative (N_i). The kernel K_{ij} in Eq. (6) contains normal and tangential derivatives of the Green's functions and μ is the ratio of magnetic permeabilities.

The key result of these equations is that only three of the six equations are coupled. This is a reduction from the four coupled Stratton-Chu and Franz equations. This result is also evident in a spectral coordinate version of the above [15]. Some of these results will appear shortly [16].

REFERENCES

[1] Nieto-Vesperinas, M., *Scattering and Diffraction in Physical Optics*, Wiley-Interscience, New York, 1991.

[2] Colton, D. and Kress, R., *Integral Equation Methods in Scattering Theory*, Wiley-Interscience, New York, 1983.

[3] Martin, P.A., and P. Ola, *Proc. Roy. Soc. Edinburgh* **123A**, 185-208, 1993.

[4] Maue, A.W., *Zeit. für Physik* **126**, 601-618, 1949.

[5] Mitzner, K.M., *J. Math. Phys.* **5**, 1776-1786, 1964.

[6] Cho, S.K., *Electromagnetic Scattering*, Springer, New York, 1990.

[7] Morita, N., N. Kumagai and J.R. Mautz, *Integral Equation Methods for Electromagnetics*, Artech House, Norwood, MA, 1987.

[8] Stratton, J.A. and L.J. Chu, *Phys. Rev.* **56**, 99-107, 1939.

[9] Stratton, J.A., *Electromagnetic Theory*, McGraw-Hill, New York, 1941.

[10] Jones, D.S., *Methods in Electromagnetic Wave Propagation*, Clarendon Press, Oxford, 1994.

[11] DeSanto, J.A. and G.S. Brown, in *Progress in Optics* **XXIII**, ed. E. Wolf, North-Holland, pp. 1-62, 1986.

[12] Franz, W., *Zeit. für Naturforschung* **3a**, 500-506, 1948.

[13] Hönl, H., A.W. Maue, and K. Westpfahl, *Handbuch der Physik*, ed. S. Flügge, **25/1** Kristeloptik, pp. 218-573, Springer, 1961.

[14] DeSanto, J.A., *J. Math. Phys.* **15**, 283-288, 1974.

[15] DeSanto, J.A., *J. Elect. Waves and Applications* 7, 1293-1306, 1993.

[16] DeSanto, J.A., in *New Perspectives on Problems in Classical and Quantum Physics*, eds. P.P. Delsanto and A.W. Saenz, Gordon and Breach, 1996.

Backscattering Enhancement and Localization Effect in the Scattering from a Random Rough Metal Surface - Stochastic Functional Approach -

H. Ogura

Dept. of Electronics, Kyoto University, Yoshida, Kyoto 606, Japan
Fax +81-75-753-5919, e-mail ogura@kuee.kyoto-u.ac.jp

The scattering of light by a silver film with a random rough surface and the excitation of surface plasmon modes on the metal surface are studied by means of the stochastic functional approach assuming that the random surface is a homogeneous Gaussian random field. The stochastic wave field, given in the stochastic Floquet form due to the homogeneity of random surface, is represented as a Wiener-Itô expansion in terms of Wiener-Hermite orthogonal functionals, and approximate solutions are obtained for the Wiener kernel functions.

We deal with the attenuated total reflection (ATR) configuration which consists of a silver film sandwiched between air and a crystal prism through which the surface plasmon on the silver-crystal interface is excited. Free plasmon mode is given by a pole of the free plasmon propagator in the absence of the surface roughness, while the "dressed" or perturbed plasmon is defined by a complex pole of the perturbed plasmon propagator which involves the mass operator [1]. The mass operator, or the self-interacting operator which appears in the perturbed plasmon propagator, describes the "dressed" plasmon mode involving the multiple scattering effect due to the surface roughness. The mass operator is shown to satisfy the nonlinear integral equation, which corresponds to the Dyson equation in the multiple scattering theory.

The first Wiener kernel, expressed by the perturbed plasmon propagator, can be interpreted as describing a "single" scattering process of "dressed" plasmon, while the second Wiener kenrnel describes a pair of reciprocal, symmetric "double" scattering processes of "dressed" plasmons.

The random surface is assumed to be a random grating such that the power spectrum possesses a pair of sharp peaks at the Bragg spatial frequency for the plasmon mode, so that the random surface looks like a periodic grating with spatial fluctuations. With the ATR geometry, using silver's dielectric constant at He-Ne laser frequency, the angular distributions of incoherent scattering into both air and crystal sides are numerically calculated by using the first- and second Wiener kernels for various combination of parameters.

In the angular distribution of incoherent scattering into crystal, strong peaks appear corresponding to the excited forward- and backward-travelling plasmon modes, which are mainly described by the first Wiener kernel containing the "dressed" plasmon propagator, and an enhanced scattering peak appears in the backward direction. These resonance peaks, visible in the crystal side, are invisible in the air side because of the plasmons being evanescent. In the incoherent scattering distribution in the air side, an enhanced scattering peak also appears in a certain direction related to the incident angle in the crystal side.

The enhanced scattering observed on both sides comes from the second Wiener kernel that describes the "double scattering" processes occurring in the reciprocal directions, where the strongly excited plasmon modes take part in the intermediate processes of the "double " scattering, and the pair of "double" scattering process interfere each other to create the enhancement in the scattering amplitude. The imaginary part of the "dressed" plasmon pole is closely connected with the peak width of the enhanced backscattering.

The mechanism of the backscattering enhancement so expained is quite similar to the scalar wave scattering from a Neumann random surface [2], electromagnetic scattering from a perfectly conducting random surface [3] and the scattering from a waveguide structure with random boundary [4].

At the resonant incidence where the incident angle satisfies the Bragg condition associated with the Bragg spatial frequency of the random grating, the surface plasmon mode is strongly excited on the random grating, and would propagate in the "random medium" along the surface, and the interaction of such propagating modes with the rough surface would be much stronger than in the "double" scattering processes which create the enhanced backscattering. Consequently, it is expected that the localization of plasmon waves may take place on the rough surface as a result of such "multiple" scattering of "dressed" plasmon modes that is strongly excited by the resonant incidence.

Although the multiple Wiener integral in terms of Gaussian random measures describing the random surface is introduced as a mathematical tool to express the stochastic wave field, it is possible to obtain a realization of the stochastic wave field by numerically calculating the multiple Wiener integrals using the Gaussian random measure approximated by a set of Gaussian random numbers. For a random grating with a pair of sharp spectral peaks, the stochastic wave field in terms of Wiener-Itô expansion can be greatly simplified, and the stochastic coefficients of the forward- and backward travelling "dressed" plasmon waves can be given by the sum of even-order and odd-order multiple Wiener integrals, respectively, and they can be numerically calculated by an iterative procedure. In this way we can evaluate the random wave field as a result of "multiple" scattering process, and we get the localized plasmon waves by the computation up to several order of multiple integral corresponding to the order of "multiple" scattering. Several localized plasmon waves on a certain interval are actually obtained by such numerical calculation of stochastic wave field [1]. At resonant excitation this approximate formalism for "multiple" scattering gives a divergent results as the order is increased, yet the localized wave form being almost unchanged. To avoid the divergence in the resonant excitation we can employ the other formulation of the stochastic functional approach in such a way that we can formulate from the begining the interactions between randomly modulated plasmon harmonics, where we have recourse to the other method of solution than the Wiener-Itô expansion.

[1] H.Ogura and Z.L.Wang: "Surface-plasmon mode on a random rough metal surface - Enhanced backscattering and localization" -, *Phys. Rev. B*, **53**, No.15, April (1996).

[2] H.Ogura and N.Takahashi: "Wave scattering from a random rough surface: reciprocal theorem and backscattering enhancement", *Waves in Random Media* **5**, 223-242 (1995).

[3] H.Ogura, T.Kawanishi, N.Takahashi and Z.L.Wang: "Scattering of electromagnetic waves from a slightly random surface — reciprocal theorem, cross-polarization and backscattering enhancement", *Waves in Random Media* **5**, 461-495 (1995).

[4] Z.L. Wang, H.Ogura and N.Takahashi: "Enhanced scattering from a planar waveguide structure with a slightly rough boundary", *Phys. Rev. B*,**52**, No.8, pp.6027-6041, (1995).

X-Ray Scattering From a Randomly Rough Surface

T. A. Leskova

Institute of Spectroscopy

Russian Academy of Sciences

Troitsk, Moscow Region 142092 RUSSIA

A. A. Maradudin

Department of Physics and Astronomy

and Institute for Surface and Interface Science

University of California

Irvine, CA 92717, U.S.A.

1. Introduction

The scattering of x-rays from rough surfaces and interfaces has been used extensively as a powerful experimental tool for investigating surface and interface properties (see, e.g., the recent reviews [1,2] and references therein). Since the dielectric function of the scattering medium $\epsilon(\omega)$ in the x-ray frequency region is close to, and a little smaller than, unity, $\epsilon(\omega) = 1 - \eta(\omega)$, where $\eta(\omega)$ is real and lies in the range $10^{-6} - 10^{-3}$ depending on the wavelength of the x-rays, the phenomenon of total internal reflection of x-rays occurs when the angle of incidence θ_0 equals the critical angle $\theta_c = \cos^{-1}\sqrt{\eta(\omega)}$. As a result, the reflectivity for grazing angles of incidence tends to unity, and the intensity of the incoherent component of the scattered x-rays tends to zero. For angles of incidence smaller than θ_c, however, the reflectivity rapidly tends to zero, while the intensity of the incoherent component of the scattered x-rays increases. In addition, the latter intensity displays a sharp asymmetric peak, called the Yoneda peak [3], at a scattering angle θ_s equal to θ_c, which has been observed in x-ray scattering from rough solid and liquid surfaces, and from the interfaces in multilayer structures [4-9] (see Fig. 1).

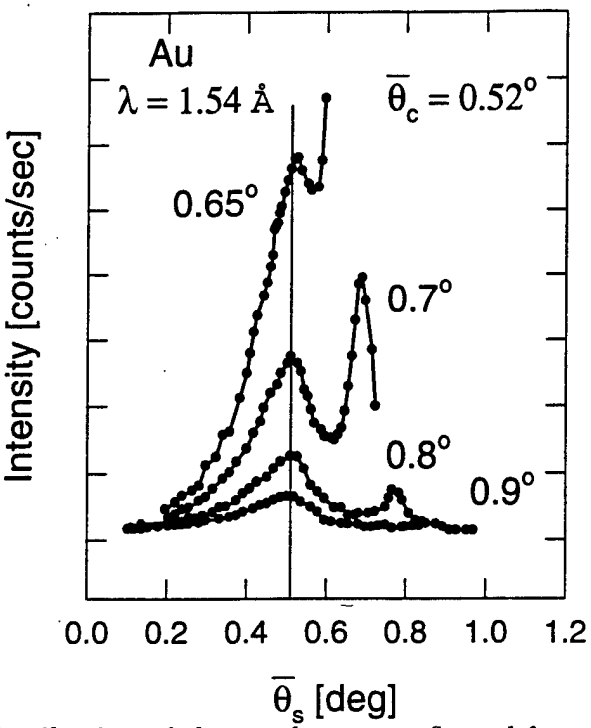

Fig.1 The angular distribution of the total power reflected from a gold surface as a function of the grazing scattering angle $\bar{\theta}_s = \pi/2 - \theta_s$ for several values of the grazing angle of incidence $\bar{\theta}_0 = \pi/2 - \theta_0$ greater than $\bar{\theta}_c = \pi/2 - \theta_c$. The wavelength of the incident x-rays is $\lambda = 1.54\mathring{A}$. $\bar{\theta}_c = 0.52°$. The Yoneda peak at $\bar{\theta}_s = \bar{\theta}_c$ is clearly seen, as is the specular peak at $\bar{\theta}_s = \bar{\theta}_0$. [After Ref. [4]].

Theories of x-ray scattering from rough surfaces and interfaces in multilayered structures have been constructed on the basis of the Born [6] and distorted-wave Born approximations [6], which exploit the weak interaction of x-rays and the scattering medium. The Born approximation is valid for small angles of incidence and scattering, but breaks down in the vicinity of θ_c [2,6]. The distorted-wave Born approximation describes well the scattering of x-rays for angles of incidence in the vicinity of θ_c, e.g. the angular dependence of the intensity of the incoherent component of the scattered x-rays obtained in this approximation displays the Yoneda peak. However, the distorted-wave Born approximation fails at smaller angles of incidence [2,6].

For grazing angles of incidence smaller than $\bar{\theta}_c = \pi/2 - \theta_c$ both the Born and distorted-wave Born approximations break down: the reflectivity obtained in the Born approximation diverges instead of saturating at $\bar{\theta}_c$, while the reflectivity obtained in the distorted-wave Born approximation is greater than unity or, for a weakly rough surface, is exactly equal to unity [6].

In this paper we present a theory of x-ray scattering from randomly rough surfaces based on the method of reduced Rayleigh equations [10], that possesses the advantages of the Born and distorted-wave Born approximations, and lacks their disadvantages. In our approach the integral equation for the scattering amplitude is calculated perturbatively as an expansion in powers of the dielectric contrast $\eta(\omega)$, the small parameter of our problem. The validity of the resulting solution is limited only by the condition for the validity of the Rayleigh hypothesis [11,12], on which the method of reduced Rayleigh equations is based, viz. $|d\zeta(x_1)/dx_1| \ll 1$ in the case of a one-dimensional random surface, and $|\nabla\zeta(x_1, x_2)| \ll 1$ in the case of a two-dimensional random surface, where $\zeta(x_1)$ ($\zeta(x_1, x_2)$) is the surface profile function which defines the position of the surface through the equation $x_3 = \zeta(x_1)(x_3 = \zeta(x_1, x_2))$ [13-15].

We also assume that the scattering medium is homogeneous on the length scale being probed, i.e. the atomic structure of the scattering medium is ignored. This assumption is valid as long as we deal with small angle scattering, where the condition $4\pi(a/\lambda)\sin\theta \ll 1$ is satisfied, where 2θ is the scattering angle, i.e. $2\theta = \pi - \theta_0 - \theta_s$, λ is the wavelength of the x-rays, and a is a typical length scale for any inhomogeneity within the scattering medium [6].

2. Scattering Theory

Due to space limitations we will outline here only the derivation of the results for scattering from one-dimensional surfaces. The derivation of the corresponding results for the scattering of x-rays from two-dimensional random surfaces, while algebraically more complicated, follows closely that for one-dimensional surfaces, and will be presented elsewhere.

The system we consider consists of vacuum in the region $x_3 > \zeta(x_1)$, and a metal charac-

terized by an isotropic, frequency-dependent dielectric function $\epsilon(\omega)$ in the region $x_3 < \zeta(x_1)$. The surface profile function $\zeta(x_1)$ is assumed to be a single-valued function of x_1 that is differentiable as many times as is necessary, and constitutes a zero-mean, stationary, Gaussian random process, defined by $\langle \zeta(x_1)\zeta(x_1')\rangle = \delta^2 W(|x_1 - x_1'|)$. The angle brackets here denote an average over the ensemble of realizations of $\zeta(x_1)$, and $\delta = \langle \zeta^2(x_1)\rangle^{\frac{1}{2}}$ is the rms height of the surface. For the surface height autocorrelation function we will assume the Gaussian form $W(|x_1|) = \exp(-x_1^2/a^2)$. The characteristic length a appearing in the expression is the transverse correlation length of the surface roughness.

The surface is illuminated from the vacuum side by a p-polarized electromagnetic wave of frequency ω, whose plane of incidence is the x_1x_3-plane. The single non-zero component of the magnetic vector in the region $x_3 > \zeta(x_1)_{max}$ is given by

$$H_2^{>}(x_1, x_3|\omega) = e^{ikx_1 - i\alpha_0(k)x_3} + \int_{-\infty}^{\infty} \frac{dq}{2\pi} R(q|k) e^{iqx_1 + \alpha_0(k)x_3}, \tag{2.1}$$

where $\alpha_0(q) = ((\omega^2/c^2) - q^2)^{\frac{1}{2}}$, with $Re\alpha_0(q) > 0$, $Im\alpha_0(q) > 0$.

The differential reflection coefficient (drc) $\partial R/\partial\theta_s$ is the fraction of the power in the incident wave that is scattered into an angular interval of width $d\theta_s$ about the scattering angle θ_s. Since the scattering surface is random, we are interested not in the differential reflection coefficient itself, but in its average over the ensemble of realizations of the surface profile function, $\langle \partial R/\partial\theta_s\rangle$. The contribution to the mean differential reflection coefficient from the coherent and incoherent components of the scattered electromagnetic field are given by

$$\left\langle \frac{\partial R}{\partial \theta_s} \right\rangle_{coh} = \frac{1}{L_1} \frac{\omega}{2\pi c} \frac{\cos^2\theta_s}{\cos\theta_0} |\langle R(q|k)\rangle|^2 \tag{2.2a}$$

$$\left\langle \frac{\partial R}{\partial \theta_s} \right\rangle_{incoh} = \frac{1}{L_1} \frac{\omega}{2\pi c} \frac{\cos^2\theta_s}{\cos\theta_0} [\langle |R(q|k)|^2\rangle - |\langle R(q|k)\rangle|^2], \tag{2.2b}$$

respectively, where L_1 is the length of the x_1-axis covered by the random surface, while the angles of incidence and scattering are related to the wave numbers k and q by $k = (\omega/c)\sin\theta_0$ and $q = (\omega/c)\sin\theta_s$, respectively. The angle of incidence θ_0 is measured counterclockwise from the x_3-axis, while the scattering angle θ_s is measured clockwise from this axis.

The reduced Rayleigh equation [10] satisfied by the scattering amplitude $R(q|k)$ can be written in the form

$$R(q|k) = 2\pi\delta(q-k)R_0(k) + \frac{\eta}{d(q)}N(q|k) + \frac{\eta}{d(q)}\int_{-\infty}^{\infty}\frac{dp}{2\pi}M(q|p)R(p|k), \tag{2.3}$$

where

$$R_0(k) = \frac{\epsilon\alpha_0(k)-\alpha(k)}{\epsilon\alpha_0(k)+\alpha(k)} \tag{2.4a}$$

$$N(q|k) = \frac{qk-\alpha(q)\alpha_0(k)}{\alpha(q)+\alpha_0(k)}J(\alpha(q)+\alpha_0(k)|q-k) \tag{2.4b}$$

$$M(q|p) = \frac{qp+\alpha(q)\alpha_0(p)}{\alpha(q)-\alpha_0(k)}J(\alpha(q)-\alpha_0(p)|q-p) \tag{2.4c}$$

$$d(q) = \epsilon\alpha_0(q)+\alpha(q), \tag{2.4d}$$

$\alpha(q) = (\epsilon(\omega^2/c^2)-q^2)^{\frac{1}{2}}$, with $Re\alpha(q) > 0$, $Im\alpha(q) > 0$, and

$$J(\gamma|Q) = \int_{-\infty}^{\infty}dx_1 e^{-iQx_1}(e^{-i\gamma\zeta(x_1)}-1). \tag{2.5}$$

We will seek the solution of Eq. (2.3) in the form

$$R(q|k) = 2\pi\delta(q-k)R_0(k) + B(q|k), \tag{2.6}$$

where the function $B(q|k)$ satisfies the equation

$$B(q|k) = \eta A(q|k) + \eta\int_{-\infty}^{\infty}\frac{dp}{2\pi}m(q|p)B(p|k), \tag{2.7}$$

with

$$A(q|k) = n(q|k) + m(q|k)R_0(k) \tag{2.8a}$$

$$m(q|k) = \hat{m}(q|k)J(\alpha(q)-\alpha_0(k)|q-k) \tag{2.8b}$$

$$n(q|k) = \hat{n}(q|k)J(\alpha(q)+\alpha_0(k)|q-k) \tag{2.8c}$$

$$\hat{m}(q|k) = \frac{qk+\alpha(q)\alpha_0(k)}{d(q)[\alpha(q)-\alpha_0(k)]} \tag{2.8d}$$

$$\hat{n}(q|k) = \frac{qk-\alpha(q)\alpha_0(k)}{d(q)[\alpha(q)+\alpha_0(k)]}. \tag{2.8e}$$

The iterative solution of Eq. (2.7) is formally an expansion of $B(q|k)$ in powers of η:

$$B(q|k) = \eta A(q|k) + \eta^2 \int_{-\infty}^{\infty} \frac{dp_1}{2\pi} m(q|p_1) A(p_1|k) + \\ + \eta^3 \int_{-\infty}^{\infty} \frac{dp_1}{2\pi} \int_{-\infty}^{\infty} \frac{dp_2}{2\pi} m(q|p_1) m(p_1|p_2) A(p_2|k) + \cdots \tag{2.9}$$

3. Coherent Scattering

From Eq. (2.2a) we see that the contribution to the mean drc from the coherent component of the scattered x-rays is expressed in terms of $\langle R(q|k)\rangle$, where

$$\langle R(q|k)\rangle = 2\pi\delta(q-k)R_0(k) + \langle B(q|k)\rangle. \tag{3.1}$$

To obtain $\langle B(q|k)\rangle$ we average Eq. (2.9) term-by-term:

$$\langle B(q|k)\rangle = \eta\langle A(q|k)\rangle + \eta^2 \int_{-\infty}^{\infty} \frac{dp_1}{2\pi} \langle m(q|p_1) A(p_1|k)\rangle + \\ + \eta^3 \int_{-\infty}^{\infty} \frac{dp_1}{2\pi} \int_{-\infty}^{\infty} \frac{dp_2}{2\pi} \langle m(q|p_1) m(p_1|p_2) A(p_2|k)\rangle + \cdots \tag{3.2}$$

In view of Eqs. (2.8a)-(2.8c) we see that the nth order term in this expansion contains the average of the product of n $J(\gamma|Q)$ functions. This average is given by

$$\langle J(\gamma_1|Q) J(\gamma_2|Q) \cdots J(\gamma_n|Q_n)\rangle = \prod_{j=1}^{n} 2\pi\delta(Q_j)(e^{-\frac{1}{2}\gamma_j^2\delta^2} - 1) + \\ + \theta(n-2) \sum_{\substack{i,j=1 \\ (i>j)}}^{n} 2\pi\delta(Q_i+Q_j) e^{-\frac{1}{2}(\gamma_i^2+\gamma_j^2)\delta^2} \int_{-\infty}^{\infty} du e^{-iQ_i u} (e^{-\gamma_i\gamma_j\delta^2 W(|u|)} - 1) \times \\ \times \prod_{\substack{k=1 \\ (k\neq i,j)}}^{n} 2\pi\delta(Q_k)(e^{-\frac{1}{2}\gamma_k^2\delta^2} - 1) + \\ + \text{terms that contain the product of } n-2 \text{ or fewer delta functions} \tag{3.3a}$$

$$= \prod_{j=1}^{n} \langle J(\gamma_j|Q_j)\rangle + \theta(n-2) \sum_{\substack{i,j=1 \\ (i>j)}}^{n} \{J(\gamma_i|Q_i)J(\gamma_j|Q_j)\} \prod_{\substack{k=1 \\ (k\neq i,j)}}^{n} \langle J(\gamma_k|Q_k)\rangle +$$

+terms that contain the product of $n-2$ or fewer delta functions, (3.3b)

where $\theta(n) = 1$ for $n \geq 1$ and $\theta(n) = 0$ for $n < 0$, and we have introduced the notation that for any two functions A and B

$$\{AB\} = \langle AB\rangle - \langle A\rangle\langle B\rangle \tag{3.4}$$

is the correlated part of the average of their product.

The significance of grouping terms in the average $\langle J(\gamma_1|Q_1)\cdots J(\gamma_n|Q_n)\rangle$ according to the number of delta functions they contain stems from the fact that the diagonal elements of the functions $\hat{m}(q|k)$ and $\hat{n}(q|k)$ defined by Eqs. (2.8d) and (2.8e) are proportional to η^{-1}:

$$\hat{m}(q|q) = -\frac{1}{\eta}, \quad \hat{n}(q|q) = \frac{R_0(q)}{\eta}. \tag{3.5}$$

This result together with the result given by the first term on the right hand side of Eq. (3.3) means that *each* term on the right hand side of Eq. (3.2) has a contribution that is of $O(\eta^0)$. Thus, in order to obtain the contribution to $\langle B(q|k)\rangle$ that is of zero order in η we have to sum the contribution of this order in each of the terms on the right hand side of Eq. (3.2). To obtain this contribution it suffices to replace the average in each term on the right hand side of Eq. (3.2) by the product of the averages of the individual factors, according to Eq. (3.3b). In this way we obtain

$$\langle B(q|k)\rangle_{(0)} = 2\pi\delta(q-k)[1 - X(k) + X(k)^2 - \cdots]a(k), \tag{3.6}$$

where we have used the results that

$$\langle m(q|k)\rangle = 2\pi\delta(q-k)[-\frac{X(k)}{\eta}] \tag{3.7a}$$

with

$$X(k) = e^{-\frac{1}{2}(\alpha(k)-\alpha_0(k))^2\delta^2} - 1, \tag{3.7b}$$

and

$$\langle A(q|k)\rangle = 2\pi\delta(q-k)[\frac{a(k)}{\eta}], \tag{3.8a}$$

with

$$a(k) = R_0(k)[e^{-\frac{1}{2}(\alpha(k)+\alpha_0(k))^2\delta^2} - e^{-\frac{1}{2}(\alpha(k)-\alpha_0(k))^2\delta^2}]. \tag{3.8b}$$

It follows that

$$\langle B(q|k)\rangle_{(0)} = 2\pi\delta(q-k)R_0(k)[e^{-2\alpha_0(k)\alpha(k)\delta^2} - 1]. \tag{3.9}$$

To obtain the leading contribution to $\langle B(q|k)\rangle$ that is of nonzero order in η we have to take into account the contribution to the average in each term on the right hand side of Eq. (3.2) from the second term on the right hand side of Eq. (3.3). Operationally, the latter tells us that in each term (starting with the second) we have to pair two factors and evaluate the correlated part of the average of their product, and then multiply the result by the product of the average of each of the remaining factors. Two sequences of terms arise, depending on whether the final factor $A(p_{n-1}|k)$ is one of the factors in the pair whose product is averaged, or whether it is one of the factors that is averaged separately. The contributions to $\langle B(q|k)\rangle$ from these two sequences are both of $O(\eta^2)$, and are given by

$$\begin{aligned}\langle B(q|k)\rangle_{(21)} &= \eta^2[1 - X(q) + X(q)^2 - \cdots]\int_{-\infty}^{\infty}\frac{dp}{2\pi}\{m(q|p)\times \\ &\quad \times[1 - X(p) + X(p)^2 - \cdots]A(p|k)\}\end{aligned} \tag{3.10a}$$

and

$$\begin{aligned}\langle B(q|k)\rangle_{(22)} &= \eta^2[1 - X(q) + X(q)^2 - \cdots]\int_{-\infty}^{\infty}\frac{dp}{2\pi}\{m(q|p)\times \\ &\quad \times[1 - X(p) + X(p)^2 - \cdots]m(p|k)\}[1 - X(k) + X(k)^2 - \cdots]a(k),\end{aligned} \tag{3.10b}$$

respectively. With the use of the definitions of $A(q|k)$ and $m(q|k)$ given by Eqs. (2.8), the definitions of $X(k)$ and $a(k)$ given by Eqs. (3.7b) and (3.8b), respectively, and the result

that

$$\{J(\gamma_1|Q_1)J(\gamma_2|Q_2)\} = 2\pi\delta(Q_1+Q_2)e^{-\frac{1}{2}(\gamma_1^2+\gamma_2^2)\delta^2}\int_{-\infty}^{\infty} du\, e^{-iQ_1u}(e^{-\gamma_1\gamma_2\delta^2 W(|u|)}-1), \quad (3.11)$$

we can rewrite Eqs. (3.10) compactly as

$$\langle B(q|k)\rangle_{(21)} = 2\pi\delta(q-k)\eta^2[e^{-2\alpha_0(k)\alpha(k)\delta^2}N(k)+R_0(k)M(k)] \quad (3.12a)$$

and

$$\langle B(q|k)\rangle_{(22)} = 2\pi\delta(q-k)\eta^2[e^{-2\alpha_0(k)\alpha(k)\delta^2}-1]R_0(k)M(k), \quad (3.12b)$$

respectively, where

$$M(k) = \int_{-\infty}^{\infty}\frac{dp}{2\pi}\hat{m}(k|p)\hat{m}(p|k)e^{-(\alpha(p)-\alpha(k))(\alpha_0(p)-\alpha_0(k))\delta^2}\times$$

$$\times\int_{-\infty}^{\infty} du e^{-i(k-p)u}[e^{-(\alpha(k)-\alpha_0(p))(\alpha(p)-\alpha_0(k))\delta^2 W(|u|)}-1] \quad (3.13a)$$

$$N(k) = \int_{-\infty}^{\infty}\frac{dp}{2\pi}\hat{m}(k|p)\hat{n}(p|k)e^{-(\alpha(p)-\alpha(k))(\alpha_0(p)+\alpha_0(k))\delta^2}\times$$

$$\times\int_{-\infty}^{\infty} du e^{-i(k-p)u}[e^{-(\alpha(k)-\alpha_0(p))(\alpha(p)+\alpha_0(k))\delta^2 W(|u|)}-1]. \quad (3.13b)$$

With the use of Eqs. (3.1), (3.9), and (3.12), we obtain the result that

$$\langle R(q|k)\rangle = 2\pi\delta(q-k)r(\theta_0), \quad (3.14)$$

where

$$r(\theta_0) = e^{-2\left(\frac{\omega\delta}{c}\right)^2\cos\theta_0(\cos^2\theta_0-\eta)^{\frac{1}{2}}}\left\{\frac{\epsilon\cos\theta_0-(\cos^2\theta_0-\eta)^{\frac{1}{2}}}{\epsilon\cos\theta_0+(\cos^2\theta_0-\eta)^{\frac{1}{2}}}+\right.$$

$$\left.+\eta^2\left[N\left(\frac{\omega}{c}\sin\theta_0\right)+\frac{\epsilon\cos\theta_0-(\cos^2\theta_0-\eta)^{\frac{1}{2}}}{\epsilon\cos\theta_0+(\cos^2\theta_0-\eta)^{\frac{1}{2}}}M\left(\frac{\omega}{c}\sin\theta_0\right)\right]+o(\eta^2)\right\}, \quad (3.15)$$

and we have used the fact that $k=(\omega/c)\sin\theta_0$. When the result given by Eq. (3.14) is substituted into Eq. (2.2a), the contribution to the mean drc from the coherent component of the scattered x-rays becomes

$$\left\langle\frac{\partial R}{\partial\theta_s}\right\rangle_{coh} = \delta(\theta_s-\theta_0)R(\theta_0), \quad (3.16)$$

where the reflectivity $R(\theta_0)$ is given by

$$R(\theta_0) = |r(\theta_0)|^2. \tag{3.17}$$

4. Incoherent Scattering

When we substitute Eq. (2.6) into Eq. (2.2b) we find that the contribution to the mean drc from the incoherent component of the scattered field can be expressed equivalently as

$$\left\langle \frac{\partial R}{\partial \theta_s} \right\rangle_{incoh} = \frac{1}{L_1} \frac{\omega}{2\pi c} \frac{\cos^2 \theta_s}{\cos \theta_0} [\langle |B(q|k)|^2 \rangle - |\langle B(q|k) \rangle|^2]. \tag{4.1}$$

To obtain $\langle |B(q|k)|^2 \rangle$ we square the modulus of the right hand side of Eq. (2.9), and average the resulting series term-by-term:

$$\begin{aligned} \langle |B(q|k)|^2 \rangle &= \eta^2 \langle A(q|k) A^*(q|k) \rangle + \\ &+ \eta^3 [\langle A(q|k) \int_{-\infty}^{\infty} \frac{dr_1}{2\pi} m^*(q|r_1) A^*(r_1|k) \rangle + \\ &+ \langle \int_{-\infty}^{\infty} \frac{dp_1}{2\pi} m(q|p_1) A(p_1|k) A^*(q|k) \rangle] + \cdots \end{aligned} \tag{4.2}$$

From the explicit expressions for $A(q|k)$ and $m(q|k)$ obtained from Eqs. (2.8a)-(2.8c), we see that the coefficient of η^n on the right hand side of Eq. (4.2), where $n \geq 2$, is the sum of $n-1$ terms of which the m^{th} contains the average of a product of m $J(\gamma|Q)$'s and $n-m$ $J^*(\gamma|Q)$'s. These averages are very similar to the average of a product of n $J(\gamma|Q)$'s encountered in obtaining the average $\langle B(q|k) \rangle$. They consist of the product of the averages of the n individual factors, plus the sum of terms in which two factors are paired, and the correlated part of the average of their product is multiplied by the product of the averages of the remaining $n-2$ factors, and so on. Since what we really need is not $\langle |B(q|k)|^2 \rangle$ but the difference $\langle |B(q|k)|^2 \rangle - |\langle B(q|k) \rangle|^2$, the first category of averages described can be omitted, since it does not contribute to this difference. The second category of averages does, but only if one of the factors in the pair whose correlated average is evaluated is unconjugated while the second is complex conjugated. The $n-2$ delta functions associated with the

product of the averages of the remaining $n-2$ factors that are unpaired yield a result that is proportional to $1/\eta^{n-2}$ which, combined with the factor of η^n multiplying the n^{th} order term produces a contribution of $O(\eta^2)$ to $\langle|B(q|k)|^2\rangle - |\langle B(q|k)\rangle|^2$ from each term on the right hand side of Eq. (4.2). Thus, an infinite series of terms must be summed to obtain the contribution to $\langle|B(q|k)|^2\rangle - |\langle B(q|k)\rangle|^2$ of the lowest nonzero order in η, namely the second.

Four classes of terms contribute to $\langle|B(q|k)|^2\rangle - |\langle B(q|k)\rangle|^2$ in this order, defined by the two factors that appear in the pair whose correlated average is evaluated. They can be written schematically as $\{AA^*\}, \{mA^*\}, \{Am^*\}$, and $\{mm^*\}$. These four categories of terms can be summed to yield the result that to $O(\eta^2)$

$$
\begin{aligned}
&\langle|B(q|k)|^2\rangle - |\langle B(q|k)\rangle|^2 \\
&= \eta^2[[1 - X(q) + X(q)^2 - \cdots]\{A(q|k)[1 - X^*(q) + X^*(q)^2 - \cdots]A^*(q|k)\} + \\
&\quad + [1 - X(q) + X(q)^2 - \cdots]\{m(q|k)[1 - X(k) + X(k)^2 - \cdots]a(k) \times \\
&\quad \times [1 - X^*(q) + X^*(q)^2 - \cdots]A^*(q|k)\} + \\
&+[1 - X(q) + X(q)^2 - \cdots]\{A(q|k)[1 - X^*(q) + X^*(q)^2 - \cdots]m^*(q|k)\} \times \\
&\quad \times [1 - X^*(k) + X^*(k)^2 - \cdots]a^*(k) + \\
&\quad + [1 - X(q) + X(q)^2 - \cdots]\{m(q|k)[1 - X(k) + X(k)^2 - \cdots]a(k) \times \\
&\quad \times [1 - X^*(q) + X^*(q)^2 - \cdots]m^*(q|k)\}[1 - X^*(k) + X^*(k)^2 - \cdots]a^*(k)] \\
&= \eta^2 \frac{1}{|1 + X(q)|^2} \frac{1}{|1 + X(k)|^2} \{[A(q|k)(1 + X(k)) + m(q|k)a(k)] \times \\
&\quad \times [A^*(q|k)(1 + X^*(k)) + m^*(q|k)a^*(k)]\}, \qquad (4.3)
\end{aligned}
$$

where the curly bracket symbol has been defined in Eq. (3.4). With the use of the explicit expressions for $X(k)$ and $a(k)$, Eqs. (3.7b) and (3.8b), respectively, we can rewrite Eq. (4.3)

in the form

$$\langle|B(q|k)|^2\rangle - |\langle B(q|k)\rangle|^2 = \eta^2\, e^{Re(\alpha(q)-\alpha_0(q))^2\delta^2} e^{Re(\alpha(k)-\alpha_0(k))^2\delta^2} \times$$

$$\times\{[e^{-\frac{1}{2}(\alpha^2(k)+\alpha_0^2(k))\delta^2} b(q|k)][e^{-\frac{1}{2}(\alpha^2(k)+\alpha_0^2(k))\delta^2} b(q|k)]^*\}, \tag{4.4a}$$

where

$$b(q|k) = \cosh(\alpha(k)\alpha_0(k)\delta^2)[n(q|k) + m(q|k)R_0(k)] +$$

$$+ \sinh(\alpha(k)\alpha_0(k)\delta^2)[n(q|k) - m(q|k)R_0(k)]. \tag{4.4b}$$

As it stands, the result given by Eq. (4.4) is not reciprocal. Reciprocity, which is a consequence of the Lorentz reciprocity theorem [16], requires that the scattering matrix $S(q|k)$ defined by

$$S(q|k) = \frac{\alpha_0^{\frac{1}{2}}(q)}{\alpha_0^{\frac{1}{2}}(k)} R(q|k) \tag{4.5}$$

must satisfy the relation

$$S(q|k) = S(-k|-q). \tag{4.6}$$

In view of Eq. (2.6) this condition requires that

$$\langle|B(-k|-q)|^2\rangle - |\langle B(-k|-q)\rangle|^2$$

$$= \frac{\alpha_0^2(q)}{\alpha_0^2(k)}[\langle|B(q|k)|^2\rangle - |\langle B(q|k)\rangle|^2]. \tag{4.7}$$

The result given by Eq. (4.4) does not satisfy this condition.

However, it is possible to transform Eq. (4.4) into a form that is manifestly reciprocal. We begin by noting that with the use of the expansion of $J(\gamma|Q)$ in powers of γ,

$$J(\gamma|Q) = \sum_{n=1}^{\infty} \frac{(-i)^n}{n!} \gamma^n \hat{\zeta}^{(n)}(Q), \tag{4.8}$$

where

$$\hat{\zeta}^{(n)}(Q) = \int_{-\infty}^{\infty} dx_1 e^{-iQx_1} \zeta^n(x_1), \tag{4.9}$$

and the use of the relation

$$\alpha_0^2(k) = \alpha^2(k) + \eta\frac{\omega^2}{c^2}, \tag{4.10}$$

together with the fact that $\epsilon = 1 - \eta$, we find that

$$n(q|k) + m(q|k)R_0(k) = \frac{qk - \alpha(q)\alpha(k)}{d(q)d(k)}\frac{J(\alpha(q) + \alpha(k)|q-k)}{\alpha(q) + \alpha(k)}2\alpha_0(k) + O(\eta) \tag{4.11a}$$

$$n(q|k) - m(q|k)R_0(k) = \frac{qk - \alpha(q)\alpha(k)}{d(q)d(k)}\frac{J(\alpha(q) + \alpha(k)|q-k)}{\alpha(q) + \alpha(k)}2\alpha(k) + O(\eta). \tag{4.11b}$$

Since we seek a result correct to the lowest order in η, we neglect the corrections to these results of $O(\eta)$. It follows, therefore, that

$$\begin{aligned}
&e^{-\frac{1}{2}(\alpha^2(k)+\alpha_0^2(k))\delta^2} b(q|k) \\
&= \frac{qk - \alpha(q)\alpha(k)}{d(q)d(k)}\frac{J(\alpha(q) + \alpha(k)|q-k)}{\alpha(q) + \alpha(k)} \times \\
&\times[(\alpha_0(k) + \alpha(k))e^{-\frac{1}{2}(\alpha(k)-\alpha_0(k))^2\delta^2} + \\
&\quad + (\alpha_0(k) - \alpha(k))e^{-\frac{1}{2}(\alpha(k)+\alpha_0(k))^2\delta^2}] \\
&= \frac{qk - \alpha(q)\alpha(k)}{d(q)d(k)}\frac{J(\alpha(q) + \alpha(k)|q-k)}{\alpha(q) + \alpha(k)} \times \\
&\times[2\alpha_0(k) - (\alpha_0^2(k) - \alpha^2(k))\sum_{n=1}^{\infty}\frac{1}{n!}\left(-\frac{\delta^2}{2}\right)^n \times \\
&\quad \times [(\alpha(k) - \alpha_0(k))^{2n-1} - (\alpha(k) + \alpha_0(k))^{2n-1}]].
\end{aligned} \tag{4.12}$$

However, in view of Eq. (4.10), the second term in brackets is of $O(\eta)$ and we neglect it. Thus, finally,

$$\begin{aligned}
&\langle|B(q|k)|^2\rangle - |\langle B(q|k)\rangle|^2 = \eta^2 e^{Re(\alpha(q)-\alpha_0(q))^2\delta} e^{Re(\alpha(k)-\alpha_0(k))^2\delta^2} \times \\
&\times\left|2\alpha_0(k)\frac{qk - \alpha(q)\alpha(k)}{d(q)d(k)}\right|^2\left\{\frac{J(\alpha(q) + \alpha(k)|q-k)}{\alpha(q) + \alpha(k)}\frac{J^*(\alpha(q) + \alpha(k)|q-k)}{\alpha^*(q) + \alpha^*(k)}\right\}.
\end{aligned} \tag{4.13}$$

In this form, the reciprocity condition (4.7) is manifestly satisfied.

With the result that

$$\{J(\gamma|Q)J^*(\gamma|Q)\} \;=\; L_1\, e^{-\frac{1}{2}(\gamma^2+\gamma^{*2})\delta^2} \int_{-\infty}^{\infty} du e^{-iQu}[e^{|\gamma|^2\delta^2 W(|u|)} - 1], \qquad (4.14)$$

together with the result given by Eq. (4.1), we can write the contribution to the mean differential reflection coefficient from the incoherent component of the scattered x-rays to $O(\eta^2)$ as

$$\left\langle \frac{\partial R}{\partial \theta_s} \right\rangle_{incoh} \;=\; \eta^2 \frac{1}{8\sqrt{\pi}} \left(\frac{\omega a}{c}\right) \frac{1}{\cos\theta_0} \sum_{n=1}^{\infty} \left(\frac{\omega\delta}{c}\right)^{2n} \frac{e^{-\frac{(q-k)^2a^2}{4n}}}{n!\sqrt{n}} |\tilde{b}_n(\theta_s,\theta_0)|^2, \qquad (4.15a)$$

where

$$\begin{aligned}
\tilde{b}_n(\theta_s,\theta_0) \;=\; & e^{-\frac{1}{2}\left(\frac{\omega\delta}{c}\right)^2[(\cos^2\theta_s-\eta)^{\frac{1}{2}}+(\cos^2\theta_0-\eta)^{\frac{1}{2}}]^2} \times \\
& \times e^{\frac{1}{2}\left(\frac{\omega\delta}{c}\right)^2[(\cos^2\theta_s-\eta)^{\frac{1}{2}}-\cos\theta_s]^2} e^{\frac{1}{2}\left(\frac{\omega\delta}{c}\right)^2[(\cos^2\theta_0-\eta)^{\frac{1}{2}}-\cos\theta_0]^2} \times \\
& \times 2\cos\theta_s \frac{\sin\theta_s\sin\theta_0 - (\cos^2\theta_s-\eta)^{\frac{1}{2}}(\cos^2\theta_0-\eta)^{\frac{1}{2}}}{[\epsilon\cos\theta_s + (\cos^2\theta_s-\eta)^{\frac{1}{2}}][\epsilon\cos\theta_0 + (\cos^2\theta_0-\eta)^{\frac{1}{2}}]} 2\cos\theta_0 \times \\
& \times [(\cos^2\theta_s-\eta)^{\frac{1}{2}} + (\cos^2\theta_0-\eta)^{\frac{1}{2}}]^{n-1}. \qquad (4.15b)
\end{aligned}$$

In obtaining the result given by Eq. (4.15) we have used the Gaussian form for the surface height autocorrelation function given by $W(|u|) = \exp(-u^2/a^2)$.

We can simplify Eq. (4.15) somewhat if we note that

$$(\cos^2\theta_{0,s}-\eta)^{\frac{1}{2}} - \cos\theta_{0,s} = \frac{-\eta}{(\cos^2\theta_{0,s}-\eta)^{\frac{1}{2}} + \cos\theta_{0,s}}. \qquad (4.16)$$

Consequently, we can replace the second and third exponential factors on the right hand side of Eq. (4.15b) by unity, in the approximation we are maintaining here. These replacements are equivalent to the assumption that $(\omega\delta/c)\sqrt{\eta(\omega)} \ll 1$. We can also replace the explicit factors of ϵ in the denominator of Eq. (4.15b) by unity to the same degree of approximation. As a result, we obtain finally

$$\tilde{b}_n(\theta_s,\theta_0) \;=\; e^{-\frac{1}{2}\left(\frac{\omega\delta}{c}\right)^2[(\cos^2\theta_s-\eta)^{\frac{1}{2}}+(\cos^2\theta_0-\eta)^{\frac{1}{2}}]^2} \times$$

$$\times 2\cos\theta_s \frac{\sin\theta_s \sin\theta_0 - (\cos^2\theta_s - \eta)^{\frac{1}{2}}(\cos^2\theta_0 - \eta)^{\frac{1}{2}}]}{[\cos\theta_s + (\cos^2\theta_s - \eta)^{\frac{1}{2}}][\cos\theta_0 + (\cos^2\theta_0 - \eta)^{\frac{1}{2}}]} 2\cos\theta_0 \times$$

$$\times[(\cos^2\theta_s - \eta)^{\frac{1}{2}} + (\cos^2\theta_0 - \eta)^{\frac{1}{2}}]^{n-1}, \tag{4.17}$$

In this form, Eq. (4.17) also applies to the scattering of x-rays of $s-$polarization when both θ_0 and θ_s are close to $\pi/2$, so that the factor $\sin\theta_s \sin\theta_0 - (\cos^2\theta_s - \eta)^{1/2}(\cos^2\theta_0 - \eta)^{1/2}$ is close to unity.

5. Results

In Section 3 we have obtained explicit expressions for the contributions to the mean scattering amplitude $\langle R(q|k)\rangle$ that are of zero and second order in $\eta(\omega)$. The contribution to the reflectivity from the zero-order term, obtained from Eqs. (3.15) and (3.17),

$$R(\theta_0) = \left|\frac{\epsilon\cos\theta_0 - (\cos^2\theta_0 - \eta)^{\frac{1}{2}}}{\epsilon\cos\theta_0 + (\cos^2\theta_0 - \eta)^{\frac{1}{2}}}\right|^2 e^{-4\left(\frac{\omega\delta}{c}\right)^2 \cos\theta_0 Re(\cos^2\theta_0 - \eta)^{\frac{1}{2}}}, \tag{5.1}$$

has the form of the Fresnel reflectivity multiplied by a factor similar to the Debye-Waller factor, and coincides with the result obtained in [6,7]. However, while in [6,7] this result was obtained in the first-order distorted wave Born approximation as an approximate result (the so-called "q-q_t" expansion), valid only for relatively weakly rough surfaces, $(\delta/\lambda)\cos\theta_0 \leq 1$, we have summed all the terms in the perturbation series for the mean scattering amplitude which are of zero order in $\eta(\omega)$ without imposing any restrictions on the rms height of the surface beyond the one implied by our adoption of the Rayleigh hypothesis.

For a lossless medium the reflectivity given by Eq. (5.1) becomes equal to unity when the angle of incidence θ_0 is equal to or greater than the critical angle for total internal reflection $\theta_0 = \cos^{-1}\sqrt{\eta}$, at which the term $(\cos^2\theta_0 - \eta)^{\frac{1}{2}}$ goes to zero and then becomes pure imaginary for $\theta_c < \theta_0 < \pi/2$. This is because the Fresnel reflectivity is unity in this range of angles of incidence, while the exponent of the "Debye-Waller" factor vanishes. In Fig. 2(a) the reflectivity given by Eq. (5.1), calculated for a one-dimensional, randomly rough gold surface, is plotted for different values of the roughness parameters, as a function

of the grazing angle of incidence $\bar{\theta}_0 = \pi/2 - \theta_0$. We see that it is equal to unity for $\bar{\theta}_0 < \bar{\theta}_c$, where $\bar{\theta}_c$ is the grazing critical angle for total internal reflection, and then decreases rapidly for $\bar{\theta}_0 > \bar{\theta}_c$, the rate of decrease increasing with increasing surface roughness.

The lowest order correction to the reflectivity given by Eq. (5.1) is of second order in $\eta(\omega)$, as can be seen from Eqs. (3.15) and (3.17). Although this correction is small, it is important because it describes the decrease of the reflectivity from unity in the regime of total internal reflection. In addition, since this correction depends on the surface height autocorrelation function $W(|x_1|)$, in contrast with the result given by Eq. (5.1) which does not, and which can therefore be used to determine only the rms height of the surface, an experimental determination of it affords the possibility of determining $W(|x_1|)$, or at least the transverse correlation length a of the surface roughness. In Fig. 2(b) we have plotted $1 - R(\bar{\theta}_0)$

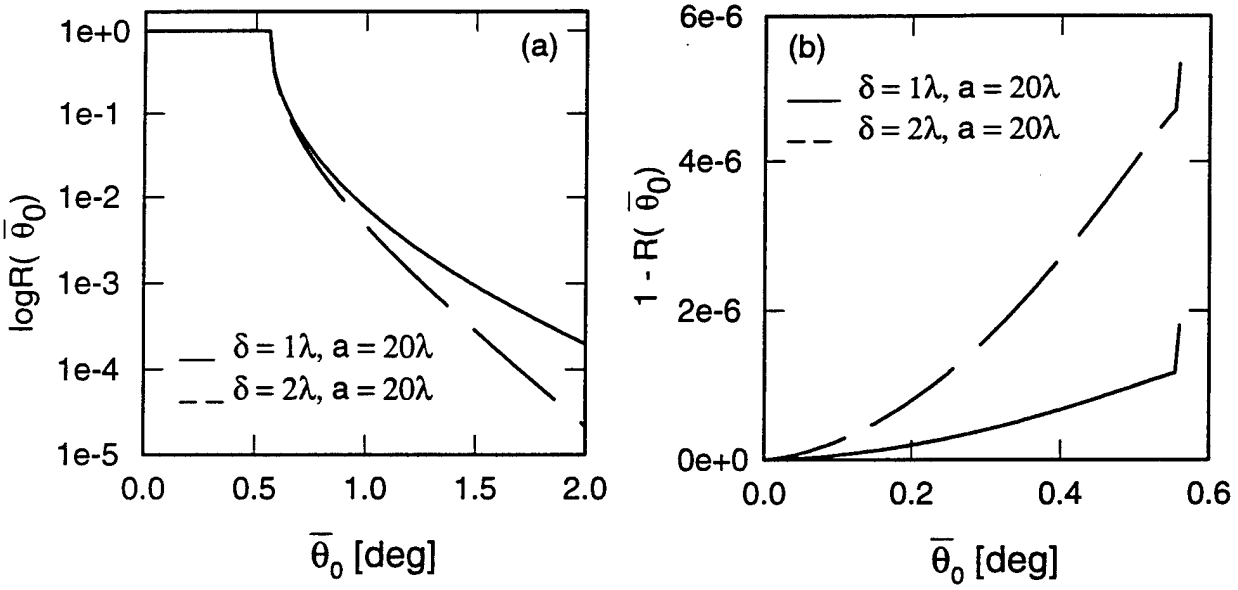

Fig.2 (a) The reflectivity (5.1) of a one-dimensional randomly rough gold surface illuminated by p-polarized x-rays of wavelength $\lambda = 1.54\mathring{A}$, as a function of the grazing angle of incidence $\bar{\theta}_0 = \pi/2 - \theta_0$. The surface roughness is characterized by a transverse correlation length $a = 20\lambda$, and two values of the rms height $\delta = \lambda, 2\lambda$. (b) A plot

of $1 - R(\bar{\theta}_0)$ for grazing angles of incidence smaller than, and a bit larger than, $\bar{\theta}_c$, calculated by including both the zero- and second-order terms in Eq. (3.15) in the evaluation of Eq. (3.17). $\bar{\theta}_c = 0.52°$.

for grazing angles of incidence $\bar{\theta}_0$ smaller than, and a bit larger than, $\bar{\theta}_c$, calculated by including both the zero-order and second-order terms in $\eta(\omega)$ in Eq. (3.15) in the evaluation of Eq. (3.17). This decrease, as might be expected, is larger the rougher the surface.

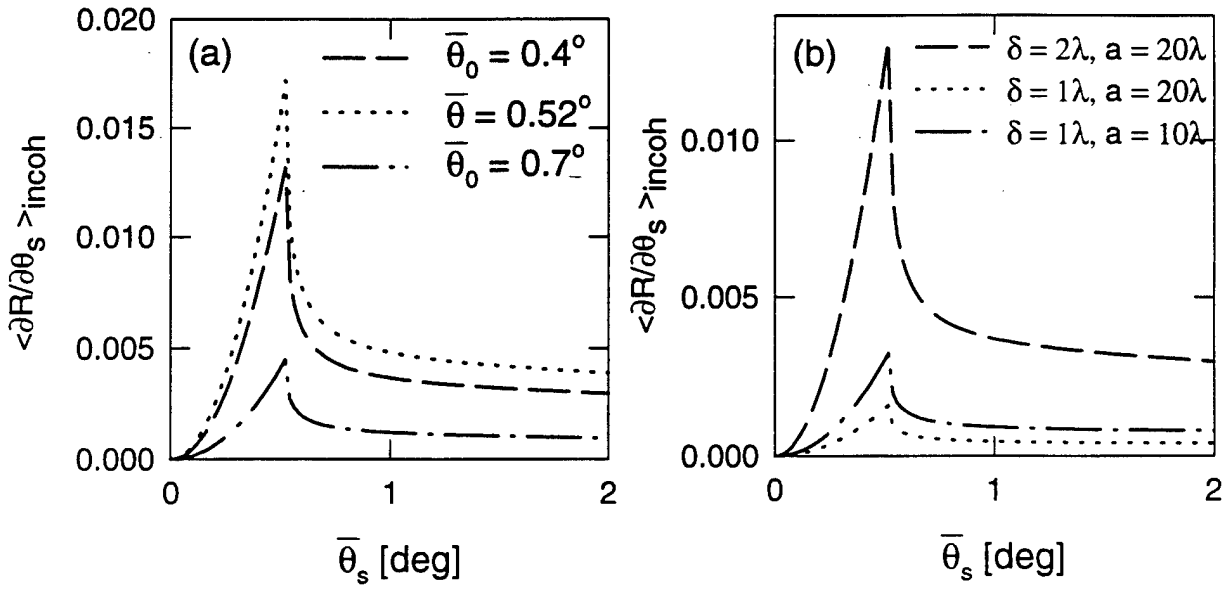

Fig.3 The contribution to the mean drc from the incoherent component of the scattered x-rays as a function of the grazing scattering angle $\bar{\theta}_s = \pi/2 - \theta_s$, when p-polarized x-rays of wavelength $\lambda = 1.54\mathring{A}$ are incident on a one-dimensional randomly rough gold surface characterized by an rms height $\delta = 2\lambda$ and a transverse correlation length $a = 20\lambda$, (a) for several grazing angles of incidence $\bar{\theta}_0$ and (b) for a fixed grazing angle of incidence $\bar{\theta}_0 = 0.4°$ for several values of the roughness parameters.

We now turn to the contribution to the mean differential reflection coefficient from the incoherent component of the scattered x-rays, given by Eqs. (4.15a,b) and (4.17). It has

been calculated to the lowest order in $\eta(\omega)$ (the second), and its reciprocal form, given by Eq.(4.17), has been derived in the limit $(\delta/\lambda)\sqrt{\eta(\omega)} \ll 1$. In this form our result differs only by the factor $\sin\theta_s \sin\theta_0 - (\cos^2\theta_s - \eta)^{\frac{1}{2}}(\cos^2\theta_0 - \eta)^{\frac{1}{2}}$ from the results obtained in the first-order distorted wave Born approximation, or the modified Born approximation, in the limit of a weakly rough surface $(\delta/\lambda)\cos\theta_0 \ll 1$ [2,6]. As in the case of the reflectivity, our result for the incoherent scattering is not limited by this condition. However, at small grazing angles of incidence and scattering where our results coincide with the results of the first-order distorted wave Born approximation, or the modified Born approximation, the two limiting conditions are practically identical, because for such angles $\cos\theta_{0,s} \leq \sqrt{\eta(\omega)}$. We note, however, that the expression (4.15b) remains valid even when the inequality $(\delta/\lambda)\sqrt{\eta(\omega)} \ll 1$ breaks down.

In Fig. 3(a) we plot the contribution to the mean differential reflection coefficient from the incoherent component of the scattered x-rays as a function of the scattering angle for different grazing angles of incidence, and in Fig. 3(b) for different values of the roughness parameters. The plots show the sharp asymmetric peak at $\theta_s = \theta_c$, called the Yoneda peak [3]. It is easy to see that this peak arises from the sharp feature at $\theta_{s,0} = \theta_c$ in the factors $|2\cos\theta_{s,0}/[\epsilon(\omega)\cos\theta_{s,0} + \sqrt{\cos^2\theta_{s,0} - \eta(\omega)}|^2$ present in the function $\tilde{b}_n(\theta_s, \theta_0)$, which are the Fresnel transmission coefficients that determine the field at the surface.

6. Conclusions

In this work we have presented a simple reciprocal theory of the scattering of x-rays from a one-dimensional randomly rough surface. This has been accomplished by solving the reduced Rayleigh equation for the scattering of electromagnetic waves from such a surface not as an expansion in powers of the surface profile function, but as an expansion in powers of the small parameter $\eta(\omega) = 1 - \epsilon(\omega)$. However, in carrying out this expansion we have been careful not to expand the functions $\alpha(k) = (\omega/c)(\cos^2\theta_0 - \eta)^{\frac{1}{2}}$ and $\alpha(q) = (\omega/c)(\cos^2\theta_s - \eta)^{\frac{1}{2}}$ appearing in the solution in powers of η. This is because it is the vanishing of these functions when θ_0 and θ_s equal the critical angle for total internal reflection at the interface between vacuum and the scattering medium, $\theta_c = \cos^{-1}\eta^{\frac{1}{2}}$, and their transformation into pure imaginary

quantities for θ_0 or θ_s greater than θ_c, that gives rise to the Yoneda peak in the angular distribution of the intensity of the x-rays scattered diffusely.

The results obtained here are valid at small angles of incidence and scattering, like the results of the Born approximation but, unlike the results of the Born approximation, are also valid in the vicinity of the critical angle for total internal reflection θ_c. In their validity for small grazing angles of incidence and scattering, our results also contrast with the results of the distorted wave Born approximation.

Although the derivation of the results obtained here has been carried out in the context of the scattering of electromagnetic waves from solid surfaces, the results of the corresponding theory for two-dimensional random surfaces can also be applied to the scattering of x-rays from liquid surfaces, if the corresponding power spectrum for the surface roughness is used. The latter has the form [17]

$$\begin{aligned} g(|\vec{k}_{||}|) &= \int d^2x_{||} W(|\vec{x}_{||}|) e^{-i\vec{k}_{||}\cdot\vec{x}_{||}} \\ &= \frac{k_B T}{\gamma} \frac{\theta(k_c - |\vec{k}_{||}|)}{\kappa^2 + k_{||}^2}, \end{aligned} \tag{6.1}$$

where $W(|\vec{x}_{||}|)$ is the surface height autocorrelation function, γ is the surface tension of the liquid at the absolute temperature T, k_B is Boltzmann's constant, and $\kappa = (g\rho/\gamma)^{\frac{1}{2}}$ is the gravitational cutoff, with ρ the mass density of the liquid, and g the acceleration due to gravity. $\theta(x)$ is the Heaviside unit step function, and the wavenumber k_c is the upper wave vector cutoff for the thermally excited surface waves (surface ripplons) whose amplitudes roughen the liquid surface. The value of k_c is of the order of the reciprocal of a few atomic diameters [18].

Finally, it seems likely that the approach used here, namely the expansion of the scattering amplitude in powers of $\eta(\omega)$, may also be useful in theoretical studies of the multiple scattering of electromagnetic waves incident from one dielectric medium onto a randomly rough interface with a different dielectric medium, when the difference between their dielectric constants is small, of the order of a few tenths, say. In such a case the leading corrections to the term of second order in $\eta(\omega)$ obtained here for the contribution to the mean differ-

ential reflection coefficient from the incoherent component of the scattered electromagnetic field may be sufficient to predict the enhanced backscattering of light from such interfaces that has been observed in the results of computer simulation calculations when the medium of incidence is the optically denser medium [19]. The dielectric contrast would then serve as a new small parameter in theory of the multiple scattering of electromagnetic waves from such interfaces.

References

1. Xiao-Lin Zhou and Sow-Hsin Chen, Phys. Rep. **257**, 224 (1995).

2. S. Dietrich and A. Haase, Phys. Rep. **260**, 1 (1995).

3. Y. Yoneda, Phys. Rev. **131**, 2010 (1963).

4. O. J. Guentert, J. Appl. Phys. **36**, 1361 (1963).

5. A. N. Nigam. Phys. Rev. **A4**, 1189 (1965).

6. S. K. Sinha, E. B. Sirota, S. Garoff, and H. B. Stanley, Phys. Rev. **B 38**, 2297 (1988).

7. L. Nevot and P. Croce, Rev. Phys. Appl. **15**, 761 (1980).

8. J. B. Kortright, J. Appl. Phys. **70**, 3620 (1991).

9. M. K. Sanayal, S. K. Sinha, K. G. Huang, and B. M. Ocho, Phys. Rev. Lett. **66**, 628 (1991).

10. F. Toigo, A. Marvin, V. Celli, and N. R. Hill, Phys. Rev. B**15**, 5618 (1977).

11. Lord Rayleigh, *The Theory of Sound*, 2nd ed. (Macmillan, London, 1896), Vol II, pp. 89 and 297-311.

12. Lord Rayleigh, Proc. Roy. Soc. (London) A**79**, 399 (1907).

13. R. Petit and M. Cadilhac, C. R. Acad. Sci. Paris, B**262**, 468 (1966).

14. R. F. Millar, Proc. Camb. Phil. Soc. **65**, 773 (1969); *ibid.* **69**, 217 (1971); Radio Sci. **8**, 785 (1973).

15. N. R. Hill and V. Celli, Phys. Rev. B**17**, 2478 (1978).

16. See, for example, M.Nieto-Vesperinas, *Scattering and Diffraction in Physical Optics* (Wiley, New York, 1991), p.8.

17. This result is implicit in the results presented, e.g., in C.A. Croxton, *Statistical Mechanics of the Liquid Surface* (Wiley, New York, 1980), pp. 77-79.

18. H. T. Davis, J. Chem. Phys. **67**, 3636 (1977).

19. M. Nieto-Vesperinas and J. A. Sánchez-Gil, J. Opt. Soc. Am. A**9**, 424 (1992).

Coherent Effects In Closed Systems With Rough Boundaries

V. Freilikher
The Jack and Pearl Resnick Institute of Advanced Technology
Department of Physics, Bar-Ilan University, Ramat-Gan 52900, Israel

In this presentation we consider theoretically the statistics of a wave field inside a totally closed system (microwave or acoustic resonator, or quantum dot) with randomly rough boundaries. The study is carried out in the framework of the random matrix theory (RMT) approach.

RMT is a powerful and very general non-perturbative method for the exploration of the statistical properties of complex random systems. The starting point (and one of the most complicated and nontrivial steps in the method) is to map the initial microscopic physical problem onto its random-matrix analogue. When the mapping is done, one can use many of the results known in RMT.

The central observation of random matrix theory that allows mapping a microscopic electrodynamic or quantum problem onto an RMT-model is that many physical properties of a real system described by a microscopic Hamiltonian $\mathcal{H}$ with eigenlevels ϵ_n can be reproduced by studying ensembles of $N \times N$ random matrices $\mathbf{H}$ with the same eigenvalues [1]. These random matrices should reflect the underlying symmetry of the system under study, i.e. of the microscopic Hamiltonian $\mathcal{H}$. At the present time the most studied are random matrix ensembles corresponding to systems with time reversal symmetry, and with broken (for example, due to absorption or a magnetic field) time-reversal symmetry. In the RMT it is common to denote these cases by a parameter β that is equal to 1 and 2, respectively.

What about the eigenfunctions in this approach? To clear up this issue let us consider the wave equation for a closed system, which in its most general form reads $\mathcal{H}\Psi_n(\mathbf{r}) = \epsilon_n \Psi_n(\mathbf{r})$, and diagonalize the corresponding random matrix $\mathbf{H}$ according to $\mathbf{H} = UEU^{\dagger}$, where E is a diagonal matrix $diag(\epsilon_1, ..., \epsilon_N)$. Since $\mathbf{H}U = UE$, or $\sum_{k=1}^{N} H_{ik}U_{kj} = \epsilon_j U_{ij}$, we can rewrite this equation in a different form by defining $U_{ij} = \phi_j(i)$ and making the replacements $i \to r$, $k \to r'$. Then we get $\sum_{r'=1}^{N} H_{rr'}\phi_j(r') = \epsilon_j \phi_j(r)$. Comparison of this equation with the initial one implies that the $\phi_j(r)$ play the role of the eigenfunctions of the initial microscopic problem provided that the space is divided into N boxes with radius vectors r that are numbered from 1 to N. In what follows it is more convenient to deal with the normalization fixed by the identity $\Psi_n(\mathbf{r}) \to (N/V)^{1/2} U_{nr}^{(\beta)}$, where $U^{(\beta)}$ is the real orthogonal ($\beta = 1$) or unitary ($\beta = 2$) matrix that diagonalizes $\mathbf{H}$ [2]. In the mapping described above the averaging over random surface roughness is replaced by averaging over the ensemble of random matrices of Wigner-Dyson type [1].

We consider the time-space evolution of a pulse (wave packet) radiated by a point source located at a point $\mathbf{r}'$ inside a cavity with perfectly reflecting randomly rough boundaries. The field of the pulse $\Phi(\mathbf{r}, \mathbf{r}'; t)$ is described by the wave equation

$$\left(\Delta - \frac{1}{c^2}\frac{\partial^2}{\partial t^2}\right)\Phi(\mathbf{r}, \mathbf{r}'; t) = 4\pi\delta(\mathbf{r} - \mathbf{r}')\,A(t),$$

with the condition $\Phi(\mathbf{r},\mathbf{r}';t)=0$ at the boundaries.

The average intensity $\langle I(\mathbf{r},\mathbf{r}';t)\rangle = \langle|\Phi(\mathbf{r},\mathbf{r}';t)|^2\rangle$ can be written as the integral

$$\langle I(\mathbf{r},\mathbf{r}';t)\rangle = \frac{1}{(2\pi)}\int d\Omega d\Omega' e^{it(\Omega-\Omega')}\langle G(\mathbf{r},\mathbf{r}';\Omega)\,G^*(\mathbf{r},\mathbf{r}';\Omega')\rangle\,\varphi(\Omega)\,\varphi*(\Omega'). \qquad (1)$$

Here

$$\varphi(\Omega)=\int dt e^{i\Omega t}A(t),$$

and $G(\mathbf{r},\mathbf{r}',\Omega)$ obeys the equation

$$\left(\Delta+\frac{\Omega^2}{c^2}\right)G(\mathbf{r},\mathbf{r}';\Omega)=4\pi\delta(\mathbf{r}-\mathbf{r}').$$

The correlator $\tilde{P}_\beta(\mathbf{r},\mathbf{r}';\Omega,\Omega')=\langle G(\mathbf{r},\mathbf{r}';\Omega)\,G^*(\mathbf{r},\mathbf{r}';\Omega')\rangle$ can be expressed through the exact eigenfunctions $\Psi_n(\mathbf{r})$ of the system with eigenlevels ω_n, provided that

$$G(\mathbf{r},\mathbf{r}';\Omega)=\sum_n\frac{\Psi_n(\mathbf{r})\,\Psi_n^*(\mathbf{r}')}{\frac{\Omega^2}{c^2}-\frac{\omega_n^2}{c^2}+i0}. \qquad (2)$$

Then the quantities that we have to calculate are mapped onto the RMT-model described above:

$$\tilde{P}_\beta(\mathbf{r},\mathbf{r}';\Omega,\Omega')=\frac{V\Delta^2}{2\pi c^2}\frac{N^2}{V^2}\left\langle\sum_n\sum_m\frac{U_{nr}^{(\beta)}U_{nr'}^{*(\beta)}U_{mr}^{*(\beta)}U_{mr'}^{(\beta)}}{\left[\frac{\Omega 2}{c^2}-\frac{\omega_n^2}{c^2}+i0\right]\left[\frac{\Omega^2}{c^2}-\frac{\omega_m^2}{c^2}-i0\right]}\right\rangle_{RME}, \qquad (3)$$

where V is the volume of the system, Δ is the mean level spacing, and

$$\left\langle F\left(U^{(\beta)},\{\epsilon\}\right)\right\rangle=\frac{\int dU^{(\beta)}\int\prod_{i=1}^N d\epsilon_i P_\beta(\{\epsilon\})\,F\left(U^{(\beta)},\{\epsilon\}\right)}{\int dU^{(\beta)}\int\prod_{i=1}^N d\epsilon_i P_\beta(\{\epsilon\})}. \qquad (4)$$

Here $dU^{(\beta)}$ is the Haar measure of the orthogonal or unitary group $U^{(\beta)}(N)$, $\epsilon_i=\omega_i^2/c^2$, $P_\beta(\{\epsilon\})=\frac{1}{Z}\prod_{i<j}|\epsilon_i-\epsilon_j|^\beta\prod_{i=1}^N\exp\{-\beta V(\epsilon_i)\}$, and $V(\epsilon)$ is the so-called strong confinement potential that behaves as or stronger than $|\epsilon|$ at infinity.

After the mapping has been carried out, i.e. after the ensemble average $\langle G(\mathbf{r},\mathbf{r}';\Omega)\,G^*(\mathbf{r},\mathbf{r}';\Omega')\rangle$ has been replaced by its RMT analogue Eq. (3) the following calculations become quite technical.

We sketch the RMT procedure below.

Since integration over the $U^{(\beta)}(N)$-group and integration over eigenlevels can be carried out independently we can write in the large-N limit that

$$\frac{1}{[\int dU^{(\beta)}]}\frac{N^2}{V^2}\int dU^{(\beta)}U_{nr}^{(\beta)}U_{nr'}^{*(\beta)}U_{mr}^{*(\beta)}U_{mr'}^{(\beta)}=\frac{1}{V^2}\left\{\delta_{nm}+(1+\delta_{\beta,1}\delta_{nm})\,\delta_{rr'}\right\}, \qquad (5)$$

postulating the existence of the Wick theorem. Then

$$\tilde{P}_\beta(\mathbf{r},\mathbf{r}';\omega)=\frac{1}{V}\left\{a(\omega)+\delta_{rr'}\left[b(\omega)+\delta_{\beta,1}a(\omega)\right]\right\}, \qquad (6)$$

where

$$a(\omega) = \frac{\Delta}{2\pi(\omega + i0)}\left[\mathcal{G}^{(-)}\left(E - \frac{\omega}{2}\right) - \mathcal{G}^{(+)}\left(E + \frac{\omega}{2}\right)\right] = \frac{i}{\omega + i0}, \tag{7}$$

$$b(\omega) = \frac{\Delta}{2\pi}\mathcal{G}^{(+-)}\left(E + \frac{\omega}{2}, E - \frac{\omega}{2}\right). \tag{8}$$

In equations (7) and (8)

$$\mathcal{G}^{(p)}(E) = \left\langle Tr\frac{1}{E - \mathbf{H} + ip0}\right\rangle_{RME} \tag{9}$$

is the one-point Green's function in RME, and

$$\mathcal{G}^{(pp')}(E, E') = \left\langle Tr\frac{1}{E - \mathbf{H} + ip0}Tr\frac{1}{E' - \mathbf{H} + ip'0}\right\rangle_{RMT} \tag{10}$$

is the two-point Green's function [1]; $p, p' = \pm 1$.

The mapping used above leads to the conclusion that the time dependence in Eq. (1) is governed by the equation

$$I(\mathbf{r}, \mathbf{r}'; t) = \left\{1 + \delta_{rr'}\left[\delta_{\beta,1} + \frac{\Delta}{2\pi}\int\frac{d\omega}{2\pi}e^{-i\omega t}\mathcal{G}^{(+-)}\left(E + \frac{\omega}{2}, E - \frac{\omega}{2}\right)\right]\right\}. \tag{11}$$

Making use of the definition Eq. (10) of the two-point Green's function it is easy to see that

$$\int\frac{d\omega}{2\pi}e^{-i\omega t}\mathcal{G}^{(+-)}\left(E + \frac{\omega}{2}, E - \frac{\omega}{2}\right) = \frac{2\pi}{\Delta}\left[1 - b_\beta\left(\frac{t\Delta}{2\pi}\right)\right], \tag{12}$$

where

$$b_\beta(z) = \int\frac{ds}{2\pi}e^{-isz}Y_2^{(\beta)}(s) \tag{13}$$

is the Fourier transform of the two-level cluster function, so that

$$I(\mathbf{r}, \mathbf{r}'; t) = \frac{1}{V}\left\{1 + \delta_{rr'}\left[\delta_{\beta,1} + 1 - b_\beta\left(\frac{t\Delta}{2\pi}\right)\right]\right\}. \tag{14}$$

Equation (14) can be rewritten in the form

$$I(\mathbf{r}, \mathbf{r}'; t) = \frac{1}{V}\left\{1 + \delta_{rr'}C_\beta(z)\right\}, \tag{15}$$

with

$$C_1(z) = 1 + z\left[2 - \ln(1 + 2z)\right]\Theta(1 - z) + \left[2 - z\ln\frac{2z + 1}{2z - 1}\right]\Theta(z - 1), \tag{16}$$

$$C_2(z) = z\Theta(1 - z) + \Theta(z - 1). \tag{17}$$

Equations (15) and (16) describe the time evolution of the field intensity in the resonator. In particular, the stationary distribution is given by $I(\mathbf{r}, \mathbf{r}'; \infty) = \frac{1}{V}\{1 + 3\delta_{rr'}\}$, which for $\mathbf{r}=\mathbf{r}'$ (at the point where the source is located) gives a factor of 3 enhancement, which

is in good agreement with the results of numerical simulations of the acoustic field in a reverberation room with rough walls [3].

If we deal with electrons in a quantum dot, then a magnetic field can break time-reversal symmetry, and therefore destroy partially the coherence of the scattered fields. This results, in accordance with Eq. (17) ($\beta = 2$), in a decrease from a factor of 3 to a factor of 2 in the coherent enhancement at the point $\mathbf{r}=\mathbf{r}'$.

The spatial correlations of the eigenfunction intensities in a closed system can also be computed in the RMT formalism.

1) The distribution function $P_\beta(v)$ of eigenfunction intensities is defined as

$$P_\beta(v) = \Delta \left\langle \sum_n \delta\left(v - V\left|\Psi_n(\mathbf{r})\right|^2\right) \delta(E-\epsilon_n) \right\rangle_{dis}, \tag{18}$$

and is given by

$$P_\beta(v) = \frac{\frac{\beta}{2}}{\Gamma\left(\frac{\beta}{2}\right)} \left(\frac{\beta v}{2}\right)^{\frac{\beta}{2}-1} \exp\left(-\frac{\beta v}{2}\right). \tag{19}$$

2) The joint distribution function of the eigenfunction intensities at two different spatial points

$$P_\beta(v, v'; \mathbf{r}, \mathbf{r}') = \Delta \left\langle \sum_n \delta\left(v - V\left|\Psi_n(\mathbf{r})\right|^2\right) \delta\left(v' - V\left|\Psi_n(\mathbf{r}')\right|^2\right) \delta(E-\epsilon_n) \right\rangle_{dis} \tag{20}$$

is given by the formula

$$P_\beta(v, v'; \mathbf{r}, \mathbf{r}') = P_\beta(v)\, P_\beta(v') + \delta_{rr'} P_\beta(v) \left[\delta(v - v') - P_\beta(v')\right]. \tag{21}$$

3) The conditional probability which describes the distribution of the wave function at a point $\mathbf{r}'$, $v' = V\left|\Psi_n(\mathbf{r}')\right|^2$, provided $v = V\left|\Psi_n(\mathbf{r})\right|^2$, is expressed as

$$P_{\beta v}(v'; \mathbf{r}, \mathbf{r}') = \frac{P_\beta(v, v'; \mathbf{r}, \mathbf{r}')}{P_\beta(v)} = P_\beta(v') + \delta_{rr'} \left[\delta(v - v') - P_\beta(v')\right]. \tag{22}$$

Then we can calculate the conditional averages $\langle v' \rangle_v$ and $\left\langle (\delta v')^2 \right\rangle_v = \left\langle (v' - \langle v' \rangle_v)^2 \right\rangle_v$:

$$\langle v' \rangle_v = 1 + \delta_{rr'}(v - 1), \quad \left\langle (\delta v')^2 \right\rangle_v = \frac{2}{\beta}(1 - \delta_{rr'}). \tag{23}$$

As can be seen, the conditional average $\langle v' \rangle_v$ is independent of the symmetry parameter β, and therefore we cannot distinguish the symmetry of the system from this quantity alone. In contrast, the study of the variance $\left\langle (\delta v')^2 \right\rangle_v$ tells us about the system symmetry due to the parameter $\frac{2}{\beta}$. Thus, fluctuations become weaker with symmetry lowering.

To conclude, the statistics of the wave field in closed systems with rough boundaries has been studied in the framework of the RMT approach. It is shown in particular that a "residual" coherence of the scattered fields manifests itself in the enhancement of the stationary distribution of the intensity of the wave packet at the point where the source is located. The height of the enhanced peak depends on the time-reversal symmetry of the system.

REFERENCES

[1] M. L. Mehta, *Random Matrices* (Academic Press, Boston, 1991).

[2] C. W. J. Beenakker, Random-matrix theory of quantum size effects on nuclear magnetic resonance in metal particles, preprint.

[3] R.L. Weaver, Phys. Rev. B**49**, p. 5881 (1994).

Detection of a Buried Target in a Random Medium Using Angular Correlation Function

Yasuo Kuga, Tsz-King Chan, Akira Ishimaru, and Chris Penwell

Department of Electrical Engineering
University of Washington
Box 352500
Seattle, WA 98195-2500

During the past several decades, extensive research has been conducted on radar detection and identification of a target embedded in clutter. When the clutter is located close to the target, the desired target return is masked by the clutter return, and discrimination becomes very difficult. This is particularly true if the target is not moving and Doppler processing, which is usually effective for detecting the moving target, is not applicable. A vehicle covered by a thick tree canopy is one example and a land mine placed on ground with a rough surface or buried under a ground cover is another example. Traditional radar technique which measures the backscattering radar cross section (RCS) at different frequencies is usually unable to discriminate a target response from that of the clutter. More advanced radars, including polarimetric, transient, and bistatic radars, have been tried with mixed success.

In this paper, we will discuss a new technique based on the angular correlation function (ACF) measurement for target detection in a homogeneous medium formed by sand particles. We evaluated the effectiveness of this approach by performing millimeter-wave experiments on the ACF measurement for the detection of a long conducting cylinder (diameter $\approx 1\lambda$) perpendicularly oriented to the plane of incidence. The cylinder was buried at a depth of about 1λ below the sand medium which has a flat sand-air interface, as shown in Fig. 1. Our results indicate that by measuring the ACF corresponding to an appropriate set of incident and scattering angles, the masking effect of the medium on the desirable target ACF return can be minimized, thus allowing successful target detection.

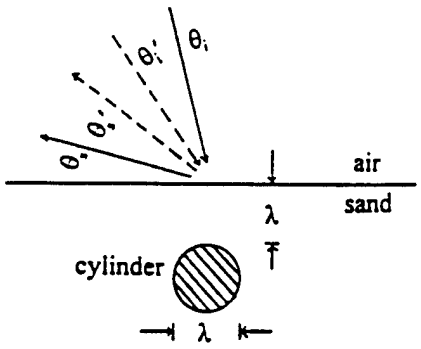

Fig. 1 Scattering geometry of the experimental setup

Recent studies showed that there is a memory effect associated with the angular dependence of multiply scattered waves from random rough surfaces in response to a change in the direction of the incident wave. This angular correlation phenomenon is known as the Angular Memory Effect and can be characterized by the ACF defined as $\Gamma(\theta_i,\theta_s;\theta_i',\theta_s') = \langle E_s(\theta_i,\theta_s)E_s^*(\theta_i',\theta_s')\rangle$ where $\Gamma(..)$ represents the angular correlation between the reference scattered wave observed at θ_S due to an incidence at θ_i and the variable scattered wave observed at θ_S' due to an incidence at θ_i', with angle brackets denoting an ensemble averaging operation. In general, the ACF or rough surface is negligibly small because of the phase cancellation due to multiple scattering, but becomes significant when the difference in the transverse wave numbers is the same for the incident and scattered waves. This condition can be stated as $k(\sin\theta_i' - \sin\theta_i) = k(\sin\theta_s' - \sin\theta_s)$. For a given pair of reference antenna positions (θ_i, θ_S), the ACF is, therefore, almost zero everywhere except along the line (the *angular memory line*) on the $\sin\theta_i' - \sin\theta_S'$ plane. The lateral width of this line is narrow and is on the order of λ/L, where L is the illumination width. In our experiments, λ/L is smaller than 1°, indicating rapid decorrelation away from the angular memory line. Since rough surface ACF is most significant when measurement is made along the angular memory line, in order to minimize the masking effect of the medium on the desirable target ACF return in the combined scene (medium together with the target), measurement should be made along a line (the *scan line*) which is *perpendicular* to the angular memory line. In this study, this scan line was chosen to be a straight line intersecting perpendicularly with the angular memory line at the reference antenna positions (θ_i = 20°, θ_S = –40°). These two lines are shown in Fig. 2.

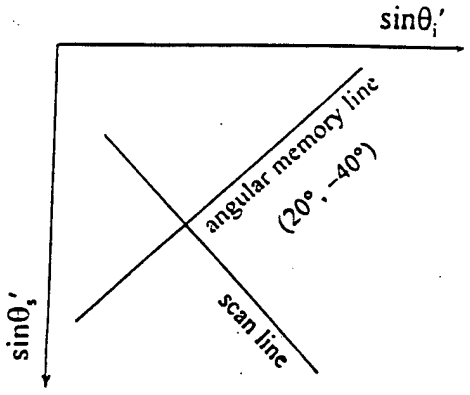

Fig. 2 The angular memory line and the scan line

We have conducted wideband millimeter-wave experiments to evaluate the effectiveness of this correlation technique for the detection of a target in a homogeneous medium. At 75–110 GHz, a long conducting cylinder (diameter ≈ 1λ) was buried at a depth of about 1λ below a homogeneous medium formed by very fine sand particles with a flat sand-air interface. The size of the sand particles was chosen so that the dominance of surface scattering over volume scattering can be justifiably assumed. An ACF measurement based on one single spatial sample was then made along the scan line. Experimental results with and without a buried target will be presented.

[1] *Radar Handbook*, 2nd Ed, Edited by M. Skolnik, McGraw-Hill, 1990.
[2] *Ultrawideband Radar*, Proceedings SPIE, Vol. 1631, Los Angeles, Jan. 1992.
[3] *Radar Polarimetry for Geoscience Applications*, edited by F. Ulaby and C. Elachi, Artech House, 1990.
[4] I. Freund, M. Rosenbluh, and S. Feng, "Memory effects in propagation of optical waves through disordered media," *Phys. Rev. Letters*, **61**, No. 20, 1988.
[5] T. R. Michel and K. A. O'Donnell, "Angular correlation functions of amplitudes scattered from a one-dimensionally, perfectly conducting rough surface," *J. Opt. Soc. Am.*, **9**, No. 8, 1992.
[6] M. Nieto-Vesperinas and J. A. Sánchez-Gil, "Intensity angular correlations of light multiply scattered from random rough surfaces," *J. Opt. Soc. Am.*, **10**, No. 1, 1993.
[7] C. Le, Y. Kuga and A. Ishimaru, "Angular correlation function based on the second-order Kirchhoff approximation and comparison with experiments," *Journal of the Optical Society of America A*, to appear May, 1996.
[8] Y. Kuga and C. Le, A. Ishimaru, and L. Ailes-Sengers, "Analytical, experimental and numerical studies of angular memory signatures of waves scattered from one-dimensional rough surfaces," accepted by *IEEE Trans. Geoscience and Remote Sensing*, 1996.
[9] Y. Kuga, T. Chan, and A. Ishimaru, "Detection of a target embedded in clutter using the angular memory effect," submitted to *IEEE Trans. Antennas and Propagation*, 1995.
[10] Guifu Zhang, Leung Tsang, and Yasuo Kuga, " Studies of the Angular Correlation Function of Scattering by Random Rough Surfaces With and Without a Buried Object," submitted to *IEEE Trans. Geoscience and Remote Sensing*, 1996.

SPECKLE CORRELATIONS AND INVERSE SCATTERING METHODS FOR 1-d AND 2-d RANDOMLY ROUGH METAL SURFACES

Arthur R. McGurn, Vladislav Malyshkin and Simeon Simeonov
Department of Physics
Western Michigan University
Kalamazoo, Michigan 49008 U.S.A.

Alexei A. Maradudin
Department of Physics and Astronomy
Institute for Surface and Interface Science
University of California
Irvine, California 92717 U.S.A.

Two calculations are presented:

1) A perturbation theory study is made of the angular and frequency correlations which exist in the speckle pattern of light scattered from 1-d and 2-d weakly rough, random metal surfaces.

2) The surface profile and the power spectrum of the surface roughness are extracted from scattering data for weakly rough, random metal surfaces using Reverse Monte Carlo methods[1] and perturbation theory results for the differential reflection coefficient of such surfaces.

In both calculations we consider weakly rough Gaussian random surfaces described by surface profile functions $\{\varsigma(x_1)\}$ in 1-d and $\{\varsigma(x_1, x_2)\}$ in 2-d. The surfaces are planar on average with $x_3 > \varsigma(x_1)$ or $\varsigma(x_1, x_2)$ being a vacuum and $x_3 < \varsigma(x_1)$ or $\varsigma(x_1, x_2)$ being a region of metal with dielectric constant $\epsilon = \epsilon_1 + i\,\epsilon_2$ where $\epsilon_1 < -1$. (For the specific results we present we have considered silver and gold surfaces illuminated by light of wavelength 4579 Å and 6120 Å, respectively.) In studies of the 1-d rough surfaces we use the perturbation theory approach developed for such surface by McGurn, Maradudin and Celli.[2] In studies of 2-d rough surfaces we use the perturbation theory approach developed for such surfaces by McGurn and Maradudin.[3] Both of these approaches are ultimately based on a general theory of rough surface scattering formulated by Brown et al.[4]

In the speckle correlation calculations, 1) above, we compute the correlation function

$$C(q,q',k,k') = \left\langle \left(I(q|k) - \left\langle I(q|k) \right\rangle \right) \left(I(q'|k') - \left\langle I(q|k) \right\rangle \right) \right\rangle$$
$$= 16\,\alpha_0(q)\,\alpha_0(q')\,\alpha_0(k)\,\alpha_0(k') \left\langle \left(|G(q|k)|^2 - \left\langle |G(q|k)|^2 \right\rangle \right) \left(|G(q'|k')|^2 - \left\langle |G(q'|k')|^2 \right\rangle \right) \right\rangle$$

where $\langle\,\rangle$ represents an average over surface profile functions; q, q′, k, k′ are the wavevector components of light which are parallel to the mean surface; $I(q|k)$ is the intensity of light scattered

with q for light of incident unit intenisty with k; $\alpha_0(r) = \left[\left(\frac{\omega}{c}\right)^2 - r^2\right]^{\frac{1}{2}}$; and $G(q|k)$ is the Green's function for the propagation of surface polaritons along the random surface. The function C(q, q′, k, k′) gives the correlation between light incident with k scattered into q and light incident with k′ scattered into q′. If the light in each of these two scattering is of different frequency then C(q, q′, k, k′) also describes the frequency correlation.

The correlation function C(q, q′, k, k′) can be represented as a sum of four parts $C^{(1)}$, $C^{(2)}$, $C^{(3)}$ and $C^{(R)}$. $C^{(1)}$ is a "memory effect" part which vanishes unless $q - k = q' - k'$. $C^{(2)}$ is a long range component which is non-zero for general q, k, q′ and k′, but goes to zero as $q - q' \to \infty$ and/or $k - k' \to \infty$. $C^{(3)}$ is an infinite range component which is non-zero for general q, k, q′ and k′, but is relatively independent of $q - q'$ and $k - k'$. $C^{(R)}$ are some remaining terms which are found to be important in surface scattering, and contain new features in C arising from resonant scattering processes involving surface polaritons. This last effect is specific for C from surface scattering. Results for $C^{(1)}$, $C^{(2)}$, $C^{(3)}$ and $C^{(R)}$ are presented for 1-d p to p scattering and 2-d p to p, p to s, s to p and s to s scattering.

In computing $C^{(1)}$, $C^{(2)}$, $C^{(3)}$ and $C^{(R)}$ a diagrammatic approach is used involving sums of ladder diagrams which in the absence of dissipative losses ($\epsilon_2 = 0$) reduce to diffusion poles and sums of maximally crossed diagrams which give rise to time-reversed phase coherent effects. A number of sharp peaks are found in $C^{(1)}$, $C^{(2)}$ and $C^{(R)}$ studied as functions of q and q′ for fixed k and k′. These peaks are correlated with various phase coherent time-reverse processes, multi-photon processes involving surface polariton and memory effects. The width of the peaks in $C^{(1)}$, $C^{(2)}$ and $C^{(R)}$ are found to be directly related to the decay length for the propagation of surface polaritons along the random vacuum-metal interface.

C(q, q′, k, k′) is computed for two types of surface. The first type is a Gaussian random surface with

$$\left\langle \varsigma(x_1)\, \varsigma(x_1') \right\rangle = \delta^2 \exp\left[-|x_1 - x_1'|^2/a^2\right]$$

in 1-d and

$$\left\langle \varsigma(x_1,x_2)\, \varsigma(x_1',x_2') \right\rangle = \delta^2 \exp\left[-\frac{(x_1-x_1')^2 + (x_2-x_2')^2}{a^2}\right]$$

in 2-d.

The second type involves a Gaussian random surface with the West and O'Donnell[5] step function form in 1-d and its generalization in 2-d.

In Fig. (1) a sampling of results are shown for C(q, q′, k, k′) computed for a 2-d rough Ag surface.

FIG. 1

Correlation Function Results for 2-D p to p Scattering

Results for Gaussian random surface with $\sigma^2 g(\vec{k}) = \pi \sigma^2 a^2 \exp[-(ka)^2/4]$ for Ag surface with $\sigma = 40$ Å, $a = 1000$ Å, $\lambda = 4579$ Å, $\epsilon = -7.5 + i\,0.25$. Figures are shown for incident k, k′ to scattered q, q′ components parallel to the mean surface where $k = \frac{\omega}{c} \sin\theta_k$ with angle θ_k measured from the normal to the surface for; a) C1 for $\theta_k = 20°$, $\theta_{k'} = -10°$; b) C2, C3 and CR for $\theta_k = 20°$, $\theta_{k'} = -10°$ and $\theta_q = 30°$.

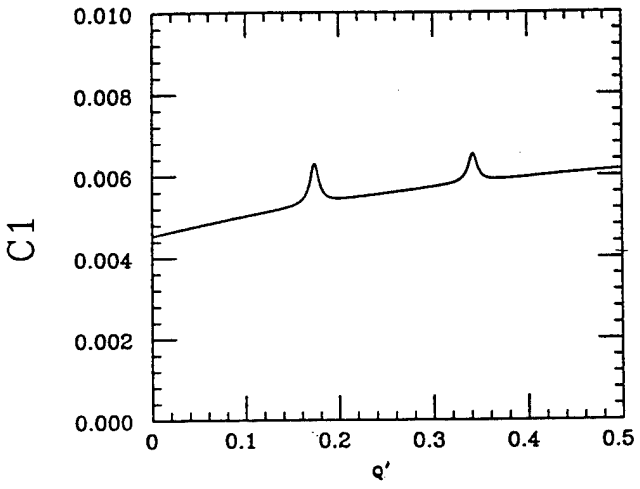

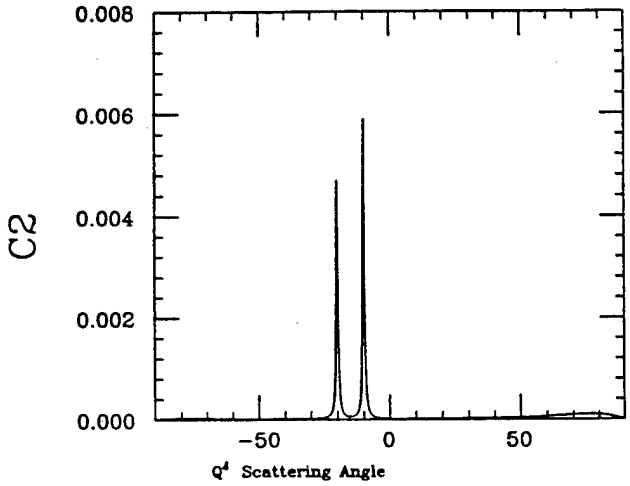

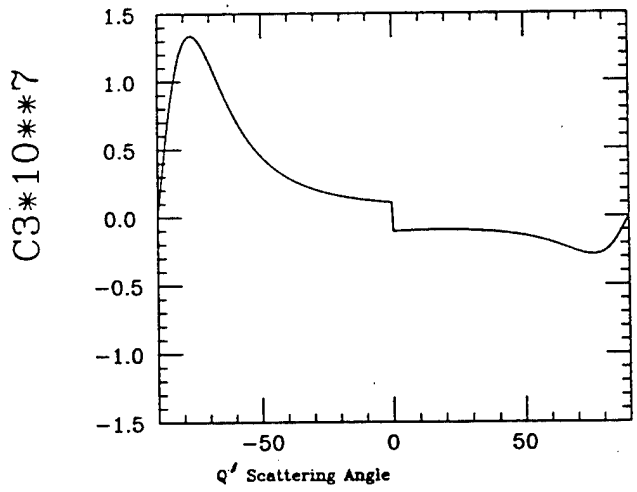

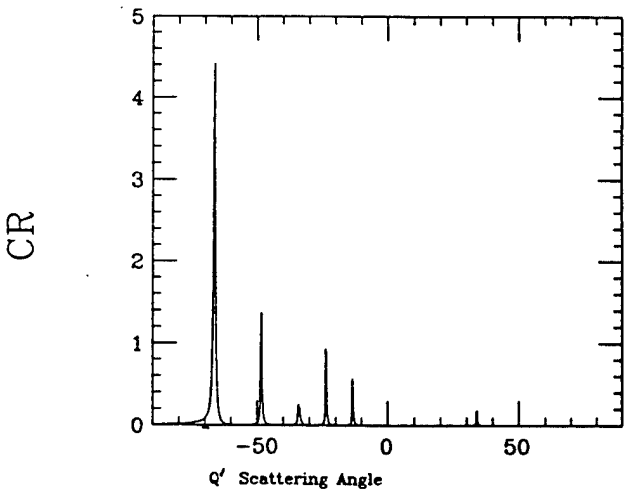

In the surface profile calculations, 2) above, data for the mean differential reflection coefficient of light scattered by a weakly rough metal surface is used to extract the power spectrum of the surface profile. Data for the differential reflection coefficient of light scattered by a ridge or groove on a metal surface is, also, used to extract the shape of the ridge or groove.

Specifically, the surface profile or spectral density is extracted from experimental data using Reverse Monte Carlo methods based on perturbation theory results. In this method we start with a flat surface. A random weak perturbation is given to the flat surface and the differential reflection coefficient for the resulting surface is computed using perturbation theory. A χ-square comparison is made between the scattering data and the differential reflection coefficient computed above. A sampling criterion based on Maximum Entropy methods is applied to the χ-square results to accept or reject the random profile as a description of the surface. If the random profile is rejected, we return to the original surface before the random change and repeat the above procedure. If the random profile is accepted, then a random change is made in the accepted surface profile and the scattering results from the new profile are subjected to the χ-square comparison. This procedure is repeated until the computed differential reflection coefficient agrees with the scattering data and the surface profile has been extracted.

This type of Reverse Monte Carlo procedure has been developed only recently to extract the structures of amorphous and polymer materials, and has been found to be very effective when applied to the determination of such structures. Our work is a first application of these techniques to the study of rough surface geometry.

Results for the extracted power spectra and profiles are presented for a number of different types of surfaces, including some recent experimental systems studied by West and O'Donnell.[5] An attempt is made to determine the minimum amount of scattering data need and the conditions on the scattering data (i.e., optimum angles of incidence, number of different frequencies need) needed for the accurate extraction of surface profile information. In general it is found that quite reasonable reproductions of the surface profile can be obtained using data for just two incident angles of light.

In Fig. (2) a sample of a power spectrum extracted from scattering data of West and O'Donnell[5] by the RMC is compared with surface profilometry results of West and O'Donnell for the same surface. Excellent agreement between the two power spectra is observed.

References

1) R.L. McGreery and M.A. Howe, Annu. Rev. Mater. Sci. 22, 217 (1992).
2) A.R. McGurn, A.A. Maradudin and V. Celli, Phys. Rev. B31, 4866 (1985).
3) A.R. McGurn and A.A. Maradudin, in press.
4) G. Brown, V. Celli, M. Haller, A.A. Maradudin and A. Marvin, Phys. Rev. B31, 4993 (1985).
5) C.S. West and K.A. O'Donnell, J. Opt. Soc. Am. A12, 390 (1995).

Reverse Monte Carlo Results

The power spectrum measured by West and O'Donnell (Experiment) compared to the RMC extraction from the differential reflection coefficient data of West and O'Donnell (Theory).

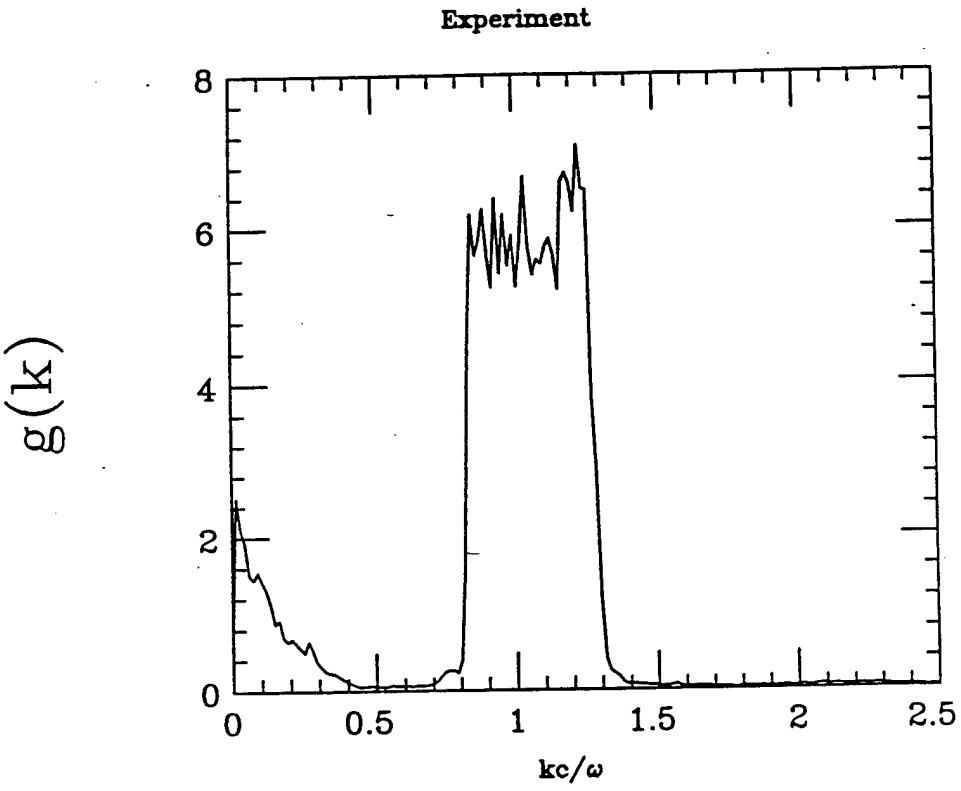

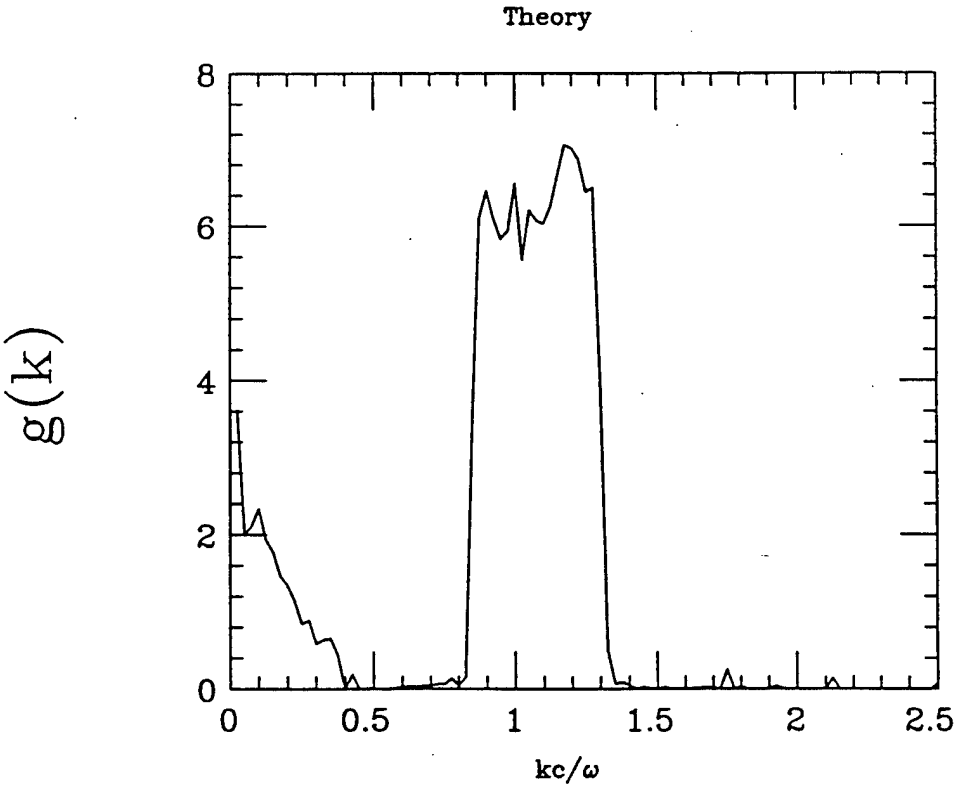

The inverse scattering problem for rough surfaces from both deterministic and statistical points of view

D. Maystre
Laboratoire d'Optique Electromagnétique
Faculté des Sciences et Techniques de Saint Jérôme (case 262)
Avenue Escadrille Normandie-Niemen
F 13397 Marseille, Cedex 20, France

Due to the tremendious development of real time control and quality tests for manufactured parts, the characterization of metallic, dielectric and semiconductor surfaces is becoming increasingly important [1]. Classical optical methods such as optical microscope, light sectionning [2], optical profilometer [3,4] or optical interferometers like FECO [5] or TOPO (WYCO Corporation) provide valuable tools but they can require a long processing time and, above all, they are not adapted to the resonance domain. The same drawbacks hold for near field optical microscopes [6,7]. Surface characterization based on scattered light analysis allows a rapid, non destructive, real time control or inspection of surface microtopography [8]. It needs a prior precise solving of the scattering problem, which can make problem in some complex cases (surfaces coated by numerous dielectric films, 3D problems), at least if the perturbation theory or the Kirchhoff approximation fail.

The aim of the communication is to show some results obtained in the last 20 years in characterization of surfaces from scattered field analysis in the optical domain. These techniques differ from the classical optical means by the fact that scattering is not prejudicial to the quality of the characterization but is, on the other hand, the basic element of the characterization process.

The easiest kind of problem to be solved is classified as parameter adjustment. In that case, one has to determine the value of a few parameters. Some examples will be given. For deterministic surfaces, the determination of the two parameters of a V-shaped groove scribed in a brass plate, has been achieved at the National Institute of Standards and Technology (Gaithersburg, USA). The measurement of the scattering pattern was made using a piezoelectric detector rotating at a constant radius in the plane normal to the groove, from -90° to +80°[9] and the theoretical scattering patterns were obtained from a rigorous theory [10]. A similar achievement has been made in the field of gratings with the determination of the groove depth of sinusoidal holographic aluminum gratings with 1200 or 1800 grooves/mm, using a 0.6328 mm He-Ar and a 0.4579 mm argon ion lasers,

and a Spectra-Physics Model 404 laser power meter to measure the efficiency of the grating in Littrow mount [11]. The experimental data was compared with results from a rigorous theory of diffraction gratings [12]. In a problem linked with the technology of CMOS in microelectronics, the process of oxide reflow of glass in an oven was controlled by printing in a corner of the sample a small grating, the efficiency of which was measured in real time during the process [13]. L.R. Baker proposed a vary peculiar method for measuring the height of a step made in a dielectric or metallic plane [14]: the scattering pattern of the step to be characterized was compared with that generated by a set of steps of known heights. For randomly rough surfaces, the determination of the rms can be achieved from a measurement of the total integrated scatter [15, 16].

The inverse scattering problem, where the unknown is a function, is much more difficult to solve since, in addition to the solving of the direct scattering problem, one must face a dramatic mathematical and numerical difficulty: the inverse problem is ill-posed in the sense of Hadamard. Fortunately, the cleaver solution proposed by Tikhonov and classified as "regularization of ill-posed problems" can provide a very accurate tool for the solution of inverse problems. A Newton-Kantorovitch algorithm with Tikhonov regularization [17] has been used for the determination of the (non sinusoidal) shape of holographic gratings from experimental measurements of efficiency [18]. The same kind of formalism can be used for the determination of the permittivity of a stack of dielectric layers from measurements of the reflection factor [19] The very difficult problem of the calculation of the power spectrum of a non-shallow randomly rough surface will also be presented and analyzed from numerical results.

References

[1] E.C. Teague, T.V. Vorburger and D. Maystre, Light scattering from manufactured surfaces, CIRP, 30, 1981, 1-7.

[2] G. Schmaltz, in Technische Oberflaechankunde, Springer, Berlin, 1936.

[3] C. Gorecki, G. Tribillon and J. Mignot, J. Optics,14, 1983.

[4] J.C. Quartel and C.J.R. Sheppard, Journal of Modern Optics, 43,1996,469-486.

[5] H. Bennett and J. Bennett, in Physics of Thin Films (G. Haas, ed.), Academic Press, New York, 1967.

[6] C. Girard and M. Spager, Applied Optics, 29,1990.

[7] C. Baignier, D. Courjon, F. Baida and C. Girard, J. Opt. Soc. Am. A, 13,1996, 287.

[8] D. Maystre, Light scattering by solid surfaces and surface characterization, in Light scattering by liquid surfaces and complementary techniques, Ed. D. Langevin, Marcel Dekker, 1992.

[9] G.S. White and J.F. Marchiando, Applied Optics, 22, 1983, 2308-2312.

[10] D. Maystre, IEEE Trans. Antennas Prop., 31, 1983, 885-895.

[11] I.J. Wilson and L.C. Botten, Applied Optics, 16, 1977, 2086-2089.

[12] D. Maystre, Optics commun., 6, 1972.

[13] A. Tissier, A. Poncet, G. Giroult, D. Maystre and P. Vincent, In-process optical measurements, Ed.K.H. Spring, Vol. 1012, chap. 3, 1988.

[14] L. R. Baker, Optica Acta, 31, 1984, 611-614.

[15] J.M. Bennett and J.H. Dancy, Applied Optics, 20, 1981, 1785.

[16] L. Mattson, Thin films Technology, Ed. J.R. Jacobson, Proc. SPIE, 652,1986, 264.

[17] A. Roger, D. Maystre, M. Cadilhac, J. Optics, 9, 1978, 83-90.

[18] A. Roger and M. Breidne, Optics Commun., 35, 1980, 299-302.

[19] A. Sammar and J.M. André, Journal of Modern Optics, 43, 1996, 67-79.

Angular, Frequency, Time and Polarization Correlations of Waves Scattered by Rough Surfaces and Applications to Surface Profile Determination and Object Detection

Akira Ishimaru, Yasuo Kuga, Charlie T. C. Le, and Tsz-King Chan
Department of Electrical Engineering
University of Washington
Box 352500
Seattle, Washington 98195-2500
Tel: 206-543-2169, Fax: 206-543-3842, E-mail: ishimaru@ee.washington.edu

This paper presents our recent study on the correlation effects of waves scattered by rough surfaces. The angular correlation, called the "memory effect," has been studied extensively in the past. The memory effect is applied to the determination of the average height profile of rough surfaces. This is the topographic mapping problem addressed by InSAR, and therefore, our approach is a generalization of conventional InSAR to include four antenna elements. The theory is based on the Kirchhoff approximation applied to surfaces with large radii of curvature. Unlike conventional scattering cross sections per unit area of the rough surface, we consider two incident waves at different incident angles and the corresponding scattered waves at two different directions. The correlation function of these two scattered waves, called the mutual coherence function, is then calculated. The surface consists of the slowly varying deterministic average profile and the randomly varying height. It is shown that the phase of the mutual coherence function is directly related to the average surface profile, and therefore, the topographic map of the height profile can be determined by the measurement of the mutual coherence function. The relative positions of the four antennas affect the sensitivities of the determination of the height profile, and this is studied by examining the memory signature diagram which shows the amplitude and phase of the mutual coherence function as functions of the incident and scattering angles [1]-[10].

The memory signature diagram is constructed as follows. Let the incident field with the incident angle θ_i be E_i and the corresponding scattered field in the direction θ_s be E_s. Also let E_i' be the incident wave at θ_i' and E_s' be the scattered wave at θ_s'. We plot the correlation $B(x,y) = < E_s E_s'^{*} >$ as a function of $x = \sin\theta_i'$ and $y = \sin\theta_s'$. Then the correlation B is strong along the memory line $y - y_o = x - x_o$ where $y_o = \sin\theta_s$ and $x_o = \sin\theta_i$ as expected from the memory effect. Outside of this line, B is small. However, for a deterministic object, the correlation is not small in all x and y. Therefore, the memory effect can be used to detect an object buried in random media. It is shown that the memory effects are drastically different depending on whether the medium is deterministic or random. This difference can be effectively used to separate the object and the surrounding random medium. Millimeter wave experiments are conducted to show that a conducting cylinder buried in a random medium can be detected using this technique [7].

The angular correlation is also extended to include the frequency correlation using the two-frequency mutual coherence function. The Fourier transform of the two-frequency mutual coherence function gives the pulse response. We can now let E_i and E_s be the incident and scattered fields at $k = \omega/c$ and E_i' and E_s' be the field at

$k' = \omega'/c$. Then the memory line is now extended to $k(\sin\theta_s - \sin\theta_i) = k'(\sin\theta_s' - \sin\theta_i')$.

The inverse double Fourier transform of the two-frequency mutual coherence function $\Gamma(\omega_1, \omega_2)$ gives the correlation in time difference *td*, $\Gamma(t_c, t_d)$, and $\Gamma(t_c, t_d = 0)$ is the pulse shape. The two-frequency mutual coherence function for very rough surfaces has been studied in detail, and the analytical results are compared with numerical Monte Carlo and experimental results. It is also shown that if the surface consists of a slowly varying profile and rough surfaces, the pulse arrival time is related to the surface height profile [10].

If the polarization state of the incident wave changes, the polarization of the corresponding scattered wave changes. Polarization responses or signatures are one useful example of this polarization correlation. We have generalized this idea to include two different polarization states for incident waves and two different observed polarization states for scattered waves. The polarization response diagram is then generalized to show the characteristic signatures for deterministic and random media.

Let χ_i and ψ_i be the ellipticity and orientation angles of the incident wave E_i, and let χ_i' and ψ_i' be those of E_i'. We also let χ_s and ψ_s be the angles for E_s, and χ_s' and ψ_s' be those of E_s'. Then it is possible to examine the relationships between the backscattered fields and the incident fields. Note that if $\chi_i = \chi_i' = \chi_s = \chi_s'$ and $\psi_i = \psi_i' = \psi_s = \psi_s'$, then this relationship can be expressed by the conventional polarization signature, and therefore the above studies are its generalization. This generalized signature is studied for several special cases. For example, if $\chi = 0$, the Fourier transforms of the correlation in ψ_s' and ψ_i' show peaks at different wave numbers depending on the nature of the object and whether the scattering is single or multiple. Numerical studies for different objects and rough surfaces are conducted and further studies are continuing.

References:

[1] A. Ishimaru, C. T. C. Le, Y. Kuga, L. Ailes-Sengers, and T.-K. Chan, "Polarimetric scattering theory for high slope rough surfaces," in *Progress in Electromagnetics Research*, edited by M. Tateiba and L. Tsang, to be published 1966.

[2] P. Phu, A. Ishimaru, and Y. Kuga, "Controlled millimeter-wave experiments and numerical simulations on the enhanced backscattering from one-dimensional very rough surfaces," Radio Science, vol. 28, no. 4, pp. 533-548, July-August 1993.

[3] A. Ishimaru, J. S. Chen, P. Phu, and K. Yoshitomi, "Numerical, analytical, and experimental studies of scattering from very rough surfaces and backscattering enhancement," Waves in Random Media, vol. 1, no. 3, pp. 91-107, July 1991.

[4] V. Celli, A. A. Maradudin, A. M. Marvin, and A. R. McGurn, "Some aspects of light scattering from a randomly rough metal surface," J. Opt. Soc. Am. A, vol. 2, pp. 2225-2239, 1985.

[5] S. Feng, C. Kane, P. A. Lee, and A. D. Stone, "Correlations and fluctuations of coherent wave transmission through disordered media," Phys. Rev. Lett., vol. 61, pp. 834-837, 1988.

[6] M. Nieto-Vesperinas and J. A. Sanchez-Gill, "Intensity angular correlations of light multiply scattered from random rough surfaces," J. Opt. Soc. Am. A, vol. 10, pp. 150-157, 1993.

[7] Y. Kuga, T.-K. Chan, and A. Ishimaru, "Detection of a target embedded in clutter using the angular memory effect," submitted to the IEEE Transactions on Antennas and Propagation, 1995.

[8] Y. Kuga, C. T. C. Le, A. Ishimaru, and L. Ailes-Sengers, "Analytical, experimental, and numerical studies of angular memory signatures of waves scattered from one-dimensional rough surfaces," accepted by the IEEE Transactions on Geoscience and Remote Sensing, 1996.

[9] A. Ishimaru, L. Ailes-Sengers, P. Phu, and D. Winebrenner, "Pulse broadening of enhanced backscattering from rough surfaces," Waves in Random Media, vol. 4, no. 4, pp. 453-465, October 1994.

[10] A. Ishimaru, C. T. C. Le, Y. Kuga, J.-H. Yea, and K. Pak, "Angular memory interferometric technique for retrieving the mean height profile of rough surfaces," submitted to the IEEE Transactions on Geoscience and Remote Sensing, 1996.

Angular Correlation Function of Speckle Patterns Scattered from a One-dimensional Rough Dielectric Film on a Glass Substrate

Jun Q. Lu and Zu-Han Gu
Surface Optics Corporation, P.O. Box 261602, San Diego, CA 92196

ABSTRACT

Currently, the scattering of light from random rough surfaces has gained much attention. By now much work has been focused on the enhanced backscattering phenomenon, which is manifested as a well-defined peak in the retroreflection direction in the angular distribution of the scattering light. It has been attributed to the correlations between the scattered field and its time-reversed counterpart.

When a coherent light is reflected from a rough surface, a complex speckle pattern is formed. This is the result of the interference among the scattered wavelets, each arising from a different microscopic element of the rough surface. However, recent theoretic study in volume scattering shows [1–4] that there are novel correlations among the speckle patterns in the multiple scattering regime and they can be divided into three types: short-range correlation, long-range correlation, and infinite-range correlations. These three types of correlations play different roles in different scattering system geometries. The short-range correlation, also known as memory effect, is the dominant part in system where the dimension in the direction of the light propagation is much smaller than that in the direction perpendicular to it. The memory effect dictates that even though a laser wave suffers many scattering events upon traversing a thick volume scattering sample, and therefore its wavefront is much distorted and seemingly random, it still "remembers" the wavefront of the incoming plane wave, so that as the incoming beam direction changes slightly, the transmitted or reflected speckle pattern will move accordingly. The long-range and infinite-range correlations will be the dominate part in the system where the dimension in the direction of the light propagation is larger than that in the direction perpendicular to it. These phenomena have then be confirmed theoretically and experimentally for volume scattering.

Correlation in light scattering from random rough surfaces has been studied .[5–10] Taking into account of the multiple-scattering, the intensity correlation function for light elastically scattered from a randomly rough metallic grating was calculated ,[5] and the angular intensity correlation of light scattering in double-passage through a random phase screen was investigated .[7] In recent theoretical and experimental investigations the correspondence between the correlation function and the enhanced backscattering

peak has been studied for light scattering from randomly rough metallic surfaces producing multiple scattering .[9-10]

In this paper we will study the angular correlation between the scattered speckle patterns generated by light incident to a rough dielectric film on a glass at different angles of incidence. Experimental results are presented for the angular correlation function of far field speckle patterns scattered by a one-dimensionally random rough surface of a thin dielectric film on a glass substrate when a polarized beam of light is incident on the rough surface from vacuum. This surface, which separates the vacuum and the dielectric, is rough enough so that only the diffused speckles are observed. The experiment for the correlation measurement was set up to use a CCD camera to obtain the image of the speckle pattern in the specular direction for each given angle of incidence, the cross correlation function is then calculated from the digitized images. It is found that the intensity correlation functions exhibit two distinct maxima, one arises from the autocorrelation and the other from the reciprocity condition. It is also found that different scattering processes give rise to quite different correlation functions, where multiple-scattering processes produce narrow peaks with secondary maxima, while single-scattering processes produce relatively broader peaks.

REFERENCES

(1) S. Feng, C. Kane, P. A. Lee, and A. D. Stone, "Correlations and fluctuations of coherent wave propagation through disordered media", Phys. Rev. Lett., 834 (1988).

(2) I. Freund, M. Rosenbluh, and S. Feng, " Memory effect in propagation of optical waves through disordered media", Phys. Rev. Lett., 2328 (1988).

(3) R. Berkovits, M.Kaveh, and S. Feng, " Memory effect of waves in disordered systems: a real space approach", Phys. Rev., 737 (1989).

(4) L. Wang and S. Feng, "Correlations and fluctuations in reflection coefficients for coherent wave propagation in disordered scattering media", Phys. Rev., 8283 (1989).

(5) A. R. McGurn and A. A. Maradudin, "Intensity correlation function for light elastically scattered from a randomly rough metallic grating", Phys. Rev., 13160 (1989).

(6) M. Nieto-Vesperinas, J. A. S´anchez-Gil, "Intensity angular correlations of light multiplely scattered from random rough surfaces", J. Opt. Soc. Am. A-10, 150 (1993)

(7) H. Escamilla, E. Mendez, and D. Hots, "Angular intensity correlation in the double passage for waves through a random phase screen", Applied Optics, Vol. 32, No. 15, 2734-2743 (1993).

(8) T. R. Michel and K. A. O'Donnell, "Angular correlation functions of amplitudes scattered from a one-dimensional, perfectly conducting rough surface", J. Opt. Soc. Am., 1374 (1992).

(9) M. E. Knotts, T. R. Michel, and K. A. O'Donnell, "Angular correlation functions of polarized intensities scattered from a one-dimensionally rough surface", J. Opt. Soc. Am., (1992).

(10) A. Arsenieva and S. Feng, "Correspondence between correlation functions and enhanced backscattering peak for scattering form smooth random surfaces", Phys. Rev. B, (1994).

Multiple Scattering Effects in the Second Harmonic Generation of Light in Reflection from a Randomly Rough Metal Surface

M. Leyva-Lucero* and E. R. Méndez

División de Física Aplicada, Centro de Investigación Científica y de Educación Superior de Ensenada, Apartado Postal 2732, Ensenada, Baja California, 22800 México

T. A. Leskova

Institute of Spectroscopy, Russian Academy of Sciences, Troitsk 142092, Russia

A. A. Maradudin

Department of Physics and Astronomy, and Institute for Surface and Interface Science, University of California, Irvine, California, 92717

Jun Q. Lu

Department of Physics, East Carolina University, Greenville, NC 27858, U.S.A.

Abstract

We present a rigorous numerical simulation analysis of the second harmonic generation of $p-$polarized light in reflection from a one-dimensional, randomly rough, metal surface, when the plane of incidence is perpendicular to the generators of the surface. When the incident light can couple to surface electromagnetic waves supported by the metal surface at the harmonic frequency, the angular distribution of the intensity of the incoherent component of the scattered light at the harmonic frequency displays either well-defined peaks or dips in the retroreflection direction and in the direction normal to the mean plane of the surface. These effects are suppressed by the direct excitation of surface electromagnetic waves at the fundamental frequency.

Interference effects in the multiple scattering of electromagnetic waves in disordered media or from rough surfaces have attracted much attention recently in view of their analogy with the interference effects occurring in the multiple scattering of electrons in strongly disordered media that are responsible for Anderson localization. Even if the disorder is weak, these effects are important since they can lead to weak localization - enhanced backscattering - viz. a peak in the retroreflection direction in the angular distribution of the intensity of the light scattered diffusely from disordered media. The enhanced backscattering of light from weakly rough metal surfaces has been of special interest because the multiple scattering of the surface electromagnetic waves supported by such surfaces - surface plasmon polaritons - is responsible for the appearance of the enhanced backscattering peak [1].

Recently, the main ideas of weak localization have been applied to nonlinear optical phenomena in disordered media (see, e.g. [2]). In particular, the results of a perturbative calculation predict that enhanced second harmonic generation of light at a weakly rough metal surface occurs not only in the retroreflection direction but also in the direction normal to the mean surface [3]. The multiple scattering of surface polaritons plays the decisive role in the appearance of both peaks.

Perturbation theory for rough surface scattering, however, has a limited range of applicability [4], and inevitably involves other approximations as well (e. g. small roughness approximation [5], pole approximation, Rayleigh hypothesis). In this Letter we describe rigorous numerical calculations of the second harmonic generation of light in reflection from a one-dimensional, weakly rough, random metal surface. The numerical approach we have used follows closely that described in detail in [6].

The physical system we consider consists of an isotropic metal characterized by a complex, frequency dependent dielectric constant $\epsilon(\omega)$ in the region $x_3 < \zeta(x_1)$ and vacuum in the region $x_3 > \zeta(x_1)$. The surface profile function $\zeta(x_1)$ is assumed to be a single-valued function of x_1 that constitutes a stationary, zero-mean, Gaussian random process.

A $p-$polarized Gaussian beam of frequency ω [6] is incident from the vacuum side at an angle θ_0 onto a surface of length L with the plane of incidence the x_1x_3-plane.

The source functions, defined as $H(x_1 \mid \Omega) = H_2^>(x_1, x_3 \mid \Omega)|_{x_3=\zeta(x_1)}$ and $L(x_1 \mid \Omega) = \phi(x_1)\,(\partial H_2^>(x_1, x_3 \mid \Omega)/\partial n)\,|_{x_3=\zeta(x_1)}$, where Ω stands for either ω or 2ω, $H_2^>(x_1, x_3|\Omega)$ is the total magnetic field in the vacuum region, $\phi(x_1) = \{1 + [\zeta'(x_1)]^2\}^{1/2}$, and $\partial/\partial n$ denotes the derivative along the normal to the surface directed from the metal into the vacuum, satisfy a pair of inhomogeneous integral equations at both frequencies ω and 2ω. The integral equations at the frequency ω obtained in a manner described in [6] are converted into matrix equations and solved using standard numerical techniques.

To calculate the second harmonic (SH) field we make use of the fact that homogeneous and isotropic metals possess inversion symmetry. Then, the SH radiation we are interested in is generated in a metal-vacuum interface layer across which both material constants and electromagnetic fields vary strongly and which has a finite thickness on the microscopic scale. Integrating Maxwell's equations across the interface layer with the use of the phenomenological expression for the surface nonlinear polarization given in [7], we obtain the nonlinear boundary conditions at a rough metal surface in the form

$$L(x_1|2\omega) - \frac{L^<(x_1|2\omega)}{\epsilon(2\omega)} = \frac{2ic}{\omega}\frac{d}{dx_1}\left\{\mu_1(\omega)\left(\phi(x_1)\frac{d}{dx_1}H(x_1|\omega)\right)^2 + \mu_2(\omega)\left(\phi(x_1)L(x_1|\omega)\right)^2\right\}, \tag{1}$$

and

$$H(x_1|2\omega) - H^<(x_1|2\omega) = -\frac{2ic}{\omega}\mu_3(\omega)\phi^2(x_1)L(x_1|\omega)\frac{d}{dx_1}H(x_1|\omega)\,, \tag{2}$$

where $H^<(x_1 \mid 2\omega)$ and $L^<(x_1 \mid 2\omega)$ are the source functions inside the metal at the harmonic frequency and are obtained from $H(x_1|2\omega)$ and $L(x_1|2\omega)$ with the appropriate changes. The phenomenological constants $\mu_1(\omega)$, $\mu_2(\omega)$, and $\mu_3(\omega)$ appearing in Eqs. (1) and (2) characterize the behavior of the nonlinearity coefficients and the dielectric constants in the interface layer [3,7].

With the use of the nonlinear boundary conditions we obtain a pair of inhomogeneous integral equations for the source functions $H(x_1|2\omega)$ and $L(x_1|2\omega)$ which can be solved numerically, once we have calculated the fundamental field source functions and, consequently,

the nonlinear sources in Eqs. (1) and (2). The differential reflection coefficient (drc), which gives the fraction of the total energy incident onto the surface that is converted into fundamental or harmonic light scattered into an angular interval $d\theta_s$ around the scattering direction θ_s can now be determined in a standard manner [6].

The results presented below represent averages obtained from 2000 realizations of the random surface. The wavelength of the incident light was chosen to be $1.064\mu m$. The dielectric constants of silver at the fundamental and harmonic frequencies are then $\epsilon(\omega) = -56.25 + i0.60$ and $\epsilon(2\omega) = -11.56 + i0.37$, respectively. In all our calculations we have used values of the nonlinear parameters $\mu_1(\omega)$, $\mu_2(\omega)$, and $\mu_3(\omega)$ given by the free-electron model [8].

The surfaces we consider here are weakly rough. Therefore, as was done recently to enhance interference effects involving surface polaritons in the incoherent scattering of light from weakly rough one-dimensional metal surfaces [9], and to clarify the mechanisms responsible for the appearance of different features in the drc at frequency 2ω, we have carried out calculations for random surfaces characterized by power spectra that are nonzero only in the ranges of wavenumbers in which the incident light can couple into surface polaritons at frequencies ω and/or 2ω:

$$g(|k|) = \frac{\pi H_1}{\Delta k(\omega)}\left[rect\left(\frac{k-k_{sp}(\omega)}{\Delta k(\omega)}\right) + rect\left(\frac{k+k_{sp}(\omega)}{\Delta k(\omega)}\right)\right] + \\ + \frac{\pi H_2}{\Delta k(2\omega)}\left[rect\left(\frac{k-k_{sp}(2\omega)}{\Delta k(2\omega)}\right) + rect\left(\frac{k+k_{sp}(2\omega)}{\Delta k(2\omega)}\right)\right], \quad (3)$$

where $k_{sp}(\Omega) = (\Omega/c)Re[\epsilon(\Omega)/(\epsilon(\Omega)+1)]^{1/2}$, $H_1 + H_2 = 1$, $\Delta k(\Omega) = 2(\Omega/c)\sin\theta_m$, and *rect* represents the rectangle function [11]. For the examples presented here we have chosen $\theta_m = 20°$.

In Fig. 1 we present the contribution to the mean drc from the incoherent component of light scattered at frequency 2ω, when the surface is characterized by the power spectrum (3) with $H_1 = 0$, $H_2 = 1$ and a standard deviation of heights $\delta = 30$ nm. Thus, the incident light does not directly excite surface polaritons of frequency ω and, as a result, the drc at frequency ω does not display a peak in the retroreflection direction. However,

for small angles of incidence, the drc at frequency 2ω displays a well-defined dip in the retroreflection direction (Figs. 1(a), (b)). A small peak in the direction normal to the mean surface appears on a slope of the backscattering dip at small angles of incidence (Fig. 1(b)). For larger angles of incidence ($\theta_s = 15°$), the dip in the drc at 2ω evolves into a strong and well-defined backscattering peak (Fig. 1(c)) and the background at zero scattering angle becomes flat. Although, in principle, the surface does not contain frequency components that can excite directly surface polaritons at the fundamental frequency, it is conceivable that some weak coupling occurs due to the finite length of the surface and the finite beam width. The additional strong peaks observed in these figures are then diffuse bands arising from the nonlinear mixing of the incident light with surface polaritons of the fundamental frequency [3,10]. It should be noted that the symmetry of the nonlinear interaction of counter-propagating $p-$polarized electromagnetic waves at a planar vacuum-metal interface, which forbids the radiation along the normal to the surface, is broken by the surface roughness, leading to a nonzero background in the direction normal to the surface.

In Fig. 2 we present the contribution to the mean drc from the incoherent component of the scattered light at frequency ω (Fig. 2(a)) and at frequency 2ω (Fig. 2(b)) when the random surface is characterized by the power spectrum (2) with $H_1 = 0.1$, $H_2 = 0.9$ and $\delta = 30$ nm. In this case the mean drc at both the fundamental (Fig. 2(a)) and the harmonic (Fig. 2(b)) frequency displays an enhanced backscattering peak. However, the intensity of the peak at the second harmonic is lower than when the entire power spectrum is centered at $k_{sp}(2\omega)$ (Fig. 1(b)). The peak disappears when the entire power spectrum is centered at $k_{sp}(\omega)$. A dip at zero scattering angle is also seen in Fig. 2(b).

The results obtained support the following physical picture of the processes taking place on a rough nonlinear surface, viz. when the incident light is converted predominantly into surface polaritons of frequency ω, the nonlinear interaction leads to diffuse scattering of volume second harmonic waves while, when the excitation of surface polaritons of the fundamental frequency is suppressed, the surface polaritons of the harmonic frequency are generated efficiently. The coherent constructive/ destructive interference in the multiple

scattering of the latter leads to the appearance of the enhanced backscattering peak/dip. It should be pointed out, that in this case the peak/dip in the direction normal to the mean surface as well as the diffuse bands are strongly suppressed too.

In summary, in this Letter we have presented the results of calculations of the angular distribution of the intensity of the diffuse component of the second harmonic light generated in reflection from a randomly rough metal surface. The results obtained display a peak or a dip in the retroreflection direction in the angular distribution of the intensity of the second harmonic light. For surfaces with the kind of power spectrum employed, we have shown that the intensity of the backscattering peak decreases when surface polaritons at the fundamental frequency are excited. Thus, our calculations show that the existence of surface polaritons at the second harmonic frequency is responsible for the backscattering effects observed at that frequency.

*On leave from: Escuela de Ciencias Físico-Matemáticas, Universidad Autónoma de Sinaloa, México

ML-L, ERM, and TAL gratefully acknowledge the support of CONACYT. The work of AAM was supported in part by the Army Research Office through Grant DAAL 03-92-G-0239.

REFERENCES

1. A. R. McGurn, A. A. Maradudin, and V. Celli, Phys. Rev. B **31**, 4866 (1985).

2. V. M. Agranovich and K. I. Grigorishin, Nonlinear Optics **5**, 3 (1993).

3. A. R. McGurn, T. A. Leskova, and V. M. Agranovich, Phys. Rev. B **44**, 11441 (1991).

4. J. A. Ogilvy, *Theory of Wave Scattering from Random Rough Surfaces* (Hilger, Bristol, 1991), p. 39.

5. F. Toigo, A. Marvin, V. Celli, and N. R. Hill, Phys. Rev. B **15**, 5618 (1977).

6. A. A. Maradudin, T. Michel, A. R. McGurn, and E. R. Méndez, Ann. Phys. (N. Y.) **203**, 255 (1990).

7. V. M. Agranovich and S. A. Darmanyan, Pis'ma Zh. Eksp. Teor. Fiz. **35**, 68 (1982) (JETP Lett. **35**, 80 (1982)).

8. D. Maystre, M. Neviere, and R. Reinisch, Appl. Phys. A **32**, 115 (1986).

9. C. S. West and K. A. O'Donnell, J. Opt. Soc. Am. A **12**, 390 (1995).

10. R. T. Deck and R. K. Grygier, Appl. Opt. **23**, 3202 (1984).

11. J. W. Goodman, *Introduction to Fourier Optics* (McGraw-Hill, San Francisco, 1962), p. 13.

Figure Captions

Fig. 1. The contribution to the mean drc from the incoherent component of the scattered light of frequency 2ω calculated for a surface possessing the power spectrum (3) with $H_1 = 0, H_2 = 1$ and $\delta = 30$ nm. (a) $\theta_0 = 0^o$; (b) $\theta_0 = 3^o$ and (c) $\theta_0 = 15^o$. The broken vertical lines indicates the backscattering direction.

Fig. 2. The contribution to the mean drc from the incoherent component of the scattered light of frequency ω (a) and of frequency 2ω (b) calculated for a surface possessing a rectangular power spectrum (3) with $H_1 = 0.1, H_2 = 0.9$ and $\delta = 30$ nm; $\theta_0 = 15^o$.

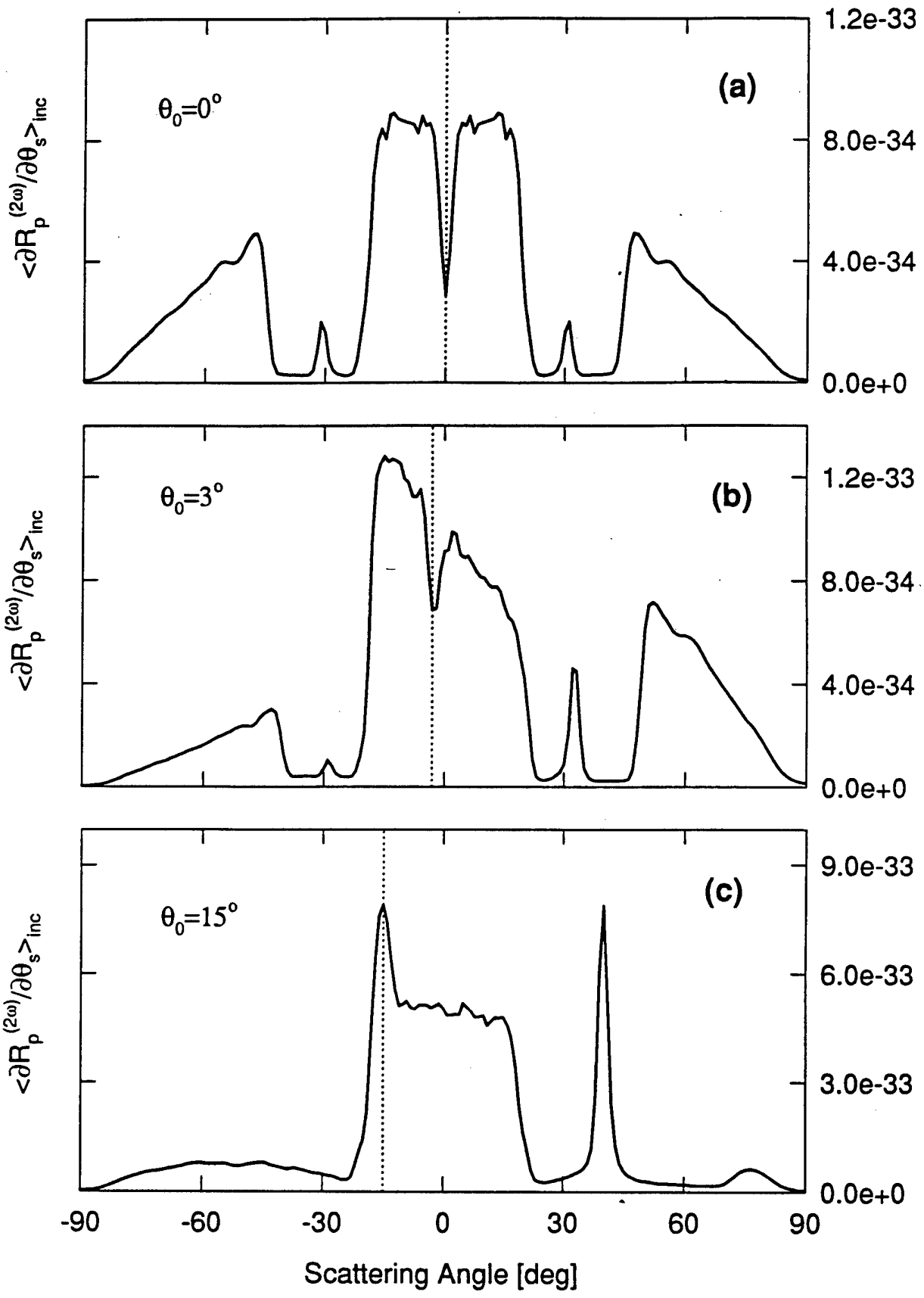
(a)
θ0=0°
(b)
θ0=3°
(c)
θ0=15°
<∂Rp(2ω)/∂θs>inc
1.2e-33
8.0e-34
4.0e-34
0.0e+0
9.0e-33
6.0e-33
3.0e-33
-90
-60
-30
0
30
60
90
Scattering Angle [deg]

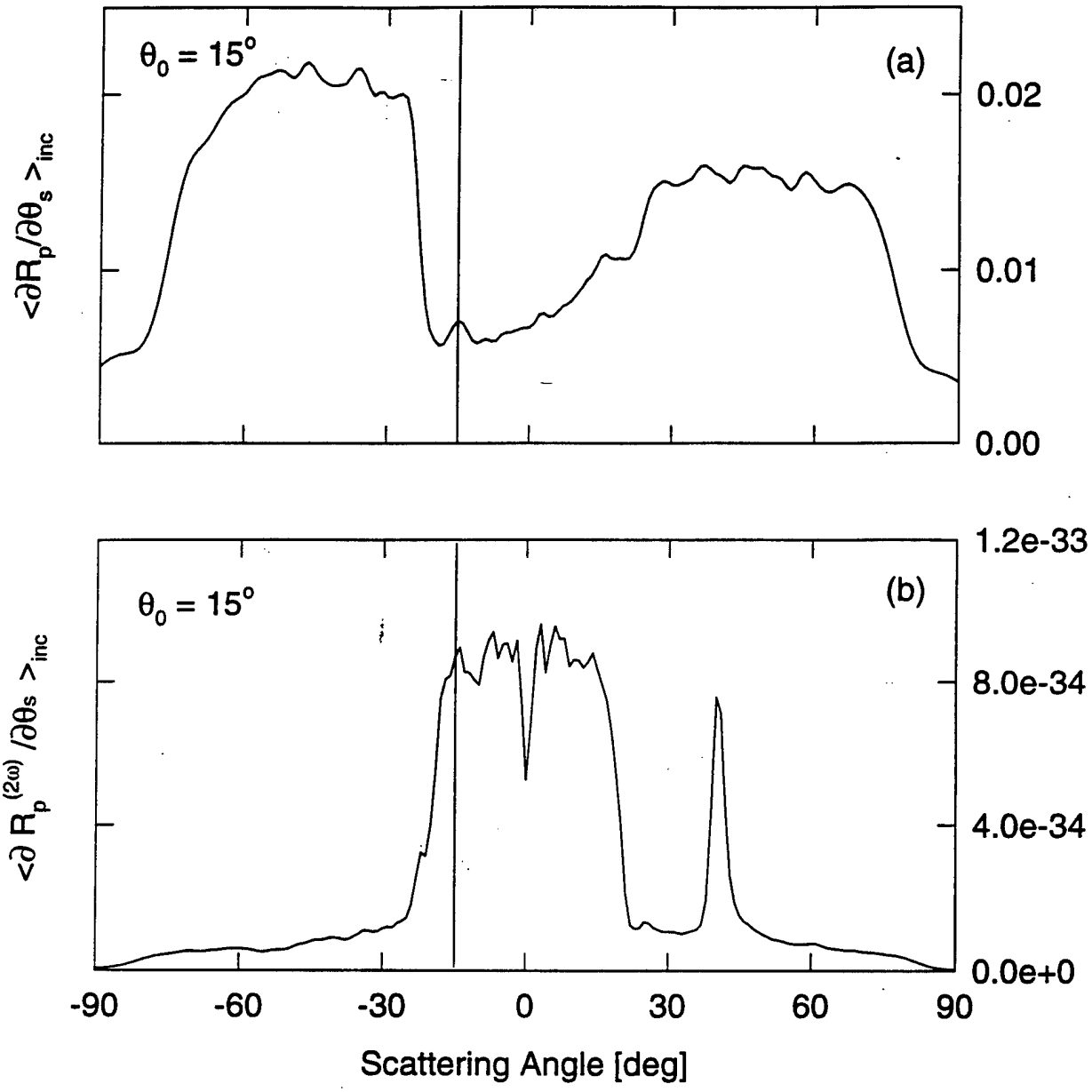
θ0 = 15°
(a)
0.02
0.01
0.00
<∂Rp/∂θs >inc
θ0 = 15°
(b)
1.2e-33
8.0e-34
4.0e-34
0.0e+0
<∂ Rp(2ω) /∂θs >inc
-90
-60
-30
0
30
60
90
Scattering Angle [deg]

Stéphane Mainguy
Centre d'Etudes Scientifiques et Techniques d'Aquitaine
Commissariat à l'Energie Atomique
BP 2; 33114 Le Barp, France

Abstract of the presentation at the Workshop on Rough Surface Scattering and Related Phenomena to be yeld in Yountville, California, June 24-27, 1996

SCATTERING OF INFRARED WAVES BY TWO-DIMENSIONAL RANDOMLY ROUGH DIELECTRIC SURFACES : COMPARISON BETWEEN BRDF MEASUREMENTS AND NUMERICAL SIMULATIONS.

The presentation deals with the phenomenon of optical scattering by realistic surfaces, i.e. two-dimensional surfaces. We have focused our study on monochromatic infrared properties. The wavelength of this study is 10.6 μm. The materials considered are of two kinds : an absorbing glass and a silicon carbide surface that has a metallic behavior at the wavelength of interest. The samples fabrication and characterization concerning optical indexes and roughness are detailed. The BRDF measurements on these samples have been carried out by use of a fully automated in and out of plane laser-light scatterometer. Comparisons of measurements with other laser-light BRDF measurements and incoherent light BRDF measurements are presented. Then we give a confrontation of these measurements with the results of numerical simulations. The calculations are based on the Rayleigh hypothesis and the extinction theorem and consist in an iterative series solution introduced by J.-J. Greffet. The properties are observed in the plane of incidence as well as in planes exterior to this plane. Also results at different angles of incidence up to 80 degrees are examined. The comparison is made for both fondamental polarization states of the incident radiation, p and s.

Diffuse Scattering from One-Dimensional Randomly Rough Metal Surfaces

E. I. Chaikina, A. G. Navarrete, and E.R.Méndez
División de Física Aplicada,
Centro de Investigación Científica y de Educación Superior de Ensenada,
Apartado Posta 2732, Ensenada, Baja California, 22800
México
T.A.Leskova
Institute of Spectroscopy, Russian Academy of Sciences, Troitsk 142092,
Russia

The phenomenon of light scattering from one-dimensional randomly rough surfaces has been studied in resent years by the use of approximate or rigorous electromagnetic theories. There is considerable interest in investigating the scattering properties of random surfaces with different statistical properties experimentally, as a tool for testing the validity of the theoretical approaches to the problem, and to investigate trends in the scattering behavior. Until now it has been difficult to provide critical and complete experimental data for a variety of reasons, not the least of which are the problems that arise in the statistical characterization of experimental surfaces. Relatively subtle statistical properties may play a significant role in the scattering behavior of a random surface [1].

In this paper we present results of experimental studies of the diffuse scattering of electromagnetic waves from one-dimensional randomly rough metal surfaces. The surfaces were fabricated on photoresist, and were subsequently coated with a layer of gold. They were characterized by a mechanical profilometer and, in all cases, both the histogram of heights and the measured surface height correlation function had an approximately Gaussian form. The surfaces have correlation lengths in the range $3 - 15\mu m$, and rms heights in the range $0.30 - 0.75\mu m$. We present the results of measurements of the scattered intensity as a function of the scattering angle for various combinations of the polarization and wavelengths of incident beam. The latter had the values $5.5\mu m$ and $10.6\mu m$. Comparisons of these results with the results of numerical simulations of the scattering problem, and with results of some analytical theories, will be made [2].

References

[1] M. E. Knotts and K. A. O'Donnell, "Comparisons of theory and experiment in light scattering from a randomly rough surface" J. Opt. Soc. Am. A **10**, 928-941 (1993).

[2] A. A. Maradudin and E. R. Mendez, "Enchanced backscattering of light from weakly rough, random metal surfaces" Applied Optics **32**, 3335-3343 (1993).

Resonant Scattering of Electromagnetic Waves from a Rectangular Groove on a Perfectly Conducting Surface

A. V. Shchegrov and A. A. Maradudin
Department of Physics and Astronomy
and Institute for Surface and Interface Science
University of California
Irvine, CA 92717, U.S.A.

T. A. Leskova
Institute of Spectroscopy,
Russian Academy of Sciences,
Troitsk, 142092 RUSSIA

There has been a good deal of attention devoted to surface shape resonances in recent years. These are excitations that are associated with an isolated defect on an otherwise planar surface. They are characterized by discrete, complex frequencies that depend on the shape of the surface perturbation. Surface shape resonances of different origin have been studied, viz. acoustic surface shape resonances associated with local perturbations on the surface of an elastic medium [1-3], magnetostatic surface shape resonances associated with a local perturbation on the surface of a ferromagnetic insulator [4], and electrostatic and electromagnetic surface resonances associated with local perturbations on the surface of a metal or a perfect conductor [5-12]. The electromagnetic surface shape resonances have attracted a great deal of attention as they are believed to play an important role in surface enhanced Raman scattering [13] and in the enhancement of second harmonic generation in reflection from a rough metal surface [14]. However, until now no direct experimental evidence for the existence of electromagnetic surface shape resonances has been provided. Existing studies of the scattering of electromagnetic waves from an isolated ridge or groove on a planar surface of a metal or perfect conductor have dealt mostly with the angular distribution of the intensity of the scattered waves of a given frequency [12, 15-18]. It was shown in [12] in a study of the scattering of a beam of $s-$polarized light from a rectangular groove on the surface of a perfect conductor, that the intensity of the scattered light as a function of its frequency shows well-defined dips at frequencies attributed in [12] to surface shape resonances. The angular dependence of the intensity of the scattered light undergoes a significant rearragement when the frequency of the incident light is

tuned to the vicinity of those particular frequencies.

In our paper we present a theory of light scattering from a single rectangular groove on the surface of a perfect conductor (Fig. 1). The frequencies of the electromagnetic surface shape resonances and the scattering of a Gaussian beam of $p-$ and $s-$polarized light from such a surface are calculated by both the modal approach [15-18] and a numerical method based on Green's second integral identity [19, 20]. We show that two different phenomena occuring in the system lead to a complicated frequency dependence of the differential reflection coefficient (drc). The first is the interference of the fields in the groove leading to a minimum of the total field in the plane of the surface, $x_3 = 0$, in the case of $s-$polarized light, and to a minimum of the normal derivative of the total field in the plane $x_3 = 0$ in the case of $p-$polarized light. As a result, the incident light is reflected predominantly in the specular direction, thus leading to the suppression of the scattering into other directions and, as a consequence, to the appearance of dips in the drc for scattering angles far from the specular direction. The second phenomenon is the existence of the surface shape resonances. We show that the presence of the $p-$polarized surface shape resonances leads to the appearance of dips at their frequencies in the drc. However, the frequencies of the $s-$polarized surface shape resonances fall in the close vicinity of the frequencies at which the field in the throat of the groove reaches its minimum value. As a result, the influence of the shape resonances on the drc is masked by the strong dips connected with the interference effects.

We assume that $p-$ or $s-$polarized light of frequency ω is incident from the vacuum side onto the surface depicted in Fig.1, with the plane of incidence being the x_1x_3-plane. Then for $p-$polarized light the only nonzero component of the magnetic field vector is $H_2(x_1, x_3|\omega)$, while for $s-$polarized light the only nonzero component of the electric vector is $E_2(x_1, x_3|\omega)$.

We seek the field in the vacuum region $x_3 > 0$ as a sum of an incident and a scattered field,

$$E_2(x_1, x_3|\omega) = e^{ikx_1 - i\alpha(k,\omega)x_3} + \int_{-\infty}^{\infty} \frac{dq}{2\pi} e^{iqx_1 + i\alpha(q,\omega)x_3} R^{(s)}(q|k), \tag{1}$$

$$H_2(x_1, x_3|\omega) = e^{ikx_1 - i\alpha(k,\omega)x_3} + \int_{-\infty}^{\infty} \frac{dq}{2\pi} e^{iqx_1 + i\alpha(q,\omega)x_3} R^{(p)}(q|k), \tag{2}$$

with

$$\alpha(q,\omega) = \sqrt{\frac{\omega^2}{c^2} - q^2}, \ Re\alpha(q,\omega) > 0, \ Im\alpha(q,\omega) > 0. \tag{3}$$

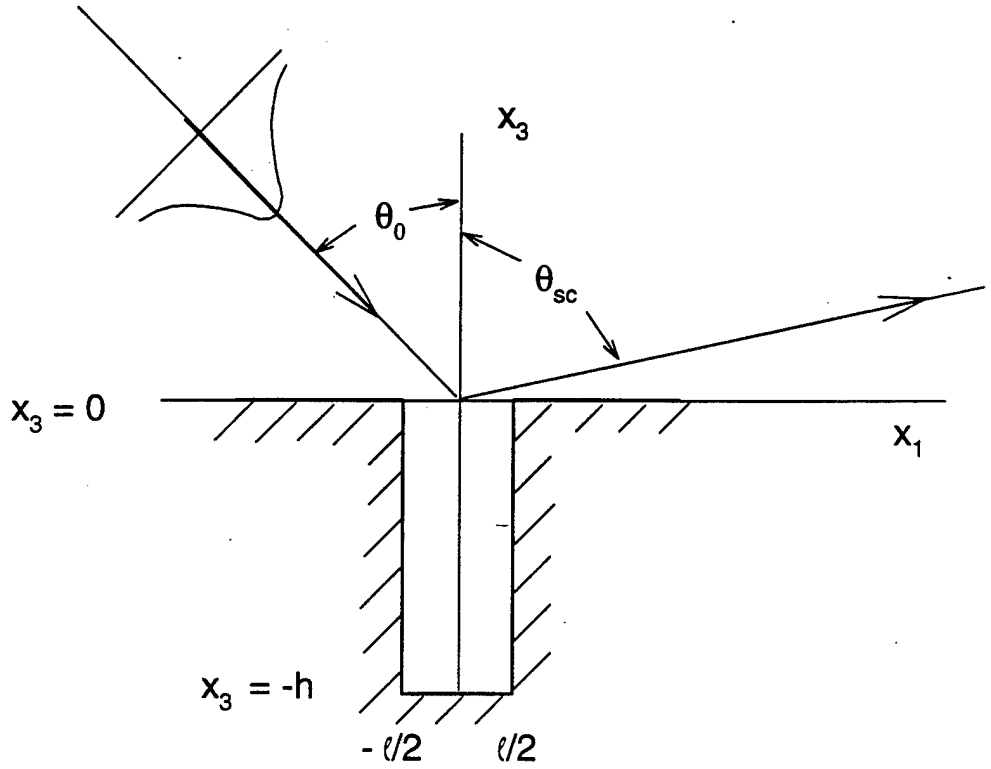

Fig.1 The scattering geometry.

The field in the groove can be expressed in terms of modal functions which are the solutions of Maxwell's equations satisfying the boundary conditions at the surfaces $x_3 = -h$ and $x_1 = \pm l/2$ for each polarization:

$$E_2(x_1, x_3|\omega) = \sum_{n=1}^{\infty} B_n^{(s)} \sin[\alpha_n(\omega)(h + x_3)] \sin\left[\frac{\pi n}{l}(x_1 - l/2)\right], \tag{4}$$

$$H_2(x_1, x_3|\omega) = \sum_{n=0}^{\infty} B_n^{(p)} \cos[\alpha_n(\omega)(h + x_3)] \cos\left[\frac{\pi n}{l}(x_1 - l/2)\right], \tag{5}$$

where

$$\alpha_n(\omega) = \sqrt{\frac{\omega^2}{c^2} - \left(\frac{\pi n}{l}\right)^2}, \; Re\alpha_n(\omega) > 0, \; Im\alpha_n(\omega) > 0. \tag{6}$$

Matching the fields and their derivatives at the plane $x_3 = 0$ and eliminating the scattering amplitude we obtain a matrix equation for the coefficients $\{B^{(p,s)}\}$

$$\overleftrightarrow{D}^{(s,p)} \vec{B}^{(s,p)} = \vec{A}^{(s,p)}, \tag{7}$$

where the vector $\vec{A}^{(s,p)}$ has the components

$$A_n^{(s)}(\omega) = -2i\alpha(k,\omega) S_n^{(s)*}(k), \tag{8}$$

$$A_n^{(p)}(\omega) = 2S_n^{(p)*}(k), \tag{9}$$

with $k = (\omega/c)\sin\theta_0$ and

$$S_n^{(s)}(q) = \frac{4}{l}\frac{n\pi/l}{q^2 - (n\pi/l)^2}\left[\frac{1-(-1)^n}{2}\cos(ql/2) - i\frac{1+(-1)^n}{2}\sin(ql/2)\right], \tag{10}$$

$$S_n^{(p)}(q) = \frac{4}{l}\frac{q}{q^2 - (n\pi/l)^2}\left[i\frac{1-(-1)^n}{2}\cos(ql/2) + \frac{1+(-1)^n}{2}\sin(ql/2)\right]. \tag{11}$$

The elements of the matrices $\overleftrightarrow{D}^{(s,p)}$ are

$$D_{mn}^{(s)}(\omega) = \alpha_n(\omega) h \cos[\alpha_n(\omega)h]\delta_{mn} + M_{mn}^{(s)}(\omega)\sin[\alpha_n(\omega)h], \tag{12}$$

where δ_{mn} is the Kronecker delta and

$$M_{mn}^{(s)}(\omega) = -2i\frac{h}{l}\left(\frac{m\pi}{l}\right)\left(\frac{n\pi}{l}\right)\left[1+(-1)^{n+m}\right] \times$$
$$\times \int_{-\infty}^{\infty}\frac{dq}{2\pi}\frac{\alpha(q,\omega)\left[1-(-1)^n e^{iql}\right]}{(q^2-(n\pi/l)^2)(q^2-(m\pi/l)^2)}, \tag{13}$$

and

$$D_{mn}^{(p)}(\omega) = \cos[\alpha_n(\omega)h]\delta_{mn} + M_{mn}^{(p)}(\omega)\alpha_m(\omega) h \sin[\alpha_n(\omega)h], \tag{14}$$

where

$$M_{mn}^{(p)}(\omega) = -2i\frac{1}{lh}\left[1+(-1)^{n+m}\right]\int_{-\infty}^{\infty}\frac{dq}{2\pi}\frac{q^2\left[1-(-1)^n e^{iql}\right]}{\alpha(q,\omega)(q^2-(n\pi/l)^2)(q^2-(m\pi/l)^2)}. \tag{15}$$

Finally, the scattering amplitudes $R^{(s,p)}(q|k)$ are found to be

$$R^{(s)}(q|k) = -2\pi\delta(q-k) -$$
$$-il\alpha(k,\omega)h\sum_{m=1}^{\infty}\sum_{n=1}^{\infty}\sin[\alpha_m(\omega)h]S_m^{(s)}(q)(\overleftrightarrow{D}^{(s)}(\omega))_{mn}^{-1}S_n^{(s)*}(k), \tag{16}$$

and

$$R^{(p)}(q|k) = 2\pi\delta(q-k) + \\ +i\frac{l}{2\alpha(q,\omega)h}\sum_{m=0}^{\infty}\sum_{n=0}^{\infty}\sin[\alpha_m(\omega)h]S_m^{(p)}(q)(\overleftrightarrow{D}^{(p)}(\omega))_{mn}^{-1}S_n^{(p)*}(k). \quad (17)$$

Up to this point we have assumed that the incident field is a plane wave. In the case when a finite beam of the form

$$\mathcal{F}(x_1,x_3|\omega)_{inc} = \frac{w\omega}{2\sqrt{\pi}c}\int_{-\pi/2}^{\pi/2}d\theta e^{-(\omega^2w^2/4c^2)(\theta-\theta_0)^2}e^{i(\omega/c)(x_1\sin\theta - x_3\cos\theta)}, \quad (18)$$

where $\mathcal{F}(x_1,x_3|\omega)_{inc}$ stands for either $E_2(x_1,x_3|\omega)_{inc}$ in the case of $s-$polarization or for $H_2(x_1,x_3|\omega)_{inc}$ in the case of $p-$polarization, θ_0 is the angle of incidence, and w is the half-width of the beam, is incident onto the surface, the magnitude of the total time-averaged incident flux is

$$P_{inc}^{(s,p)} = L_2\frac{cw}{32\pi\sqrt{2\pi}}\left[erf\left(\frac{w\omega}{c\sqrt{2}}(\pi/2-\theta_0)\right)+erf\left(\frac{w\omega}{c\sqrt{2}}(\pi/2+\theta_0)\right)\right], \quad (19)$$

where L_2 is the length of the surface in the x_2-direction, and $erf(x)$ is the error function. The time-averaged flux scattered scattered into the direction θ_{sc} is

$$P^{(s,p)}(\theta_{sc}) = L_2\frac{\omega}{16\pi^2}\cos^2\theta_{sc}|R^{(s,p)}(q,\omega)|^2, \quad (20)$$

where $q = (\omega/c)sin\theta_{sc}$ and

$$R^{(s,p)}(q,\omega) = \frac{w\omega}{2\sqrt{\pi}c}\int_{-\omega/c}^{\omega/c}dk\,R^{(s,p)}(q|k)\frac{1}{\alpha(k,\omega)}e^{-(w^2\omega^2/4c^2)(\sin^{-1}(ck/\omega)-\theta_0)^2}. \quad (21)$$

The differential reflection coefficient (drc), which gives the fraction of the total energy incident onto the surface that is scattered into an angular interval $d\theta_{sc}$ about the scattering direction defined by the scattering angle θ_{sc}, is then given by [20],

$$\frac{\partial R^{(s,p)}}{\partial\theta_{sc}} = \frac{P^{(s,p)}(\theta_{sc})}{P_{inc}^{(s,p)}}. \quad (22)$$

We now turn to a discussion of the results obtained. The frequencies of the surface shape resonances associated with the rectangular groove are the frequencies at which

the determinant of the matrix $\overleftrightarrow{D}^{(s,p)}$ in Eq.(7) vanishes. It is seen from Eqs.(13) and (15) that the elements $M_{mn}^{(s,p)}(\omega)$ vanish unless m and n have the same parity, which means that the equation $\det \overleftrightarrow{D}^{(s,p)}(\omega) = 0$ breaks up into two separate equations for the frequencies of surface shape resonances whose electric field ($s-$polarization) and magnetic field ($p-$polarization) are even and odd functions of x_1. The solutions of the equations $\det \overleftrightarrow{D}^{(s,p)}(\omega) = 0$ are complex, reflecting the fact that they fall into the frequency region of bulk electromagnetic waves. We have evaluated the functions $|\det \overleftrightarrow{D}^{(s,p)}(\omega)|^{-2}$ as functions of ω numerically to obtain the frequencies of the lowest frequency surface shape resonances of even and odd symmetry. A plot of $|\det \overleftrightarrow{D}^{(s,p)}(\omega)|^{-2}$ as a function of the frequency ω is shown in Fig.2. It should be pointed out that the nondiagonal elements of the matrices $\overleftrightarrow{M}^{(s,p)}$ are negligibly small in comparison with the diagonal elements. Therefore, to obtain accurate values of the frequencies of the lowest frequency resonances it is enough to evaluate determinants of 1×1 matrices for resonances of each symmetry. In this case the frequencies are primarily defined by the solutions of

$$\cos[\alpha_1(\omega)h] = 0 \tag{23}$$

for $p-$polarized resonances, and

$$\tan[\alpha_1(\omega)h] = \frac{\alpha_1^5(\omega)l^4c}{2\pi\omega}\sqrt{\frac{\omega l}{2\pi c}}e^{-i(\omega l/c-\pi/4)} \tag{24}$$

for $s-$polarized resonances. In obtaining Eq.(24) we have taken into account that the solutions of $\det \overleftrightarrow{D}^{(s)}(\omega) = 0$ group just below the cutoff frequency determined by $\alpha_n(\omega) = 0$ in the frequency region where $\alpha_n(\omega) \ll \omega/c$. In this case the solutions of Eq. (24) are close to the solutions of $\sin[\alpha_1(\omega)h] = 0$. The terms omitted in these estimates (Eqs. (23) and (24)) contribute only a small shift of the frequencies. As in the determination of the surface shape resonance frequencies the contribution of each mode to the scattering amplitude is significant only in the frequency region below the cutoff frequency, so that in the frequency region of the lowest frequency shape resonances ($l < \lambda < 2l$) the main contributions comes from the first modes in the modal representations (4) and (5). As expected, the field inside the groove has its maximum value at the frequencies of the surface shape resonances. However, the contributions of the leading modes to the fields $E_2(x_1, x_3|\omega)$ and $\partial H_2(x_1, x_3|\omega)/\partial x_3$ on the plane $x_3 = 0$ vanish at the frequencies defined by the zeros of $\sin[\alpha_n(\omega)h]$.

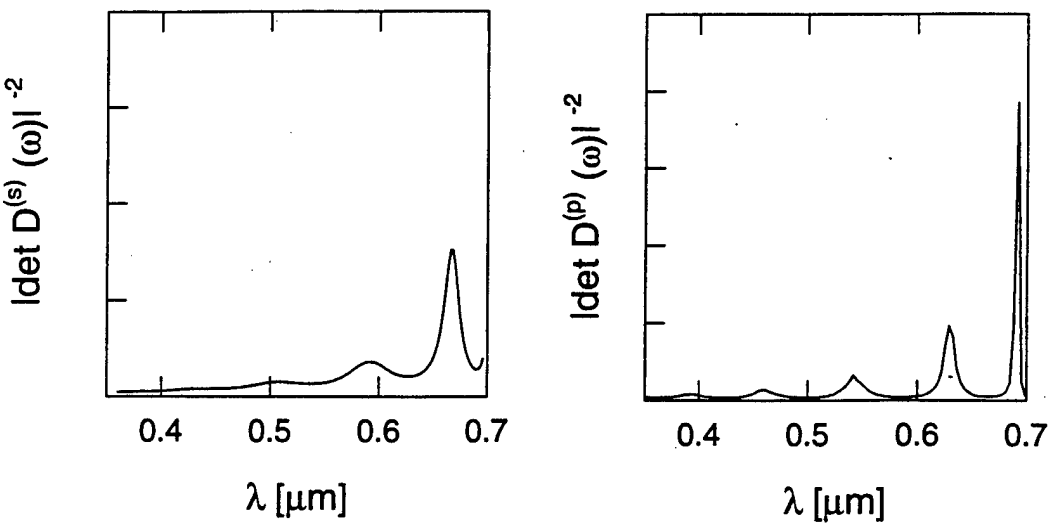

Fig.2 (a) $|\det \overleftrightarrow{D}^{(s)}(\omega)|^{-2}$ and (b) $|\det \overleftrightarrow{D}^{(p)}(\omega)|^{-2}$ for a rectangular groove with $l = 0.35\mu m$ and $h = 1\mu m$

This means that the boundary conditions for a perfect conductor are almost restored on the plane $x_3 = 0$, and this results in the decrease of scattering out of the specular direction. The latter gives rise to dips in the frequency dependence of the drc for scattering angles far from the specular direction. These dips were attributed incorrectly to surface shape resonances in Ref. 12.

In the case of $s-$polarization, in the lowest frequency region we are interested in, the corresponding frequencies almost coincide with the frequencies of the surface shape resonances, given by Eq. (24). It should be pointed out that Eq.(24) gives a good approximation to the frequencies of the $s-$polarized resonances only for the first two or three solutions which group just below the cutoff frequency. As the frequency increases, Eq.(24) transforms into Eq.(23), so that the frequencies of the s-polarized surface shape resonances shift from the positions of the dips associated with the vanishing of the modal field at $x_3 = 0$. However, the imaginary part of the solutions grows with the solution number, thus preventing them from influencing the drc.

In the case of $p-$polarization the lowest order mode associated with the magnetic field independent of x_1 has no cutoff and leads to the appearance of dips in the frequency dependence of the drc at the frequencies $\omega_n = n\pi c/hc$. The lowest frequency $p-$polarized mode giving rise to the surface shape resonances turns out to be the odd mode, so that at normal incidence the Gaussian beam does not feel the presence of

the surface shape resonances. However, at oblique incidence in the frequency region of the dominant influence of this mode both the surface shape resonances and the minima of the mode field give rise to dips in the drc. The somewhat simplified analysis presented above describes very well the behaviour of the fields and the drc in the frequency region just above the cutoff frequency for the odd mode of the lowest order. With increasing of the frequency the higher order modes become important and, thus, complicate the frequency dependence of the drc.

In addition to the modal expansion approach, we also used the method of moments [19,20] based on Green's second integral identity to solve the scattering problem. Although the former approach gives a deeper understanding of the problem, the latter allows obtaining an exact solution for an arbitrarily shaped surface profile. We define the surface profile by the parametric equations $x_1 = \xi(s)$, $x_3 = \eta(s)$, where the parameter s measures the arc length of the curved surface. The functions $P^{(s,p)}(\theta_{sc})$ introduced in Eq.(20) can then be represented as [20]

$$P^{(s,p)}(\theta_{sc}) = L_2 \frac{c^2}{64\pi^2\omega} |r_{s,p}(\theta_{sc})|^2, \tag{25}$$

where the functions $r_{s,p}(\theta_{sc})$ are defined by

$$r_s(\theta_{sc}) = -\int ds\, e^{-i\frac{\omega}{c}[\xi(s)\sin\theta_{sc}+\eta(s)\cos\theta_{sc}]} F(s|\omega), \tag{26}$$

$$r_p(\theta_{sc}) = i\frac{\omega}{c}\int ds\, e^{-i\frac{\omega}{c}[\xi(s)\sin\theta_{sc}+\eta(s)\cos\theta_{sc}]} [\eta'(s)\sin\theta_{sc} - \xi'(s)\cos\theta_{sc}] H(s|\omega), \tag{27}$$

with $F(s|\omega) = \left[-\eta'(s)\frac{\partial}{\partial x_1} + \xi'(s)\frac{\partial}{\partial x_3}\right] E_2(x_1, x_3|\omega)$ and $H(s|\omega) = H_2(x_1, x_3|\omega)$ evaluated at $(x_1, x_3) = (\xi(s), \eta(s))$. The functions $F(s|\omega)$ and $H(s|\omega)$ satisfy the integral equations

$$F(s|\omega) = F(s|\omega)_{inc} - \int ds' \mathcal{H}_0^T(s|s') F(s'|\omega), \tag{28}$$

$$H(s|\omega) = H(s|\omega)_{inc} + \int ds' \mathcal{H}_0(s|s') H(s'|\omega), \tag{29}$$

where $F(s|\omega)_{inc} = \left[-\eta'(s)\frac{\partial}{\partial x_1} + \xi'(s)\frac{\partial}{\partial x_3}\right] \mathcal{F}(x_1, x_3|\omega)_{inc}$ and $H(s|\omega)_{inc} = \mathcal{F}(x_1, x_3|\omega)_{inc}$ evaluated at $(x_1, x_3) = (\xi(s), \eta(s))$. The kernels of Eqs.(28)–(29) have the form

$$\mathcal{H}_0(s|s') = \frac{i}{4}\left[-\eta'(s')\frac{\partial}{\partial\xi(s')} + \xi'(s')\frac{\partial}{\partial\eta(s')}\right] \times$$
$$\times H_0^{(1)}\left(\frac{\omega}{c[(\xi(s) - \xi(s') - \varepsilon\eta'(s))^2 + (\eta(s) - \eta(s') + \varepsilon\xi'(s))^2]^{1/2}}\right), \tag{30}$$

$$\mathcal{H}_0^T(s|s') = \frac{i}{4}\left[-\eta'(s)\frac{\partial}{\partial\xi(s)} + \xi'(s)\frac{\partial}{\partial\eta(s)}\right] \times$$
$$\times H_0^{(1)}\left(\frac{\omega}{c[(\xi(s)-\xi(s')+\varepsilon\eta'(s'))^2+(\eta(s)-\eta(s')-\varepsilon\xi'(s'))^2]^{1/2}}\right). \qquad (31)$$

Here $H_0^{(1)}(z)$ is a Hankel function of the first kind and ε is a positive infinitesimal. In solving Eqs.(28) and (29) by the method of moments, we replace the infinite range of integration by the finite one $(0, L)$, where L is the arc length of the part of the surface profile we consider. We point out that the singular points of the surface profile, $(x_1, x_3) = (-l/2, 0)$, $(l/2, 0)$, $(-l/2, -h)$, and $(l/2, -h)$ give no contribution to the integrals, as was shown in Ref.21. Therefore, we can divide the range $(0, L)$ into three subranges on each of which there are no singular points. Then we divide each of these subranges into intervals of equal arc length $\Delta s = L/N$ [19], where N is the total number of the intervals on the surface. The method of moments then yields $F(s|\omega)$ and $H(s|\omega)$ at the midpoint of each interval. Finally, we calculate the functions $P^{(s,p)}(\theta_{sc})$ from Eqs. (25)–(27). The results obtained by the method of moments agree with those obtained by the modal expansion method.

In Fig. 3 the drc for the $p-$polarized light is plotted as a function of frequency for different angles of incidence and scattering along with the function $|\det D^{(p)}(\omega)|^{-2}$. At normal incidence the dips in the drc appear at the wavelengths given by $\lambda_n = 2h/n$, at which the normal derivative of the magnetic vector almost vanishes at the plane $x_3 = 0$. At oblique incidence, however, the positions of the dips shift to the position of the maxima in the frequency dependence of $|\det D^{(p)}(\omega)|^{-2}$.

In conclusion, in this paper we have first demonstrated the existence of electromagnetic surface shape resonances associated with a rectangular groove on a perfectly conducting surface. We have have then shown that in both $p-$ and $s-$polarizations the differential reflection coefficient displays well-defined dips which are due to the vanishing, or almost vanishing, of the total field ($s-$polarization) and its normal derivative ($p-$polarization) at the plane $x_3 = 0$. The presence of the $p-$polarized surface shape resonances leads to the appearance of dips at their frequencies in the drc. However, the frequencies of the $s-$polarized surface shape resonance fall in the close vicinity of the frequencies at which the total field in the throat of the groove reaches its minimum value. As a result, the influence of the $s-$polarized surface shape resonances on the drc is masked by the strong dips caused by the interference effects.

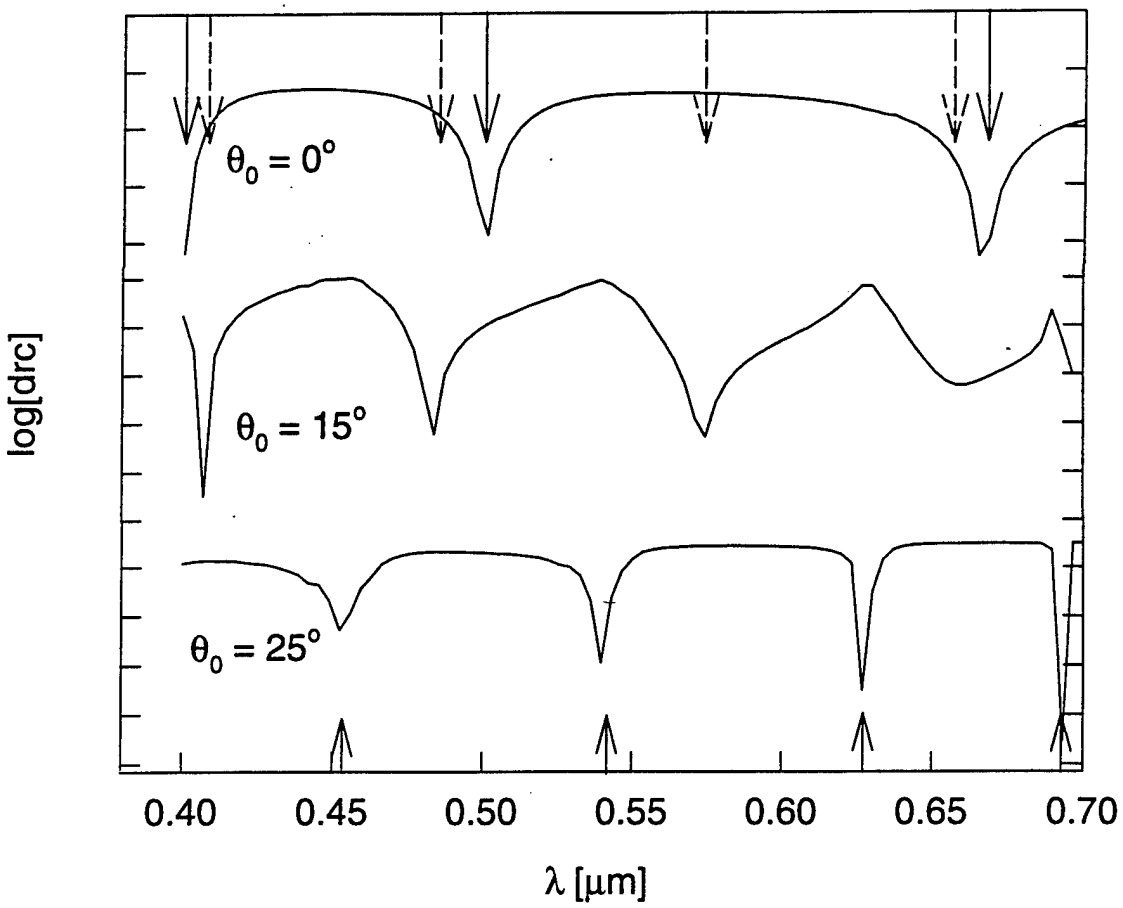

Fig. 3 The drc for $p-$polarized light scattered from a recatangular groove with $l = 0.35\mu m$ and $h = 1\mu m$ at a fixed scattering angle $\theta_{sc} = 30^o$ and different angles of incidence, as a function of the wavelength of the incident light. The arrows pointing up show the wavelengths of the surface shape resonances. The arrows pointing down show the wavelengths at which the normal derivative of the total field at $x_3 = 0$ has its mininum value: the solid arrows pointing down show the wavelengths $\lambda_n = 2h/n$ at which the normal derivative of the first even mode vanishes, viz. the zeros of $\sin[\alpha_0(\omega)h]$; the dashed arrows pointing down show the wavelengths $\lambda_n = 2/\sqrt{(n/h)^2 + (1/l)^2}$ at which the normal derivative of the first odd mode vanishes, viz. the zeros of $sin[\alpha_1(\omega)h]$.

References

[1] A. A. Maradudin, P. Ryan, and A. R. McGurn, Phys. Rev. B **48**, 3068 (1988).

[2] A. R. Baghai-Wadji and A. A. Maradudin, in *Boundary Elements XIV, vol. 1: Field Problems and Applications.* eds. C. A. Brebbia, J. Dominguez, and F. Paris (Elsevier, New York, 1992), p.231.

[3] A. V. Shchegrov and A. A. Maradudin, Appl. Phys. Lett. **67**, 3090 (1995).

[4] A. A. Maradudin, in *Surface Waves in Plasmas and Solids*, ed. S. Vukovich (World Scientific, Singapore, 1986), p.220.

[5] D. W. Berreman, Phys. Rev. **163**, 855 (1967).

[6] R. W. Rendell, D. J. Scalapino, and B. Mülschlegel, Phys. Rev. Lett. **41**, 1746 (1978).

[7] R. W. Rendell and D. J. Scalapino, Phys. Rev. B **24**, 3276 (1981).

[8] R. Ruppin, Solid State Commun. **39**, 903 (1981).

[9] P. C. Das and J. I. Gersten, Phys. Rev. B **25**, 6281 (1982).

[10] A. G. Mal'shukov and Sh. A. Shekhmamet'ev, Fiz. Tverd. Tela (Leningrad) **25**, 2623 (1983) [Sov. Phys. – Solid State **25**, 1509 (1983)].

[11] A. A. Maradudin and W. M. Visscher, Z. Phys. B **60**, 215 (1985).

[12] A. Zuniga–Segundo and O. Mata–Mendez, Phys. Rev. B **46**, 536 (1992).

[13] See, e.g. *Surface-Enhanced Raman Scattering*, eds. R. K. Chang and T. E. Furtak (Plenum, New York, 1982).

[14] C. K. Chen, A. R. B. de Castro, and Y. R. Shen, Phys. Rev. Lett. **46**, 145 (1981).

[15] A. Wirgin and A. A. Maradudin, Phys. Rev. B **31**, 5573 (1985).

[16] K. Barkeshli and J. L. Volakis, IEEE Transactions on Antennas and Propagation **39**, 804 (1991).

[17] T. J. Park and H. J. Eom, J. Appl. Phys. **73**, 3571 (1993).

[18] R. A. Depine and D. C. Skigin, J. Opt. Soc. Am. A **11**, 2844 (1994).

[19] A. Mendoza–Suárez and E. R. Méndez (unpublished work).

[20] A. A. Maradudin, T. Michel, A. R. McGurn, and E. R. Méndez, Ann. Phys. (N. Y.) **203**, 255 (1990).

[21] A. Mendoza–Suárez (unpublished work).

Statistics of eigenmodes in microwave cavities with rough boundaries

E. Kanzieper

The Jack and Pearl Resnick Institute of Advanced Technology,
Department of Physics, Bar-Ilan University, Ramat-Gan 52900, Israel

The statistics of the local amplitudes v of the eigenfunctions of a closed system with rough boundary is studied within the framework of the random matrix theory (RMT)[1]. This problem is proved to be rather general, being equally related to the statistics of the wave field in microwave resonators and acoustic reverberation rooms, and to that of electrons confined in quantum dots as well[2]. It is shown that this statistics is entirely determined by the symmetry of the real microscopic problem but it is insensitive to the microscopic details (such as boundary shape, statistical properties of the surface roughness, etc.). Whereas the RMT-approach leads to the conclusion about the absence of correlations between wavefunctions belonging to different eigenstates, these correlations are shown to survive for the wavefunctions within given eigenstate but taken at different spatial points inside irregularly shaped closed system. The latter statement follows from the analysis of the joint probability distribution of the modulus square of the wavefunctions at two different spatial points. Moreover, it is turned out that the correlations between fluctuations of the wavefunctions at different spatial points depend on their amplitudes. The large fluctuations remain strongly correlated at large distances of the order $\xi = \lambda v^{1/(d-1)}$, while correlation length for small fluctuations behaves as $\xi = \lambda\sqrt{v}$ (here λ is the eigenmode wavelength, and d is the dimensionality of the closed system). The general results derived within the framework of the phenomenological RMT-approach exactly coincide with those obtained, for example, by straightforward solution of the Shrödinger equation for electrons in a disordered quantum dot by means of the zero-dimensional version of the non-linear σ-model[3,4].

---

1. V. Freilikher, E. Kanzieper, and I. Yurkevich, Physical Review E **54** (1996)
2. A. Kudrolli, V. Kidambi, and S. Sridhar, Physical Review Letters **75**, 822 (1995)
3. M. Srednicki, preprint cond-mat/9512115
4. V. N. Prigodin, Physical Review Letters **74**, 1566 (1995)

Near field microcopy of rough surfaces: perspectives and challenges

Mehdi Vaez-Iravani

Tencor Instruments,
2444 Charleston Road,
Mountain View,
CA 94043.

Abstract

The application of near-field scanning optical microscopy in general imaging is discussed. Some of the challenges facing the technique in probing rough surfaces are enumerated. It is argued that direct imaging of rough surfaces may be subject to significant coherent effects which must be considered in image interpretation. The role and nature of feedback systems, amplitude, and phase signals are examined.

1. Introduction

Near field scanning optical microscopy is the study of those phenomena that occur over a sub-wavelength distance from an object {1,2}. Naturally, the process involves the use of a probe in this region to achieve a resolution beyond the diffraction limit {3-6}. The fact that one is dealing with light opens a vast number of possible configurations, and contrasts. Indeed, near field microscopy has been demonstrated in probing amplitude {5,7,8}, phase {9,10}, polarization {11-14}, in fluorescence and photoluminescence detection, imaging, and spectroscopy {15-19}, and in the measurement of critical dimensions {20}. In all these cases, the NSOM probe has been used to illuminate the sample in question. Yet, the tip can also be used to collect the signal in the near-field, allowing the probing of an existing field. Some examples of the application of the NSOM in this area are the detection of waveguide modes, laser diode outputs, and the polarization effects of high numerical aperture focusing {21-23}.

In the context of rough surfaces, the NSOM takes on the posture of a non-contact stylus, and as such the main contrast mechanisms that need be considered are the amplitude, and phase in the near-field. At the same time, we note that in this particular application the sample is perhaps the most tolerant of the inevitable heating effect at the sharpened tip (in case of a fiber probe) {24}. One can then consider using a relatively large input power into the fiber to optimize signal to noise.

In this paper, we review and examine the role of the NSOM in imaging rough surfaces, and discuss some of the challenges facing the theoreticians and experimentalists in this field.

2. Nature of force regulation mechanism

The vast majority of NSOM's in use today operate on the principle of force regulation of the tip/sample separation. This involves operating the tip in near resonance condition in the close vicinity of the sample, and observing the change in the tip oscillation amplitude upon scanning the sample under the tip {5,7,25}. The prevalent view of the mechanisms of the modulation of the tip oscillation amplitude have been i) the reduction of the amplitude due to the presence of a layer of contamination on samples and ii) the resolved component of the Van der Waales attractive forces along the direction of the oscillation. Recently, however, there has been a suggestion that the contrast mechanism is the reduction in amplitude of the free tip oscillation due to the contact of the sample and the tip at one extreme of the cycle. This latter case would be highly reminiscent of the tapping mode AFM. The resolution of this problem is of significance both to the near-field optics and force microscopy communities. In addition, there is direct experimental evidence of the effect of surface conditioning, including hydrophobicity and hydrophilicity on the tip approach {21}. The challenge to the community is to establish the true nature of this regulation mechanism, and to investigate the subtle effects of departures from the different models.

3. Nature of amplitude imaging in near-field microscopy of rough surfaces

Although the advent of force regulation substantially alleviates the problem of tip crash and destruction in viewing real surfaces, one basic question remains: what is the nature of the optical signal in imaging a rough surface? Consider the case of viewing a rough surface in reflection using an aperture NSOM. The light exits through a small aperture, and illuminates the part of the sample directly under the tip. The scattered light then illuminates the surrounding area. The radiation is gathered by a relatively high NA lens, typically set at an angle w.r.t. the sample. Thus, the signal at a given scan position is a function not only of the sample point under the tip, but also the surrounding points. The problem is somewhat alleviated in practice due to the fact that the radiation scattered at a given point quickly loses its evanescent components. The directly illuminated point is, therefore, substantially more significant to the overall signal strength at that scan position than the surrounding. In this regard, it is advantageous to employ a near field illumination and collection mode, in which the same probe is employed for both purposes. However, the great reduction in the light level due to the double passage of light through the aperture is a major problem (see section 4). Whatever the experimental arrangement, there is a need for an in-depth analysis of the situation to establish the limits of applicability of aperture NSOM to rough surfaces.

The case of apertureless NSOM operating on the principle of probe induced scattering of the proximity field, due to a diffraction limited illuminated spot {6}, is even more complex. In the case of a rough surface, there is a great deal of multiple scattering within the spot, as well as the surrounding area. Hence, the probed field at any given scan position is affected by the surrounding features. Clearly, the degree to which this effect alters the image is a function of such features as the porosity, complex refractive index, and the relative distance of the prevalent

features within the field.

Regardless of the method, in both of the above cases the fact that the tip is in the close vicinity of the sample means that operation in reflection is accompanied by sample-induced, or tip-induced, shadowing {20}.

4. Nature of phase imaging in force regulated NSOM

In the diffraction limited domain phase contrast provides a sensitive method of probing the surface roughness, and the same holds true in the near-field. However, the fact that one is dealing with a much reduced optical power level renders the experimental implementation of phase contrast in the near-field a considerably more complicated proposition. Indeed, the demonstration of this in both transmission and reflection formats has been in a pseudo-heterodyne arrangement {9,10}. For a sample showing pure topography and no variation in dielectric constant, the force regulation mechanism will provide a trace of the topography. On the other hand, in cases of samples with both a variation in the dielectric constant, and topography, the simultaneity of the force signal and near-field phase contrast can be invaluable. Recent theoretical work has indicated that the important parameter in near-field imaging is not the height alone, but the product of the height and the differential dielectric constant {26}. It should thus be possible to separate these parameters and substantially to enhance the available amount of information about samples. A particularly significant application of near field phase contrast may be in the area of imaging biological structures.

5. Conclusions

Some of the applications and challenges facing near-field scanning optical microscopy have been discussed. Clearly, the field continues to attract a good deal of serious and casual curiosity in various disciplines. In using the NSOM, however, it is particularly important to remember its inherent limitations. In so far as the application of the NSOM as a profiler of rough surfaces is concerned, it is, perhaps, worth noting that much of the information potentially furbished by the NSOM probe is available form the force regulation part. Any attempt to extract additional information from the optical data should strictly account for the various interactions taking place. Much emphasis needs to be placed on the simultaneity of the acquired data using different modalities. The direct deconvolution of the information in a data inversion process remains an attractive possibility.

References

1. Pohl, D.W., Denk, W., and Lanz, M. (1984) Image recording with resolution λ/20, *Appl. Phys. Lett.* **44**, 652-653.
2. Lewis, A., Isaacson, M., Haootunian, A., and Muray, A. (1984) Development of a 500 A spatial resolution light microscope, *Ultramicroscopy* **13**, 227.
3. Betzig, E., Trautman, J.K., Harris, T.D., Weiner, J.S., and Kostelak, R.L. (1991) Breaking the diffraction barrier: optical microscopy on a nanometric scale, *Science* **251**, 1468-1470.
4. Fischer, U. Ch., and Zapletal, M. (1992) The concept of a coaxial tip as a probe for scanning near-field optical microscopy and steps towards a realization, *Ultramicroscopy* **42**, 393-398.
5. Toledo-Crow, R., Yang, P.C., Chen, Y., and Vaez-Iravani, M. (1992) Near-field differential scanning optical microscope with atomic force regulation, *Appl. Phys. Lett.* **60**, 2957-2959.
6. Zenhausern, F., O'Boyle, M.P., and Wickramasinghe, H.K., Apertureless near field optical microscope, *Appl. Phys. Lett.* **65**, 1623-1625.
7. Betzig, E., Finn, P.L., and Weiner, J.S. (1992) Combined shear force and near-field scanning optical microscopy, *Appl. Phys. Lett.* **60**, 2484-2486.
8. van Hulst, N.F., Moers, M.H.P., Noordman, O.F.J., Faulkner, T., Serink, F.B., van der Werf, B., de Grooth, G., and Bolger, B. (1992) Operation of a scanning near field optical microscope in reflection in combination with a scanning force microscope, *SPIE* **1639**, 36-43.
9. Vaez-Iravani, M. and Toledo-Crow, R. (1993), Phase contrast and amplitude pseudo-heterodyne interference near-field scanning optical microscopy, *Appl. Phys. Lett.* **62**, 1044-1046.
10. Pilevar, S., Atia, W.A., Davis, C.C. (1995) Reflecetion Near-Field Scanning Optical Microscopy: An interferometric approach, *Proc. NFO3,* Brno, May 9-11.
11. Betzig, E., Trautman, J.K., and Weiner, J.S. (1992) Polarization contrast in near-field scanning optical microscopy, *Appl. Opt.* **31**, 4563-4568 (1992)
12. Betzig, E., Trautman, J.K. Wolfe, R., Gyorgy, E.M., Finn, P.L., Kryder, M.H., and Chang, C.H. (1992), Near-field magneto-optic and high density data storage, *Appl. Phys. Lett.* **61**, 142-144.
13. Vaez-Iravani, M. and Toledo-Crow, R. (1993), Pure linear polarization imaging in near-field scanning optical microscopy, *Appl. Phys. Lett.* **63**, 138-140.
14. Ade, H., Toledo-Crow, R., Vaez-Iravani, M., and Spontak, R.J., Observation of polymer birefringnce in near-field optical microscopy, *Langmuir* (in press)
15. Trautman, J.K., Macklin, J.J., Brus, L.E., and Betzig, E. (1994) Near-field spectroscopy of single molecules at room temperature, *Nature* **369**, 40-42.
16. Hess, H.F., Betzig, E., Harris, T.D., Pfeiffer, L.N., and West, K.W. (1994) Near- field spectroscopy of the quantum constituents off a luminescent system, *Science* **264**, 1740-1745.
17. Xie, X.S. and Dunn, R.C. (1994) Probing single molecule dynamics, *Science* **265**, 361-364.

18. Rogers, J.K., Seiferth, F., and Vaez-Iravani, M. (1995) Near-field probe microscopy of porous silicon: observation of spectral shifts in photoluminescence of small particles, *Appl. Phys. Lett.* **66**, 3260-3262.
19. Rogers, J.K., Toledo-Crow, R., Vaez-Iravani, M. DiFrancisico, G., Zhao, T., and Hailstone, R. (1995) Correlative near-field direct/fluorescence imaging and spectroscopy of a sensitizing dye on single microcrystals of silver halide, *Jour. Imag. Sci. Tech.* **39**, 205.
20. Toledo-Crow, R., Smith, B.W., Rogers, J.K., Vaez-Iravani, M. (1994) Near-field optical microscopy characterization of IC metrology, *SPIE* **2196**, 62-73.
21. van Hulst, N.F., *Ultramicroscopy* (in press)
22. Burratto, S.K., Hsu, J.W.P., Trautman, J.K., Betzig, E., Bylsma, R.B., Bahr, C.C., and Cardillo, M.J. (1994), *Jour. Appl. Phys.* **76**, 7720.
23. Toledo-Crow, R., Rogers, J.K., Seiferth, F., and Vaez-Iravani, M. (1995) Contrast mechanisms and imaging modes in near field optical microscopy, *Ultramicroscopy* **57**, 293-297.
24. Kavaldjiev, D.I., Toledo-Crow, R., and Vaez-Iravani, M. (1995) On the heating of the fiber tip in a near-field scanning optical microscope, *Appl. Phys. Lett.* **67**, 2771-2773.
25. Yang, P.C., Chen, Y., and Vaez-Iravani, M. (1992) Attractive mode force microscopy with optical detection in an orthogonal cantilever/sample configuration, *Jour. Appl. Phys.* **71**, 2499.
26. Carminati, R., and Greffet, J.J. (1995), Influence of dielectriv contrast and topography on the near field scatteredby an inhomogeneous surface, *Jour. Opt. Soc. Amer. A* **12**.

Numerical Study of a Scatter-Probe Near Field Optical Microscope

Eugenio R. Méndez*
Departamento de Física de la Materia Condensada
Instituto de Ciencia de Materiales de Madrid, CSIC
Cantoblanco 28049 Madrid, Spain

Near field optical microscopy has been successful in demonstrating the possibility of beating the diffraction limit of conventional optical systems. In near field optics the resolution is primarily determined by the size of the probe and resolutions of about $\lambda/10$ are routinely achieved with these instruments. Efforts are now being made by several groups for improving our understanding of the relation between the object and the image, and for improving the resolution currently achievable. Most of the reported systems seem to be limited to resolutions of about 50 nm. This is not, however, a fundamental limitation but a consequence of the technical difficulties involved in making finer and efficient optical probes.

A minor trend in near field optical microscopy, but one that has already demonstrated near atomic resolution [1], consists of using scatterers rather than the tapered optical waveguides employed by more conventional systems to illuminate the sample (SNOM) or pickup the near field intensity scattered by it (PSTM). Several different schemes of apertureless or scatter-probe microscopes have been proposed (see e. g. [2], [3], and [4]), but the weakness of the signals and the complexity of the image formation process have probably contributed to their relatively low profile. Nevertheless, the production of metallic probes of near atomic dimensions, such as those employed in the STM, is a practical proposition and thus, provided that some progress on the problem of image interpretation is made, scatter probe near field optical scanning microscopy represents a potentially promising and useful technique.

The basic idea behind scatter-probe near field microscopy may be visualized as follows. The probe, being small in comparison with the wavelength, creates a scattered evanescent field that upon interaction with the sample generates a propagating field that can be detected in the far field (the probe acts as a source). Alternatively, one may prefer to think that the evanescent waves present in the neighborhood of the sample, can be converted into propagating waves by the presence of the probe. Of course, since the interaction between the probe and the sample can be strong none of these naive pictures is entirely correct, but they provide an indication of the resolution that one might expect from the technique.

In this work we present a numerical study of a scanning scatter probe near field optical microscope working in reflection. The system considered, depicted in Fig. 1, is invariant along the x_2-direction, and the plane of incidence of the electromagnetic field is the x_1x_3-plane. For purely s- or p-polarized waves incident on the system the state of polarization is retained during the scattering process, and these two fundamental polarizations may be treated separately. In a typical numerical experiment the system is illuminated by a plane wave with an angle of incidence θ_0, and the scattered light is detected in the direction θ_s. The method of calculation is based on the "integral equation" formalism described in Ref. [5]. Employing Green's integral theorem, coupled integral equations that determine the source functions (the field and its normal derivative) along the boundaries of the two objects shown in Fig. 1 are established. The boundaries of the objects may be described as parametric curves which are functions of the parameter s, the arc length. Then, in the discretization of the coupled integral equations, the sampling interval Δs can be chosen as constant for a given section of the curves. Also, to reduce the time of calculation, an impedance boundary condition applicable to this formulation [6] is employed. This

* Permanent Address: División de Física Aplicada, Centro de Investigación Científica y de Educación Superior de Ensenada, Apdo. Postal 2732, Ensenada, B. C., 22800 México.

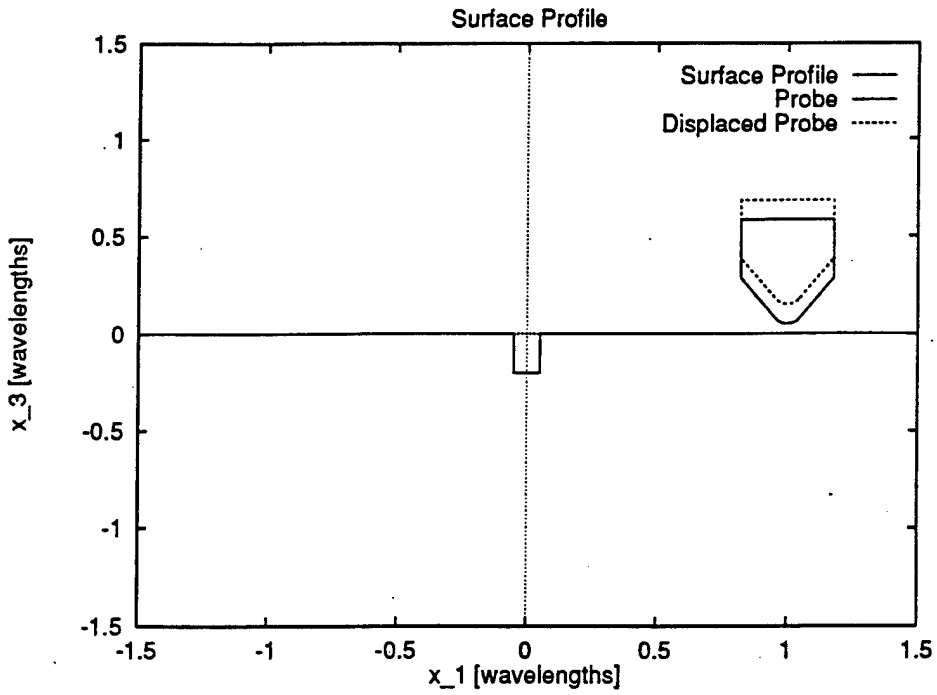

Figure 1: Schematic diagram of the system studied. The probe and the sample are characterized by complex dielectric constants $\epsilon_p(\omega)$ and $\epsilon(\omega)$, respectively.

approximation, accurate for cases in which $|\epsilon(\omega)|$ is large, eliminates one of the unknown source functions of the scattering problem. The matrix equation obtained through such a procedure is solved using standard numerical techniques. This provides the unknown source function which in turn is used to calculate the scattered field.

In our study, a vibrating probe is simulated by calculating *the signal* associated to a point on the sample as the difference between the intensities obtained in the far field with the probe situated in two vertically displaced positions (see Fig. 1). The image is then formed using the calculated signal for each position of the probe along x_1 as it is scanned over the sample at constant height. Images of various structures obtained under different conditions of illumination and detection will be presented. Particular attention will be given to the strength of the detected signal as a function of the angles of incidence and detection, and to the effects of polarization and optical properties of the materials on the calculated images.

References

1.- F. Zenhausern, M. P. O'Boyle, and H. K. Wickramasinghe, Appl. Phys. Lett. **65**, 1623-1625 (1994).

2.- J. D. Pedarnig, M. Specht, W. M. Heckle, and T. W. Hänsch, in *Near Field Optics*, D. W. Pohl and D. Courjon, eds., Kluwer Academic Publishers (Dordrecht, 1993), p. 273-280.

3.- Y. Inouye and S. Kawata, Opt. Lett. **19**, 159-161 (1994).

4.- R. Bachelot, P. Gleyzes, and A. C. Boccara, Opt. Lett. **20**, 1924-1926 (1995).

5.- A. Mendoza-Suárez and E. R. Méndez, "Light scattering by a reentrant fractal surface," submitted to Appl. Opt. (1996).

6.- A. Mendoza-Suárez and E. R. Méndez, "Derivation of an impedance boundary condition for one-dimensional, curved, reentrant surfaces," submitted to Opt. Commun. (1996).

Recent progress in the analysis of image formation in near-field optical microscopy

Jean-Jacques Greffet, Rémi Carminati
Laboratoire EM2C, Ecole Centrale Paris, CNRS
F-92295, Châtenay-Malabry Cedex, France

Several experimental set-ups producing images with super-resolution have been designed in the last ten years[1, 2]. In most cases, the relationship between topography, dielectric contrast and images is not fully understood. In this talk, we shall discuss the main features of the imaging process and propose a possible solution for the inverse problem.

The first topic is devoted to the analysis of the interaction of the tip with the surface under unspection. It will be shown that the tip can be accounted for by introducing a transfer function that relates the intensity (square modulus of the electric field) to the signal detected by a tip, namely, the flux of energy in the optical fiber. This concept relies on the assumption of a passive probe[3]. The validity of this approximation will be discussed[4].

The second topic of the presentation is the analysis of the images produced in the detection mode. It was observed that the images depend on the polarization, angle of incidence and coherence of the source. These effects will be analysed in the framework of a perturbative theory in order to extract the relevant parameters and to provide a simple understanding of the main features of the images[5]. In particular, we will show that all the effects of polarization and coherence of the illumination can be accounted for by an Impulse Response[4]. This concept will be introduced and illustrated by numerical simulations.

The third topic deals with the solution of the inverse problem. Is it possible to discriminate between topography and dielectric contrast ? Is it possible to reconstruct a surface profile from near field data ? It will be shown that for most structures studied in near field, the optical image yields a coupled information on the topography and the dielectric contrast. Thus, it is not possible to obtain a purely optical information and different structures may produce the same optical image. We will show that an equivalent surface profile acounting for both dielectric contrast and topography can be introduced[4]. An inversion procedure based on the knowledge of the impulse response will be described[6, 7, 8]. Some numerical simulations will be presented. It will be shown that the reconstruction procedure enhances the resolution.

Two usual ways of producing images are the constant height mode and constant intensity mode. We will show that in the regime where perturbative analysis is valid, these two modes yields the same images. Finally, we shall discuss the implications of reciprocity in near-field optics.

1. Courjon, D. and Bainier, C. (1994) Near-field microscopy and near-field optics, *Rep. Prog. Phys.* **57**, 989-1028.
2. Pohl, D.W. (1992) Nano-optics and Scanning Near-Field Optical Microscopy, in R. Wiesendanger and H.J.Güntherodt (ed.), *Scanning Tunneling Microscopy II*, Springer-Verlag, Berlin, pp. 233-271.
3. Carminati, R. and Greffet, J.J. (1995) Two dimensional numerical simulation of the Photon Scanning Tunneling Microscope. Concept of transfer function., *Opt. Commun.* **116**, 316-321.
4. Greffet, J.-J. and Carminati, R. *Theory of imaging in near-field microscopy* 1-1-26 (Kluwer Academic Publishers, 1996).
5. Carminati, R. and Greffet, J.J. (1995) Influence of dielectric contrast and topography on the near field scattered by an inhomogeneous surface, *J. Opt. Soc. Am. A* **12**,
6. Greffet, J.-J., Sentenac, A. and Carminati, R. (1995) Surface profile reconstruction using near field data, *Opt. Commun.* **116**, 20-24.
7. Carminati, R., Greffet, J.-J., Garcia, N. and Nieto-Vesperinas, M. (1996) Direct reconstruction of surfaces from near-field intensity under spatially incoherent illumination, *Opt. Lett.* **21**, 501-503.
8. Garcia, N. and Nieto-Vesperinas, M. (1995) Direct solution to the inverse scattering problem for surfaces from near-field intensities without phase retrieval, *Opt. Lett.* **20**, 949-951.

Light Scattering From Bodies Either in Front or Behind Corrugated Interfaces

M. Nieto-Vesperinas and A. Madrazo
Instituto de Ciencia de materiales, C.S.I.C.
and Departamento de Fisica de la Materia Condensada
Universidad Autonoma , C-III, Madrid 28049, SPAIN

Abstract

We shall present a study of the scattering of light and other electromagnetic waves from systems formed by a corrugated interface with a body either in front or behind it.

We shall show how the solution of this problem can be of interest in several practical situations, namely, in achieving superresoluiton of the surface corrugation by near field optical microscopy, or, reciprocally, in the detection of objects hidden behind randomly rough surfaces.

As regards surface characterization, we shall show how the presence of a body close to the surface transfers all the information of the near field into the far zone by scattering on it. This is the basis of recently developed near field optical microscopes in which light is scattered into the far zone by metallic particles or STM tips, thus dramatically increasing the resolution over that of previous SNOM systems, and, hence allowing resolution in the range of a few nanometers [1]-[3]. In our work we explicitly show how this process of conversion of the near field into the far field is achieved.

Concerning hidden object detection [4], [5], we shall show how their presence behind rough surfaces can be detected due to the dramatic increase of the backscattering peak that they produce.

References

[1] Y. Inouye and S. Kawata, Opt. Lett. **19**, 159 (1994).

[2] F. Zenhausern, Y. Martin and H. K. Wickramasinghe, Science **269**, 1083 (1995)

[3] H. K. Wickramasinghe, Y. Martin, and F. Zenhausern, Scanning Interferometric Apertureless Microscopy at 10 angstrom resolution, in *Optics at the Nanometric Scale: Imaging and Storing with Photonic Near Fields*, M. Nieto-Vesperinas and N. Garcia, eds., *NATO - ASI Series*, Vol. E-319, (Kluwer, Dordrecht, 1996).

[4] I. Tsang, J. A. Kong, and R. T. Shin, *Theory of Microwave Remote Sensing*, (Wiley, New York, 1996).

[5] A. J. Sieber, EMSL Newsletter 7:2 (1996).

Scattering and imaging of rough surfaces

C.J.R. Sheppard
Department of Physical Optics, School of Physics, University of Sydney,
NSW 2006 Australia

Scattering by rough surfaces in the Kirchhoff approximation is considered in terms of three-dimensional spatial frequencies. This has some advantages for understanding general trends of scattering behaviour, and allows the inverse problems of determining profiles or their statistics from scattering measurements.

In recent years considerable advances have been made in the rigorous theories of surface scattering. A variety of methods have been employed, including differential methods, based on coupled wave or modal methods, and integral equation methods. However, whilst such approaches have been useful in explaining specific phenomena, such as enhanced backscatter for example, they suffer from the problem of mathematical complexity, which results in the following limitations:

- It is difficult to extract overall trends in the behaviour.
- The problem of scattering by two-dimensional surfaces, including skew rays, is computationally difficult.
- Studies of imaging of rough surfaces, including investigation of speckle phenomena, are computationally intensive.
- Integration over scattering (as in total integrated scatter, TIS, measurements) or incidence angles is computationally intensive.
- Inverse problems of determining surface profiles or their statistics from scattering data are generally intractable.

The Kirchhoff approximation has been shown to give good prediction of the scattered light under the conditions that the radius of curvature of the profile is large compared with the wavelength, the surface slope is small enough so that shadowing effects or multiple scattering are negligible, scattering angles are not too large and vectorial effects are not important. It should be noted that the Kirchhoff approximation is valid for rough surfaces, with height variations of many wavelengths, as long as the above conditions are satisfied.

Scattering can be specified by the scattering function, which gives the complex amplitude of the scattered plane wave components for a given incident wave. For a random surface profile we can specify the BRDF (bidirectional reflectance distribution function), which gives the intensity of the scattered waves. Both these quantities satisfy the reciprocity property, which is valid in general, even with loss and multiple scattering.

The scattering function for a surface of profile $\varsigma(x,y)$ is given by[1,2]

$$S(\mathbf{p}) = \frac{\mathbf{p}^2}{2s} \int\int\int_{-\infty}^{\infty} \delta\left(z - \zeta(x,y)\right) \exp\{-ik\mathbf{p} \bullet \mathbf{r}\} d\mathbf{r} \qquad (1)$$

where

$$\begin{aligned} \mathbf{p} &= p\mathbf{i} + q\mathbf{j} + s\mathbf{k} \\ p &= p_2 - p_1 \\ q &= q_2 - q_1 \\ s &= \left(1 - p_1^2 - q_1^2\right)^{1/2} + \left(1 - p_2^2 - q_2^2\right)^{1/2} \\ \mathbf{r} &= x\mathbf{i} + y\mathbf{j} + z\mathbf{k} \\ k &= 2\pi / \lambda \end{aligned} \qquad (2)$$

and p_1, q_1, p_2, q_2 are the direction cosines of incidence and scattering. The three-dimensional (3-D) spatial frequencies p,q,s represent particular directions for incident and scattered light.

The form of Eq.1 is seen to be very simple compared with expressions in terms of polar coordinates. We can see that

1) The scattering is constrained within a sphere of radius $|\mathbf{p}| = 2$, which is the well-known Ewald sphere.

2) The scattering, which is in general a function of four direction cosines, two for incidence and two for scattering, becomes only a function of three quantities, the three-dimensional spatial frequencies.

3) Each point in $\mathbf{p}$ space represents two reciprocal scattering situations.

4) Scattering over a range of scattering angles, or incidence angles, can be determined by integration over the 3-D spatial frequencies.

To model imaging of the surface, the image can be calculated by integrating over the incident and scattered plane waves. This can be done using rigorous[3-5] or Kirchhoff[6-8] scattering data. The scattering data has to be multiplied by the 3-D transfer function of the optical system before integration.[9-12]

The confocal surface profiling method consists of finding the axial position, for each point of the surface, of the peak in intensity of the 3-D image.[13] We have investigated numerically this algorithm for reconstructing a surface profile from scattering data.[14] Then after finding the axial position of the peak intensity we recover the surface profile. The confocal profiling method can thus be regarded as a non-linear reconstruction based on the Kirchhoff approximation. Alternative algorithms[15] are based on interference microscopy.[16,17]

Imaging of stratified media can also be modeled by a similar procedure.[18] For weak changes in refractive index, but including multiple reflections, the image amplitude can be inverted to reconstruct the profile.[19] Generalizing to the case of a 3-D distribution of refractive index, a scattering potential can be defined[20] for reflection imaging. Similar methods can be used for transmission based on the Born or Rytov approximations.[7,19]

Turning now to random surface profiles, the BRDF for an isotropic rough surface, neglecting the coherent specular reflection, is[21,22]

$$BRDF = \frac{\pi \mathbf{p}^4}{2\lambda^2 s^2} \int_0^{\infty} \left[\chi_2(s,-s) - \chi(s)\chi^*(s)\right] J_0(k\ell\tau)\tau\, d\tau \tag{3}$$

where $\chi(s)$ is the characteristic function associated with the height variation, $\chi_2(s,-s)$ is the joint characteristic function of the distribution, and

$$\ell = k\left(p^2 + q^2\right)^{1/2} \tag{4}$$

is the normalized radial transverse spatial frequency. For the important case of a surface governed by a normally distributed continuous stationary random process with zero mean, with a distribution function $w(\varsigma)$ of heights ς

$$w(\varsigma) = \frac{1}{\sigma\sqrt{2\pi}} \exp\left(-\varsigma^2 / 2\sigma^2\right) \tag{5}$$

where σ is the RMS surface height we then have[22]

$$BRDF = \frac{\pi L^2 \mathbf{p}^4}{2\lambda^2 s^2} \left\{ \exp\left(-k^2 s^2 \sigma^2\right) \int_0^{\infty} \left[\exp\left(k^2 s^2 \sigma^2 C(t)\right) - 1\right] J_0(k\ell L t)\, t\, dt \right\} \tag{6}$$

were $C(t)$ is the correlation coefficient and $t = \tau / L$ with L the correlation length.

The expression in braces in Eq.6 for the isotropic case is a function of two dimensionless parameters $ks\sigma$, $k\ell\tau$ which can be regarded as normalised roughness and correlation length, or alternatively as normalised axial and transverse spatial frequencies. The behaviour with variation of wavelength is also immediately apparent.

The BRDF has been calculated from Eq.6 for random surfaces with a variety of statistics such as a Gaussian correlation coefficient[21] or a surface with exponential correlation (fractal with an outer scale).[23] Eq.6 also shows that if the BRDF is known the correlation coefficient can be recovered by an inverse Hankel transformation. [22]

It is straightforward to integrate Eq. 6 over scattering angles to calculate the total integrated scatter[24] in the Kirchhoff approximation and find a resultant correction factor for a Gaussian random surface, for example. If the correlation length is too small, or the rms surface height too large, for the TIS to be proportional to the roughness, the correction factor allows the correct roughness to be predicted.

References

1. Sheppard CJR, Connolly TJ, Gu M (1993) Scattering by a one dimensional rough surface and surface reconstruction by confocal imaging, *Phys. Rev. Letts.* **70**, 1409-1412.
2. Sheppard, C.J.R., Connolly T.J., and Gu Min (1993) Imaging and reconstruction for rough surface scattering in the Kirchhoff approximation by confocal microscopy, *J. Mod. Opt.* **40**, 2407-2421.
3. Sheppard CJR, Sheridan JT (1989) Micrometrology of thick structures, *Proc. SPIE* **1139**, 32-39.
4. Sheridan JT, Sheppard CJR (1993) The coherent imaging of periodic thick fine isolated structures, *J. Opt. Soc. Amer.* A **10**, 614-632.
5. Sheridan JT, Sheppard CJR (1994) Modelling of images of square-wave gratings and isolated edges using rigorous diffraction theory, *Opt. Commun.***105**, 367-378.
6. Sheppard CJR, Heaton JM (1984) Images of surface steps in coherent illumination, *Optik*, **68**, 267-280.
7. Sheppard CJR, Heaton JM (1984) Confocal images of straight edges and surface steps, *Optik*, **68**, 371-380.
8. Sheppard CJR, Carlini AR, Matthews HJ (1988) Three-dimensional imaging of phase steps, *Optik*, **80**, 91-94.
9. Sheppard CJR (1989) General considerations of diffraction theory of 3-D imaging, *European J. Cell Biology*, Suppl. 25, **48**, 29-32.
10. Sheppard CJR, Cogswell CJ (1990) Three-dimensional image formation in confocal microscopy, *J. Microsc.* **159**, 179-194.
11. Sheppard CJR, Gu M, Mao XQ (1991) Three-dimensional coherent transfer function in a reflection-mode confocal scanning microscope, *Opt. Commun.* **81**, 281-284.
12. Sheppard CJR, Gu Min, Kawata Y, Kawata S (1994) Three-dimensional transfer functions for high aperture systems, *J. Opt. Soc. Amer.* A **11**, 593-598.
13. Cox IJ, Sheppard CJR (1983) Digital image processing of confocal images, *Image and Vision Computing* **1**, 52-56.
14. Quartel JC, Sheppard (1996) Surface reconstruction using an algorithm based on confocal imaging*J. Mod. Opt.* **43** 469-486
15. Quartel JC, Sheppard CJR (1996) A surface reconstruction algorithm based on confocal interferometric imaging, *J. Mod. Opt* . **43** 591-606
16. Hamilton DK, Sheppard CJR (1982) A confocal interference microscope, *Optica Acta* **29**, 1573-1577.
17. Matthews HJ, Hamilton DK, Sheppard CJR (1986) Surface profiling by phase-locked interferometry, *Appl. Optics* **25**, 2372-2374.
18. Sheppard CJR, Connolly TJ, Lee J, Cogswell C (1994) Confocal imaging of a stratified medium, *Appl. Opt.* **33**, 631-640.
19. Sheppard CJR, Gu M (1994) Modeling of 3-D brightfield microscope images, *Proc. SPIE* **2302**, 352-358.
20. Sheppard CJR, Connolly TJ, Gu Min (1995) The scattering potential for imaging in the reflection geometry, *Opt. Commun.* **117**, 16-19
21. Sheppard CJR, Connolly TJ (1995) Imaging of random surfaces, *J. Mod. Opt.* **42**, 861-881
22. Sheppard CJR (1996) Simplified expressions for the bidirectional reflectance distribution function, *J. Mod. Opt.*. **42** 373-380
23. Sheppard CJR (1996) Scattering by fractal surfaces with an outer scale, *Opt. Commun.* **122**, 178-188
24. Sheppard CJR, Roy M (1995) Total integrated scatter in the Kirchhoff approximation, *Optik*, in press.

Nonlinear and Linear Inverse Scattering

John Sylvester
Mathematics Department
University of Washington

This presentation is part of a joint project with Dale Winebrenner of the Applied Physics Laboratory at the University of Washington. The focus of the project is to probe the electro-magnetic properties, and, in particular, the depth of sea ice via microwave remote sensing.

We model the ice as a medium with index of refraction depending only on depth with the incident field being a plane wave. Ice is a lossy medium, but what I will describe here are features of a lossless, non-dispersive model. There are, apparently more complicated, analogs of everything I will describe here for the model which includes loss, but the theory is not yet complete.

The lossless remote sensing problem for a medium which depends only on depth leads to a 1-dimensional scattering/inverse scattering problem. By *forward scattering*, we mean the mathematical problem of calculating the complex valued (amplitude and phase) reflection coefficient at various frequencies given a hypothetical non-dispersive index of refraction. By *inverse scattering* we mean the opposite, the calculation of the index of refraction from a (potentially very noisy) complex reflection coefficient over a wide frequency band.

The only feature of this one dimensional inverse scattering problem which makes it more than a simple question in signal analysis is the presence of *multiple reflections*. If we ignore these multiple reflections, the scattering and

inverse scattering problems become linear and much more tractable. We shall refer to (idealized) scattering without multiple reflections as *Linear Scattering.* In the language of mathematicians, linear scattering is the (Frechet) derivative of nonlinear scattering at the constant background.

The moral of this lecture is that a surprising number of the main features of linear scattering have exact analogs for nonlinear scattering (i.e. in the presence of multiple reflections)

In order to be more specific, we need to cast linear scattering in its most transparent form. We will need to write down a few formulas and will introduce new independent and dependent variables. Instead of the physical depth coordinate, z, we will use the *travel time depth* $x(z)$ defined via the formula:

$$x(z) = \int_0^z n(s)ds \tag{1}$$

where n denotes the index of refraction. Secondly, we will denote the variation in the logarithm of the index of refraction with respect to travel time by α; that is,

$$\alpha(x) = \frac{d\,\log(n)}{dx} \tag{2}$$

It is possible to compute the index of refraction as a function of the physical depth, from its logarithmic variation, α, as a function of travel time depth – this requires solving a single nonlinear ordinary differential equation.

With these new variables the linear scattering transformation becomes exactly the the Fourier transform, i.e.

$$r_L(\omega) = \widehat{\alpha}(\omega) := \int_{\infty}^{0} \mathrm{e}^{-2i\omega x}\alpha(x)dx \tag{3}$$

The subscript L is to emphasize that this is the linear reflection coefficient, which doesn't account for multiple reflections.

Basic Tools and Features of Linear Scattering

The Plancherel Equality

$$\int_{-\infty}^{\infty} |r_L(\omega)|^2 d\omega = \frac{\pi}{4} \int_{-\infty}^{0} \alpha(x)^2 dx$$

This equality says a lot about the stability of any linearized inversion process. It tells us that the linearized reflection coefficient of a square integrable α will also be square integrable, and should therefore be calculated in terms of a basis of square integrable functions.

First and Last Reflections (Paley-Weiner Theorem)

Think for a moment about the reflection of a pulse in the time domain. There is a well defined first arrival time, when the first reflection is detected, and, in the absence of multiple reflections, there is also a well defined last arrival time. Thus it is possible to locate the top and bottom of an inhomogeneous perturbation of a constant background from reflection data in a simple way. The Paley-Weiner Theorem is the mathematical statement of how to detect the support of the variation (the places where α is nonzero) from its Fourier transform.

The Shannon Sampling Theorem

If the inhomogeneity has a finite depth, D, then it is sufficient to sample r_L at discrete frequencies spaced $\frac{1}{D}$ apart.

The Hilbert Transform and Causality

Any function f can be decomposed into it's it causal and *a-causal* pieces.

$$f = f^+ + f^-$$

If we apply this decomposition to $e^{-2i\omega D} r_L(\omega)$ we decompose r into the parts of the reflection generated by reflections below and above (travel time) depth D. For a pulse in the time domain, this corresponds to the parts of the reflected wave that arrive after and before time D .

We call f^+ the Hilbert transform of f. The decomposition is orthogonal with respect to the norm in the Plancherel equality, i.e.

$$\int_{-\infty}^{\infty} |f|^2 d\omega = \int_{-\infty}^{\infty} |f^+|^2 d\omega + \int_{-\infty}^{\infty} |f^-|^2 d\omega$$

Basic Tools and Features of Nonlinear Scattering

The point of this lecture is that the tools of linear scattering which we listed above have nonlinear analogs. We list them below:

The Nonlinear Plancherel Equality

$$\int_{-\infty}^{\infty} \log(1 - |r(\omega)|^2) d\omega = \frac{\pi}{4} \int_{-\infty}^{0} \alpha(x)^2 dx$$

This guarantees stability of the nonlinear inverse scattering problem in the same way the linear equality does for the linear scattering problem. Notice that it includes the restriction that $|r(\omega)| < 1$. In fact, in [1] it is proved that any causal function for which the integral on the left is finite is in fact a reflection coefficient.

First and Last Reflections (Paley-Weiner Theorem)

The first arrival of a reflected pulse is the same for linear and nonlinear scattering — multiple reflections haven't had time to interfere. However, the nonlinear response to a pulse has no last arrival time. If the scattering is strong, this last reflection from the bottom can be completely obscured by multiple reflections at higher depths. However, if one computes the quantity $\frac{r(\omega)}{(1-|r(\omega)|^2)}$, then its inverse Fourier transform will have a last arrival time which is exactly the travel time depth to the bottom. Although we don't indicate the reasons here, this is actually a consequence of duality based on the nonlinear Plancherel equality above. The inverse Fourier transform of $\frac{1}{(1-|r(\omega)|^2)}$ has a last arrival time as well, which measures the width of the inhomogeneity in travel time.

The Nonlinear Sampling Theorem

Because of the paragraph above, the linear sampling theorem can be applied to $\frac{r(\omega)}{(1-|r(\omega)|^2)}$ and to $\frac{1}{(1-|r(\omega)|^2)}$, so that each can be calculated exactly from the sampled values or r at discrete frequencies. As r is just the ratio of these two, it too can be exactly calculated .

The Nonlinear Hilbert Transform

One way to see that the linear Hilbert transform is inappropriate for nonlinear scattering is to recall that the nonlinear reflection coefficient must always have modulus less than or equal to one. The linear Hilbert

transform does not preserve this property. It turns out that there is a nonlinear analog which does separate a reflection coefficient into causal and a-causal parts. Instead of decomposing into a sum, a reflection coefficient decomposes uniquely into a *star-product* of a causal and a-causal part. That is,

$$f = \frac{f_+ + f_-}{1 + \overline{f_-} f_+}$$

If we apply this decomposition to $e^{-2i\omega D} r(\omega)$, r_+ roughly represents the reflections generated below (travel time) depth D. This decomposition is the basic step in the implementation of the layer stripping algorithm described in [1].

This decomposition is *orthogonal* with respect to the *nonlinear norm* in the nonlinear Plancherel equality, i.e.

$$\int_{-\infty}^{\infty} \log(1 - |f|^2) d\omega = \int_{-\infty}^{\infty} \log(1 - |f^+|^2)|^2 d\omega + \int_{-\infty}^{\infty} \log(1 - |f^-|^2) d\omega$$

References

[1] A. Sylvester J., Winebrenner, D., and Gylys-Colwell, F. *Layer stripping for the Helmholtz equation* , SIAM Journal on Applied Mathematics , (1996)

INVERSE PROBLEMS FOR A PERTURBED DISSIPATIVE HALF-SPACE

Margaret Cheney and David Isaacson
Department of Mathematical Sciences
Rensselaer Polytechnic Institute
Troy, NY 12180

ABSTRACT

This paper addresses the scattering of acoustic and electromagnetic waves from a perturbed dissipative half-space. For simplicity, the perturbation is assumed to have compact support. Section 1 discusses the application that motivated this work and explains how the scalar model used here is related to Maxwell's equations. Section 2 introduces three formulations for direct and inverse problems for the half-space geometry. Two of these formulations relate to scattering problems, and the third to a boundary value problem. Section 3 shows how the scattering problems can be related to the boundary value problem. This shows that the three inverse problems are equivalent in a certain sense. In section 4, the boundary value problem is used to outline a simple way to formulate a multidimensional layer stripping procedure. This procedure is unstable and does not constitute a practical algorithm for solving the inverse problem. The paper concludes with three appendices, the first two of which carry out a careful construction of solutions of the direct problems and the third of which contains a discussion of some properties of the scattering operator.

Short title: Inverse problems for a half-space

PACS Classification numbers: 0340K, 0380, 4320, 4110H

1. INTRODUCTION

This work is motivated by the problems encountered in using radar as a geophysical probe. For these applications, the radar antenna is positioned above the earth, often on a satellite [E], an airplane, or a tall gantry. In many cases it is reasonable to approximate the earth as an infinite half-space $x_3 < 0$. The upper half-space is assumed to be composed of dry air, whose electromagnetic characteristics we assume to be those of free space (i.e., vacuum). Electromagnetic measurements are made in the upper half-space, and from these measurements one hopes to reconstruct the electromagnetic characteristics of the lower half-space.

In this paper we consider a simplified scalar model that includes not only the variable speed of wave propagation but also the dissipation. This model is also appropriate for acoustic wave propagation.

The propagation of electromagnetic waves is governed by Maxwell's equations, which we write in the form

$$\nabla \wedge E = i\omega\mu H \tag{1.1}$$

$$\nabla \wedge H = (\sigma - i\omega\epsilon)E. \tag{1.2}$$

Here E is the electric field, H the magnetic field, ϵ the electric permittivity, μ the magnetic permeability, and σ the conductivity. These equations are obtained from the time-dependent equations by assuming a time dependence of $e^{-i\omega t}$. We will take ω to be positive throughout.

In many cases of interest, the magnetic permeability is very close to the permeability of free space; accordingly we assume $\mu = \mu_0$. If we write out the six scalar equations of (1.1) and (1.2), and assume that ϵ, σ, E, and H are independent of one of the coordinates, say x_2, then we find that the six equations decouple into two sets of equations, one set for H_1, E_2, and H_3, and the other set for E_1, H_2, and E_3. These determine independent polarizations, the former called the Transverse Electric (TE) polarization and the latter called the Transverse Magnetic (TM) polarization [J].

The equations for the TE polarization reduce to

$$(\nabla^2 + \omega^2\mu_0\epsilon + i\omega\mu_0\sigma)E_2 = 0, \tag{1.3}$$

where the Laplacian is a two-dimensional one in the x_1 and x_3 variables. We assume that the upper half-space ($x_3 > 0$) is air, which we approximate by the same electromagnetic parameters as free space, namely $\epsilon = \epsilon_0$, $\sigma = 0$. We will write $k = \omega/c_0$, where $c_0 = (\mu_0\epsilon_0)^{-1/2}$ is the speed of light in free space. We will consider only k positive. In addition, we write $n^2 = \epsilon/\epsilon_0$ and $m = \sigma\sqrt{\mu_0/\epsilon_0}$. With this notation, (1.3) becomes

$$(\nabla^2 + k^2n^2 + ikm)E = 0, \tag{1.4}$$

where we have dropped the subscript on E.

In what follows, we will develop the theory for (1.3) and (1.4) when the Laplacian is a three-dimensional one; the theory for the two-dimensional case is similar. Both n^2 and m are assumed nonnegative. We assume that n^2 is identically one in the upper half-space, and in the lower half-space, n^2 differs from a positive constant n_-^2 only in a region of

compact support. Similarly m is identically zero in the upper half-space, and in the lower half-space differs from a positive constant m_- only in a region of compact support. These assumptions are meant to include the case of an ice floe in sea water. The parameter values for sea ice in the gigahertz range are between 3 and 4 for n^2 and around 6 m^{-1} for m. For sea water, n_-^2 is 3.37, and the value of m_- is around seven thousand m^{-1} [Ca]. We will write $x = (x_1, x_2, x_3) = (x', x_3)$.

The arguments given here would need to be modified in order to apply to cases when the background medium has more layers, and for the case when the perturbation extends into the upper half-space.

The theory of scattering from a half-space for (1.4) in the non-dissipative case ($m = 0$) has been developed in [Wi, DG, We, Xu]. The layered problem has been investigated by many investigators. In particular, the papers [Chj, M, KK] show that backscattered data from a single incident plane wave suffices to determine both n^2 and m only if n^2 and m have a jump discontinuity. An abstract formulation of scattering for dissipative hyperbolic systems has been given in [LP].

2. FORMULATION OF THREE INVERSE PROBLEMS

When a layered half-space is perturbed, some thought must be given to the formulation of the direct and inverse scattering problems. For the direct problem, one commonly-used approach [TKS] is to assume an incident plane wave and then use a half-space or layered-medium Green's function to set up an integral equation. The solution of this integral equation defines the scattering solution, whose far-field asymptotics are taken to be the scattering data. Inverse problems involve using this scattering data to determine perturbations in the medium.

One problem with this approach is that in practice, the incident field is never infinite in extent. This is unimportant if energy from infinity has no effect on the scattering, but for some layered medium problems this may not be the case. One can avoid this difficulty by multiplying the incident field by a cut-off function meant to model the antenna beam pattern, but the form of this cut-off function certainly does affect the scattering, and it is difficult to find a simple way to retain the information about the incident field in the far-field pattern. One approach to this is in [GX]. Below some other methods are suggested.

THE DIRECT AND INVERSE SCATTERING PROBLEM.

For any incident field, solutions to the direct scattering problem can be constructed in the usual way by converting the differential equation (1.4) to an integral equation that builds in the boundary conditions at infinity. The kernel of this integral equation is a Green's function for the unperturbed problem with outgoing boundary conditions. The details are given in Appendix 1.

To define scattering data, we consider the field E in the upper half-space. We define the scattering operator S to be the map from the downgoing part of the wavefield to the upgoing part. We construct an explicit representation $\hat{S}$ of this map in the Fourier transform domain. In particular, we use the fact that the medium parameters are known and constant in the upper half-space. For x_3 positive, one can therefore Fourier transform (1.4) in the x_1 and x_2 coordinates. The result is an ordinary differential equation whose

general solution for $x_3 > 0$ is

$$\hat{E}(\xi, x_3) = A(\xi)e^{i\lambda_+ x_3} + B(\xi)e^{-i\lambda_+ x_3}, \tag{2.1}$$

where $\lambda_+ = \sqrt{k^2 - |\xi|^2}$ and the hat denotes the two-dimensional Fourier transform

$$\hat{E}(\xi, x_3) = \int E(x', x_3)e^{-i\xi \cdot x'} dx', \tag{2.2}$$

x' denoting (x_1, x_2). When λ_+ is zero, the general solution corresponding to (2.1) is simply a constant. When $|\xi| < k$, the B term in (2.1) is a downgoing wave, whereas the A term is upgoing. The coefficient B thus determines an incident wave. This incident wave, together with continuity of E and its normal derivative at the interface $x_3 = 0$ and a radiation condition in the lower half-space, uniquely defines the scattered wave, which determines A. (See Appendix 1 for details.) Consequently, we can define $\hat{S}$ as the map from B to A. Thus $\hat{S}$ maps incident fields to scattered fields; knowledge of $\hat{S}$ is equivalent to knowledge of the scattered fields corresponding to all incident fields in some class. In particular, $\hat{S}$ can be considered as a map on the space $L^2(\mathbf{R}^2)$ of square-integrable functions. The operator S is then defined by $\widehat{Sf} = \hat{S}\hat{f}$.

If $|\xi| > k$, then the second term on the right side of (2.1) grows exponentially as x_3 becomes large. Because it is not physically reasonable for the incident wave in a scattering experiment to be exponentially large at infinity, in the scattering case we take B to be zero for $|\xi| > k$. For these values of ξ, the scattered wave also decays exponentially as x_3 goes to infinity; thus for a scattering experiment in which measurements are made in the far field, the relevant scattering operator is $P\hat{S}P$, where P denotes the projection operator of multiplication by the function that is one for $|\xi| \leq k$ and zero for $|\xi| > k$. Appendix 3 contains a proof that $P\hat{S}P$, as a map on a certain L^2 space, has norm less than one.

In the case when the incident wave is a plane wave independent of x_2, making an angle θ with the vertical, B is a delta function supported at $\xi = (k \sin\theta, 0)$. If the lower half-space varies only in the depth coordinate x_3, then $\hat{S} = P\hat{S}P$ is simply multiplication by the usual reflection coefficient [To, TKS]. Thus data from a single angle of incidence θ defines the action of $\hat{S}$ on $\delta(\xi - k(sin\theta, 0))$. As θ varies and the incident beam rotates around the vertical axis, the set $\{|\xi| < k\}$ is swept out. Thus knowledge of $\hat{S}$ incorporates knowledge of scattering for all angles of incidence.

This definition of scattering data differs from that in [TKS, Xu, We] in that no far-field asymptotic expansion is needed. The present definition may thus be useful in cases when measurements are made close to the surface. The present definition can handle any antenna beam pattern. However, this definition has the disadvantage that measurements are needed everywhere on a horizontal surface to completely determine $\hat{S}$. This makes it unsuitable for use with satellite-borne radar. If n^2 and m are assumed to depend only on x_3, then $\hat{S}$ can be determined for all ξ with magnitude less than k by measuring the reflection coefficient for all angles of incidence.

The inverse scattering problem is to determine n^2 and m in the lower half-space from knowledge of $\hat{S}$. In the three-dimensional case, if $\hat{S}$ is thought of as an integral operator mapping functions of two variables to functions of two variables, it is clear that $\hat{S}$ depends

on four variables. The unknowns n^2 and m depend on only three variables, so this inverse problem is overdetermined in the three-dimensional case. In the two-dimensional case, $\hat{S}$, n^2, and m are all functions of two variables.

THE POINT SOURCE INVERSE PROBLEM.

Another way to define scattering data is to assume that the incident field is due to a point source located either on the surface $x_3 = 0$ or in the upper half-space. In this case, (1.4) becomes

$$(\nabla^2 + k^2 n^2 + ikm)G(x, y) = -\delta(x - y), \tag{2.3}$$

where y is the location of the source. To define G uniquely, one needs an outgoing radiation condition at infinity. (See Appendix 1 for details.) Scattering data in this case can be taken to be knowledge of $G(x, y)$ for all x with $x_3 =$ constant and all y with $y_3 =$ constant.

The point source inverse problem is to determine n^2 and m in the lower half-space from the scattering data. In the three-dimensional case, the scattering data depend on four variables; in the two-dimensional case, on two.

THE INVERSE BOUNDARY VALUE PROBLEM.

A boundary value problem can be defined by

$$(\nabla^2 + k^2 n^2 + ikm)u = 0 \qquad \text{for } x_3 < 0 \tag{2.4}$$

$$u|_{x_3=0} = f, \tag{2.5}$$

together with an outgoing radiation condition in the lower half-space. If f is in the Sobolev space $H^{1/2}$ and $m > 0$, the Lax-Milgram theorem can be used [T] to show that the boundary value problem (2.4), (2.5) has a unique H^1 solution in the lower half-space. (A more explicit construction, involving Green's functions, is given in Appendix 2.) Thus the normal derivative $\partial u/\partial \nu$ on the surface $x_3 = 0$ is uniquely determined. The mapping from $H^{1/2}$ to $H^{-1/2}$

$$\Lambda : u|_{x_3=0} \mapsto \frac{\partial u}{\partial \nu}\Big|_{x_3=0} \tag{2.6}$$

is called the Dirichlet-to-Neumann map. Such maps have been used a great deal recently in the study of inverse problems [SU, SCII, Sy].

The inverse boundary value problem is to determine n^2 and m in the lower half-space from knowledge of Λ. In the three-dimensional case, Λ depends on four variables; in the two-dimensional case, it depends on two.

For some purposes, it is more convenient to work with the inverse of Λ; this inverse can be defined directly in a similar way.

3. CONNECTIONS BETWEEN THE SCATTERING PROBLEMS AND THE BOUNDARY VALUE PROBLEM

In this section, we discuss the sense in which the above inverse problems are equivalent.

The scattering problem and the boundary value problem. To see how the scattering problem is related to the boundary value problem, we recall that E and its normal

derivative are continuous at the interface $x_3 = 0$. In the upper half-space, however, E is given by (2.1). If $E = f$ on $x_3 = 0$, then we have

$$\hat{f} = (\hat{S} + I)B, \tag{3.1}$$

where I denotes the identity operator, and, differentiating (2.1) with respect to x_3,

$$\widehat{\Lambda f} = i\lambda_+(\hat{S} - I)B. \tag{3.2}$$

Eliminating B from (3.1) and (3.2) and defining $\hat{\Lambda}\hat{f} = \widehat{\Lambda f}$, we have

$$\hat{\Lambda}(\hat{S} + I) = i\lambda_+(\hat{S} - I). \tag{3.3}$$

This is an operator equation that holds on a certain function space that is discussed in Appendix 3.

To recover Λ from $\hat{S}$, it appears that we need only invert the operator $\hat{S} + I$ appearing on the left side of (3.3). To find the inverse, we solve the system (3.1), (3.2) of linear equations for B, obtaining $B = \frac{1}{2}(I - (i\lambda_+)^{-1}\hat{\Lambda})\hat{f}$. This shows that

$$(\hat{S} + I)^{-1} = \frac{1}{2}(I - (i\lambda_+)^{-1}\hat{\Lambda}). \tag{3.4}$$

This expression itself can be used to recover Λ from $\hat{S}$.

A similar argument shows that

$$(I - (i\lambda_+)^{-1}\hat{\Lambda})^{-1} = \frac{1}{2}(\hat{S} + I);$$

this expression can be used to obtain $\hat{S}$ from Λ. Note that this formula and (3.4) each contain terms with a singularity at $\lambda_+ = 0$. This is to be expected because $\hat{S}$ is not defined at $\lambda_+ = 0$.

The point source problem and the boundary value problem. To see how the point source problem is connected to the boundary value problem, we follow [N], where this connection was worked out for the case of a bounded body. We write $q = k^2n^2 + ikm$ and $q_0 = k^2$ so that the perturbed and unperturbed point source problems can be written

$$(\nabla^2 + q)G = -\delta \tag{3.5a}$$

and

$$(\nabla^2 + q_0)G_0 = -\delta, \tag{3.5b}$$

respectively. The scattering solutions G and G_0 satisfy radiation conditions at infinity.

We write Λ_q and Λ_0 for the Dirichlet-to-Neumann maps for the operators $\nabla^2 + q$ and $\nabla^2 + q_0$, respectively. We next use the scattering solutions G and G_0 to define two integral operators,

$$\Gamma f(x') = \lim_{y_3 \to 0^-} \int G((x', 0), (y', y_3))f(y')dy' \tag{3.6a}$$

and

$$\Gamma_0 f(x') = \lim_{y_3 \to 0^-} \int G_0((x',0),(y',y_3)) f(y') dy'. \tag{3.6b}$$

Theorem. G is related to Λ_q by the "boundary resolvent equation"

$$\Gamma - \Gamma_0 = \Gamma_0(\Lambda_q - \Lambda_0)\Gamma. \tag{3.7}$$

For the proof of this theorem, we need the following notation and lemma.

Given any f defined on the surface $x_3 = 0$, we use Γf to define the solutions u and v of the following boundary value problems:

$$(\nabla^2 + q)u = 0 \tag{3.8}$$

$$u|_{x_3=0} = \Gamma f \tag{3.9}$$

and

$$(\nabla^2 + q_0)v = 0 \tag{3.10}$$

$$v|_{x_3=0} = \Gamma f. \tag{3.11}$$

Both u and v are outgoing at infinity in the lower half-space.

Lemma. The solution u to (3.8), (3.9) is actually given by

$$u(x) = \int_{y_3=0} G(x,y) f(y) dy. \tag{3.12}$$

Proof. The function defined by equation (3.12) is an outgoing solution to (3.8), which on the boundary $x_3 = 0$ is equal to Γf.

QED

Proof of Theorem. Here we carry out the argument of [N] for the half-space case.

Relation (3.7) is obtained by using two different methods to compute the integral

$$I(x) = \int_{y_3<0} \left(G_0(x-y)\nabla^2(u-v)(y) - (u-v)(y)\nabla^2 G_0(x-y) \right) dy. \tag{3.13}$$

This integral is the limit as h goes to infinity of the integral I_h, in which the integrand is the same but the region of integration is C_h, a large cylindrical region with radius h^2 whose top is a disk in the plane $y_3 = 0$ and whose bottom is a disk in the plane $y_3 = -h$.

First, by Green's theorem,

$$I_h = \int_{\partial C_h} (G_0 \partial_\nu (u-v) - (u-v)\partial_\nu G_0) dA, \tag{3.14}$$

where ∂_ν denotes differentiation with respect to the outward unit normal and ∂C_h denotes the boundary of C_h. The boundary of C_h has three parts: the disk of radius h^2 on the surface $y_3 = 0$, the disk of radius h^2 on the surface $y_3 = -h$, and the side of the cylinder. We denote the corresponding integrals by I_h^1, I_h^2, and I_h^3, respectively.

First we consider I_h^1. Because $u = v$ on $y_3 = 0$, the second term of I_h^1 vanishes. Taking into account definitions of Γ_0 and the Dirichlet-to-Neumann maps, we find that for x with $x_3 = 0$, the first term is equal to $\Gamma_0(\Lambda_q u - \Lambda_0 v) = \Gamma_0(\Lambda_q - \Lambda_0)\Gamma f$.

The integrals I_h^2 and I_h^3 vanish as h goes to infinity because of the asymptotics of G_0. (See Lemma A1.2 in Appendix 1.)

Thus we have shown that

$$I|_{x_3=0} = \Gamma_0(\Lambda_q - \Lambda_0)\Gamma. \tag{3.15}$$

On the other hand, we can compute I without using Green's theorem. We see from (3.5), (3.8), and (3.10) that

$$I(x) = \int_{y_3<0} (G_0(q_0 v - qu) + (u - v)q_0 G_0)\, dy - (u - v)(x). \tag{3.16}$$

The terms in (3.16) involving $q_0 G_0 v$ cancel. Moreover, as x approaches the surface $x_3 = 0$, the term $(u - v)(x)$ vanishes. Thus (3.16) becomes

$$I = \int_{y_3<0} G_0(q - q_0)u dy. \tag{3.17}$$

The solution u of the boundary value problem, however, is given by $u = \int Gf$. Using this in (3.17), interchanging integrals, and using the resolvent equation $G - G_0 = \int G_0(q - q_0)G$, we obtain

$$I|_{x_3=0} = \int_{y_3=0} (G - G_0)f dy' = \Gamma f - \Gamma_0 f. \tag{3.18}$$

QED

In order to use (3.7) to obtain the Dirichlet-to-Neumann map from knowledge of the point source data, we need to be able to invert the integral operators Γ and Γ_0. This is discussed in Appendix 1.

Similarly, to obtain the point source data from the Dirichlet-to-Neumann map, one needs invertibility of the map $I - \Gamma_0(\Lambda_q - \Lambda_0) = \Gamma_0\Gamma^{-1}$, which follows from invertibility of Γ and Γ_0.

4. THE INVERSE BOUNDARY VALUE PROBLEM

Because the inverse scattering and inverse point source problems can be converted into the inverse boundary value problem, it is this problem we address here. We outline a possible approach, one based on the idea of layer-stripping. Roughly, the idea is first to use the measured data to find the medium parameters on the boundary, then to use that information to synthesize data on a nearby inner subsurface. The process is then repeated. In this manner, the medium is mathematically stripped away, layer by layer, and the medium parameters are found in the process.

For one-dimensional problems, this is an old idea; we make no attempt to trace its history here. For multidimensional problems it has not been so clear how to proceed;

various multidimensional layer-stripping algorithms have been suggested in [CK, SCII, W, Sm, DH, Y]. We outline here a simple way to formulate a multidimensional layer-stripping procedure.

Most of the layer-stripping schemes involve some sort of Riccati equation to remove a known layer of the medium. A Riccati equation, moreover, can be useful as a theoretical tool in working with inverse problems [LU]. As we see below, using the Dirichlet-to-Neumann map makes the appearance of a Riccati equation especially easy to understand.

Synthesizing the subsurface data. To synthesize the subsurface data, we obtain a differential equation for the boundary data in the depth variable. This requires that we extend the definition of the Dirichlet-to-Neumann map to any $z < 0$:

$$\Lambda(z)u|_{x_3=z} = \frac{\partial u}{\partial x_3}\Big|_{x_3=z}. \tag{4.1}$$

This map satisfies the following Riccati equation:

$$\frac{d\Lambda}{dz} = -\Lambda^2 - (\partial_{x_1}^2 + \partial_{x_2}^2) - q. \tag{4.2}$$

This equation is obtained by differentiating (4.1) with respect to z, using (2.4) to eliminate $\partial^2 u/\partial z^2$, and using (4.1) to eliminate $\partial u/\partial z$.

We note that equation (4.2) together with (3.3) or (3.4) can also be used to obtain a differential equation for the scattering operator $\hat{S}$. In the case when $d\hat{S}/dz$ commutes with $\hat{S}$ (such as in the layered case when $\hat{S}$ is a multiplication operator), this differential equation has the form

$$2i\lambda_+ \frac{d\hat{S}}{dz} = \lambda_+^2(\hat{S} - I)^2 + (\hat{S} + I)^2|\xi|^2 - (\hat{S} + I)^2 Q, \tag{4.3}$$

where $Q\hat{f} = \widehat{qf}$.

Finding the medium parameters on the boundary. To solve the inverse problem, we also need to use the boundary data to find the medium parameters on that same boundary. One approach to doing this is to use the idea of [KV, SCII] that is based on the principle that highly oscillatory boundary data corresponds to waves that penetrate only a short distance into the body. The difficulty with this approach, however, lies in the practical problem of creating such a field on the boundary: even in a nondissipative homogeneous medium such as air, fields with rapid spatial oscillations decay exponentially. This can be seen by writing a solution of

$$(\nabla^2 + q_0)u = 0 \tag{4.4}$$

as $u(x) = v(\xi, x_3)\exp(i\xi \cdot x')$, so that v satisfies the ordinary differential equation

$$(\partial_{x_3}^2 + q_0 - \xi^2)v = 0. \tag{4.5}$$

Even when q_0 is real, for large ξ the solution v decays exponentially. This suggests that conventional radar experiments, in which the antenna is far from the sample, could not supply highly oscillatory boundary data.

Accordingly, we consider an alternate method for obtaining the medium parameters on the boundary, namely geometrical optics [SU2]. This requires that we use either a range of temporal frequencies ω or that we do the experiments directly in the time domain.

The time-domain version of (1.3) is

$$(\nabla^2 - \mu_0\epsilon\partial_t^2 - \mu_0\sigma\partial_t)\mathcal{E} = 0. \tag{4.6}$$

The plan is to obtain a progressing wave expansion [CH] for (4.6); an expansion in functions of $\phi(x) - t$, however, results in successive coefficients differing in magnitude by the speed of light c_0. We therefore make the change of variables $\tau = c_0 t$, which converts (4.6) into

$$(\nabla^2 - n^2\partial_\tau^2 - m\partial_\tau)\mathcal{U} = 0. \tag{4.7}$$

We are interested in the small-time behavior of $\mathcal{U}$ in the neighborhood of an interface at $x_3 = 0$. For $x_3 > 0$, where $n = 1$, we expect that $\mathcal{U}$ is composed of an incident plane wave $\mathcal{U}^i = /delta(s^i(x) - \tau)$ plus a reflected wave, which we expand in the form

$$\mathcal{U}^r(s^r(x) - \tau) = A_0^r(x)\delta(s^r(x) - \tau) + A_1^r(x)H(s^r(x) - \tau) + \cdots. \tag{4.8}$$

Here s^i and s^r are the incident and reflected phases, δ denotes the Dirac delta function, and H denotes the Heaviside function that is one for positive arguments and zero for negative arguments. We take $\mathcal{U}^i$ to be a plane wave propagating in direction $\hat{e} = (e_1, e_2, e_3)$, which implies that $s^i = \hat{e} \cdot x$. Because we take this wave to be propagating in the downward direction, e_3 is negative. Just below the interface, for a short time we expect $\mathcal{U}$ to take the form of a transmitted wave, which we also expand as

$$\mathcal{U}^t(s^t(x) - \tau) = A_0^t(x)\delta(s^t(x) - \tau) + A_1^t(x)H(s^t(x) - \tau) + \cdots. \tag{4.9}$$

Here again s^t denotes the phase of the transmitted wave. On the interface $x_3 = 0$, $\mathcal{U}$ and its first x_3 derivative are continuous. Using these conditions at the interface and forcing $\mathcal{U}$ to satisfy (4.7) results in the eikonal equation

$$(\nabla s)^2 = n^2, \tag{4.10}$$

the interface conditions

$$s^i|_{x_3=0} = s^r|_{x_3=0} = s^t|_{x_3=0}, \tag{4.11}$$

and the transport equations

$$2\nabla s \cdot \nabla A_0 + A_0\nabla^2 s + mA_0 = 0 \tag{4.12}$$

$$2\nabla s \cdot \nabla A_1 + A_1\nabla^2 s + mA_1 + \nabla^2 A_0 = 0. \tag{4.13}$$

Here the absence of superscripts r or t indicates that the equation in question holds for both the reflected wave and transmitted wave. Solving these equations gives us

$$s^r(x) = e_1x_1 + e_2x_2 - e_3x_3 \tag{4.14}$$

$$\nabla s^t(x) = (e_1, e_2, -\sqrt{n^2 - e_1^2 - e_2^2}) \tag{4.15}$$

$$A_0^r|_{x_3=0} = \frac{1 + \sqrt{n^2 - e_1^2 - e_2^2}/e_3}{1 - \sqrt{n^2 - e_1^2 - e_2^2}/e_3} \tag{4.16}$$

$$A_0^t|_{x_3=0} = \frac{2}{1 - \sqrt{n^2 - e_1^2 - e_2^2}/e_3} \tag{4.17}$$

$$A_1^r|_{x_3=0} = \frac{\partial_{x_3} A_0^t - \partial_{x_3} A_0^r}{e_3 - \sqrt{n^2 - e_1^2 - e_2^2}}. \tag{4.18}$$

The quantities $\partial_{x_3} A_0^t$ and $\partial_{x_3} A_0^r$ appearing in (4.18) can be computed, with the help of the transport equation (4.12), to be

$$\partial_{x_3} A_0^r = (e_1 \partial_{x_1} + e_2 \partial_{x_2}) A_0^r / e_3 \tag{4.19}$$

and

$$\partial_{x_3} A_0^t = \frac{-1}{\sqrt{n^2 - e_1^2 - e_2^2}} \left((\partial_{x_3} \sqrt{n^2 - e_1^2 - e_2^2} A_0^t - m A_0^t)/2 - (e_1 \partial_{x_1} + e_2 \partial_{x_2}) A_0^t \right). \tag{4.20}$$

To obtain the medium parameters n^2 and m at a point x^0 on the surface from scattering data, we send in an incident wave that is planar in a neighborhood of x^0. We then measure the scattered field at all points on a plane $x_3 =$ constant. From this information, the short-time scattered field can be inferred in a neighborhood of x^0. The value of A_0^r at x^0 tells us, via (4.16), what the value of n^2 is at x^0. In this manner, we obtain n^2 for every point on the surface; this allows us to compute, at every point, not only A_0^t from (4.17) but also the x_1- and x_2-derivatives appearing on the right side of (4.19) and (4.20). Once these are known, $\partial_{x_3} A_0^r$ can be computed and used in the right side of (4.18); since A_1^r is also known, from (4.18) we can obtain $\partial_{x_3} A_0^t$. All quantities in (4.20) are thus known except for m and $\partial_{x_3} n^2$; evidently both quantities cannot be found from a single angle of incidence. Use of the scattered field from two angles of incidence allows us to find both m and $\partial_{x_3} n^2$.

Let us consider the layer-stripping algorithm in the case when a complete set of incident fields are used and measurements of the corresponding scattered fields are made on a plane. We assume measurements are made at N frequencies. For experiments with stepped-frequency radar, for example, N can range from 51 to 801 [Jz]. The algorithm proceeds as follows.

Step 1. From the measurements at frequencies $k_0, k_1, \ldots, k_N$, construct an approximation to each scattering operator $S(k_n)$, $n = 0, 1, \ldots, N$. In practice, one would represent $S(k_n)$ by its matrix with respect to some basis. Such a basis could perhaps be constructed from antenna beam patterns for a large number of incident angles. The operator $\hat{S}$, for example, is the representation of S in a Fourier basis.

Step 2. For each of at least two incident directions $\hat{e}_j$, $j = 1, 2, \ldots, J$, choose an incident field that looks like $\exp(ik_n \hat{e}_j \cdot x)$ in the neighborhood of some point x_0 on the surface. Apply $S(k_n)$ to these incident fields to obtain the scattered field $E_{sc}(k_n, x)$.

Step 3. Fourier transform into the time domain to obtain $U^r(\tau, x)$. In practice, one can do this by first synthesizing an approximate delta function in the form

$$\delta(\tau) \approx \sum_{n=1}^{N} w_n e^{ik_n\tau}, \tag{4.21}$$

where the w_n are, for example, Hamming weights [OS]. Then the field

$$U^r(\tau, x) \approx \sum_{n=1}^{N} E_{sc}(k_n, x) w_n e^{ik_n\tau} \tag{4.22}$$

is locally the response to the incident approximate delta function (4.21).

Step 4. Extract the coefficients $A_0^r(x_0, \hat{e}_j)$ and $A_1^r(x_0, \hat{e}_j)$. This can be done, for example, by the least squares minimization

$$\min_{A_0^r, A_1^r} \int_0^T |U^r(\tau, x_0) - A_0^r(x_0, \hat{e}_j)\delta(s^r(x_0) - \tau) - A_1^r(x_0, \hat{e}_j)H(s^r(x_0) - \tau)|^2 d\tau, \tag{4.23}$$

where for U^r one uses (4.22), for s^r one uses (4.14), for δ one uses (4.21), and for the Heaviside function H one uses

$$H(\tau) \approx \sum_{n=1}^{N-} \frac{w_n}{ik_n} e^{ik_n\tau}. \tag{4.24}$$

Step 5. From $A_0^r(x_0, \hat{e}_j)$ and $A_1^r(x_0, \hat{e}_j)$ for $j = 1, 2, \ldots, J$, determine $n^2(x_0)$, $m(x_0)$, and $\partial_{x_3} n^2(x_0)$. If $J > 2$ so that the system is overdetermined, one can use least squares to find the best fit.

Step 6. Repeat steps 2) through 5) for a large number of points x_0 on the surface.

Step 7. For each k_n, synthesize the subsurface data either from a Riccati equation for $S(k_n)$ such as (4.3), or use (3.3) or (3.4) to convert $S(k_n)$ to $\Lambda(k_n)$, use (4.2), and convert back to $S(k_n)$ with (3.3) or (3.4). Again, in practice, the operators $S(k_n)$ and $\Lambda(k_n)$ would be represented as matrices with respect to some basis, and equations (3.3), (3.4), and (4.2) would be approximated as matrix equations.

Step 8. Repeat, starting with step 2).

Although the above algorithm may seem ready to implement, it cannot be used in its present form because it is UNSTABLE. This is partly because of the multiplication by $|\xi|^2$ on the right side of (4.3) or equivalently, because of the x_1 and x_2 derivatives appearing on the right side of (4.2). This is similar to the situation in [YL]; this type of instability can be overcome to some extent by smoothing in the x_1 and x_2 directions, as discussed in [C]. Even when the problem is independent of x_1 and x_2, however, one expects the methods to be unstable, due to the fact that only a little of the energy put into the system on the top can propagate to great depths. Thus one expects the boundary data and scattering data to contain little information about the deeper regions. There may be methods, such as those of [SCII, SWG], for overcoming this instability to some extent. Finally, there may

be difficulties connected with using bandlimiting data as described in [PSS]. Investigation of methods for overcoming the instability is left for the future.

APPENDIX 1. CONSTRUCTION OF SCATTERING SOLUTIONS

In this Appendix, we will construct outgoing solutions of (1.4) and (2.3). We do this with the help of the unperturbed Green's function.

Construction of the scattering Green's function. The unperturbed scattering Green's function $G_0(x,y) = G_0(x_1 - y_1, x_2 - y_2, x_3, y_3)$ satisfies

$$(\nabla^2 + k^2 n_0^2(x_3) + ikm_0(x_3))G_0(x,y) = -\delta(x-y) \tag{A1.1}$$

and is outgoing at infinity. Here $n_0^2 = 1$ and $m_0 = 0$ for $x_3 > 0$, and $n_0^2 = n_-^2$ and $m_0 = m_-$ for $x_3 < 0$. Equation (A1.1) can be Fourier transformed in the x_1 and x_2 variables, which yields

$$(\partial_{x_3}^2 + \lambda_0^2)\hat{G}_0(\xi, x_3, y_3) = -\delta(x_3 - y_3), \tag{A1.2}$$

where we have written $\lambda_0^2 = -|\xi|^2 + k^2 n_0^2 + ikm_0$. The general solution of (A1.2) is

$$\hat{G}_0^+(\xi, x_3, y_3) = A^+(\xi)e^{i\lambda_+ x_3} + B^+(\xi)e^{-i\lambda_+ x_3} \tag{A1.3}$$

for $x_3 > 0$ and

$$\hat{G}_0^-(\xi, x_3, y_3) = A^-(\xi)e^{i\lambda_- x_3} + B^-(\xi)e^{-i\lambda_- x_3}. \tag{A1.4}$$

for $x_3 < 0$. The coefficients $A^\pm$ and $B^\pm$, however, depend on whether y_3 is positive or negative and are different in the regions separated by the origin and the point $x_3 = y_3$. When x_3 is bigger than both 0 and y_3, the condition that $\hat{G}_0$ be upgoing implies that B^+ is zero; when x_3 is less than both 0 and y_3, the condition that $\hat{G}_0$ be downgoing implies that A^- is zero. $\hat{G}_0$ and its x_3 derivative are continuous except at $x_3 = y_3$, where $\hat{G}_0$ is continuous but its x_3 derivative jumps by one. Solving for the As and Bs in both cases results in

$$\hat{G}_0(\xi, x_3, y_3) = \frac{i}{2\lambda_+}\begin{cases} R(\lambda_+, \lambda_-)e^{i\lambda_+(x_3+y_3)} + e^{i\lambda_+|x_3-y_3|}, & \text{for } x_3 > 0 \\ T(\lambda_+, \lambda_-)e^{i\lambda_+ y_3}e^{-i\lambda_- x_3}, & \text{for } x_3 < 0 \end{cases} \tag{A1.5}$$

for the case when $y_3 > 0$ and

$$\hat{G}_0(\xi, x_3, y_3) = \frac{i}{2\lambda_-}\begin{cases} T(\lambda_-, \lambda_+)e^{-i\lambda_- y_3}e^{i\lambda_+ x_3}, & \text{for } x_3 > 0 \\ e^{i\lambda_-|x_3-y_3|} + R(\lambda_-, \lambda_+)e^{-i\lambda_-(x_3+y_3)}, & \text{for } x_3 < 0 \end{cases} \tag{A1.6}$$

for the case when $y_3 < 0$, where

$$T(\lambda_1, \lambda_2) = \frac{2\lambda_2}{\lambda_1 + \lambda_2} \tag{A1.7}$$

and

$$R(\lambda_1, \lambda_2) = \frac{\lambda_2 - \lambda_1}{\lambda_1 + \lambda_2}. \tag{A1.8}$$

Note that since the imaginary parts of λ_+ and λ_- are nonnegative, the exponents in (A1.5) and (A1.6) are decaying. The Green's function itself is obtained from its Fourier transform by

$$G_0(x,y) = \frac{1}{(2\pi)^2} \int e^{i(x'-y')\cdot\xi} \hat{G}_0(\xi, x_3, y_3) d\xi.$$

Construction of scattering solutions. For an incident wave E^0, a scattering solution E of (1.4) can be defined as the solution to the integral equation

$$E(x) = E^0(x) + \int G_0(x,y)V(y)E(y)dy, \qquad (A1.9)$$

where we have written $V(y) = k^2(n^2(y) - n_-^2) + ik(m(y) - m_-)$.

Similarly, for (2.3), the scattering solution $G(x,y)$ at x due to a point source at y should satisfy the resolvent equation

$$G(x,y) = G_0(x,y) + \int G_0(x,z)V(z)G(z,y)dz. \qquad (A1.10a)$$

The Green's function G, however, has a singularity at $x = y$, which causes some technical problems. We therefore write the resolvent equation in terms of the scattered wave G_{sc}, which is defined by $G = G_0 + G_{sc}$:

$$G_{sc} = \int G_0 V G_0 + \int G_0 V G_{sc}. \qquad (A1.10b)$$

In order to use (A1.9) to define E and (A1.10b) to define G, we must show that both equations have unique solutions.

In order to do this, we will need the following spaces that are weighted in the x_3 variable.

$$L^{2,s}(\mathbf{R}^3) = \{u : (1 + |x_3|^2)^{s/2} u \in L^2(\mathbf{R}^3)\}$$

$$H^{1,s} = \{u : D^\alpha u \in L^{2,s}, |\alpha| \le 1\},$$

where we use the multi-index notation $\alpha = (\alpha_1, \alpha_2, \alpha_3)$, $|\alpha| = |\alpha_1| + |\alpha_2| + |\alpha_3|$, and $D^\alpha = (\partial/\partial x_1)^{\alpha_1}(\partial/\partial x_2)^{\alpha_2}(\partial/\partial x_3)^{\alpha_3}$. Here L^2 denotes the space of square-integrable functions.

Proposition A1.1. If V is a bounded function of compact support, the operator G_0V is compact in $H^{1,-s}(\mathbf{R}^3)$ for any $s > 1/2$.

Proof. Because we are making the (unnecessary but simplifying) assumption that V has compact support in the lower half-space, we write G_0V as $G_0\chi V$, where χ is the function that is one on the support of V and zero everywhere else. We then follow the ideas of [Ag]: first we show that multiplication by V is a compact operator mapping $H^{1,-s}$ into $L^{2,s}$; then we show that the operator $G_0\chi$ is a bounded operator mapping $L^{2,s}$ into $H^{1,-s}$. Hence the product operator $G_0\chi V = G_0V$ is a compact operator on $H^{1,-s}$.

Multiplication by V is a compact operator from $H^{1,-s}$ to $L^{2,s}$ under much more general conditions (see [S]). Here, however, we can simply rely on the Sobolev imbedding theorem [Ad, p. 144].

To show that $G_0\chi$ is a bounded mapping from $L^{2,s}$ into $H^{1,-s}$, we follow the outline of the argument in [RS4]. We write $\phi = G_0\chi\psi$, which, when Fourier transformed, reads

$$\hat{\phi}(\xi, x_3) = \frac{1}{2\lambda_-} \begin{cases} \int_{-h}^{0} (R(\lambda_-, \lambda_+) e^{-i\lambda_-(x_3+y_3)} + e^{i\lambda_-|x_3-y_3|}) \hat{\psi}(\xi, y_3) dy_3, & \text{for } x_3 < 0 \\ \int_{-h}^{0} T(\lambda_-, \lambda_+) e^{-i\lambda_- y_3} e^{i\lambda_+ x_3} \hat{\psi}(\xi, y_3) dy_3, & \text{for } x_3 > 0 \end{cases} \tag{A1.11}$$

where h is chosen so that the support of V is in the region $y_3 > -h$.

Because the exponentials on the right side are decaying, from (A1.11) we can draw the conclusion

$$|\hat{\phi}(\xi, x_3)| \leq \frac{c}{(1+|\xi|^2)^{1/2}} \|\hat{\psi}(\xi, \cdot)\|_{L^1}, \tag{A1.12}$$

where L^1 refers to $L^1(-h, 0)$. Similarly, if we differentiate ϕ, we obtain

$$|\widehat{D^\alpha \phi}(\xi, x_3)| \leq c \|\hat{\psi}(\xi, \cdot)\|_{L^1} \tag{A1.13}$$

for any $|\alpha| \leq 1$.

Next we relate each side of (A1.13) to a weighted norm in the x_3 variable. First, the L^1 norm on the right side can be bounded above by

$$\int (1+|x_3|^2)^{-s/2} (1+|x_3|^2)^{s/2} |\hat{\psi}(\xi, x_3)| dx_3 \leq c \|\hat{\psi}(\xi, \cdot)\|_{L^{2,s}}. \tag{A1.14}$$

The left side of (A1.13), on the other hand, can be related to a weighted norm by

$$\|\widehat{D^\alpha \phi}(\xi, \cdot)\|^2_{L^{2,-s}} = \int (1+|x_3|^2)^{-s} |\widehat{D^\alpha \phi}(\xi, x_3)|^2 dx_3 \leq \|\widehat{D^\alpha \phi}(\xi, \cdot)\|^2_{L^\infty} \int (1+|x_3|^2)^{-s} dx_3. \tag{A1.15}$$

For $s > 1/2$, the rightmost integral of (A1.15) converges to a positive real number; thus we can rewrite (A1.15) as

$$\|\widehat{D^\alpha \phi}(\xi, \cdot)\|^2_{L^{2,-s}} \leq c \|\widehat{D^\alpha \phi}(\xi, \cdot)\|^2_{L^\infty}. \tag{A1.16}$$

Using (A1.14) and (A1.16) in (A1.13), we obtain

$$\|\widehat{D^\alpha \phi}(\xi, \cdot)\|^2_{L^{2,-s}} \leq c \|\hat{\psi}(\xi, \cdot)\|^2_{L^{2,s}}. \tag{A1.17}$$

Next we convert (A1.17), which involves only one-dimensional weighted norms, to a similar statement about three-dimensional weighted norms. We do this by integrating both sides with respect to x_1 and x_2, and using the Plancherel theorem to obtain

$$\int |D^\alpha \phi(x)|^2 (1+|x_3|^2)^{-s} dx \leq c \int |\psi(x)|^2 (1+|x_3|^2)^s dx. \tag{A1.18}$$

QED

Because the medium in the lower half-space is dissipative, waves there must decay exponentially as they travel in the medium. We can see this as follows.

Lemma A1.2. If V has compact support, then in any finite-thickness slice of the lower half-plane $\{x : x_3^- < x_3 < x_3^+ < 0\}$, any solution u of (1.4) that is in $H^{1,-s}$ decays exponentially at infinity.

Proof. We consider a rectangular region along the x_1 axis outside the support of V, namely $\{x : x_1^- < x_1, 0 < x_2 < x_2^+, x_3^- < x_3 < x_3^+ < 0\}$. In this region, we write u in a Fourier series

$$u(x) = \sum_{l,p} \tilde{u}_{l,p}(x_1) e^{il\pi x_2/\Delta x_2} e^{ip\pi x_3/\Delta x_3}, \qquad (A1.20)$$

where we have written $\Delta x_2 = x_2^+ - x_2^-$ and $\Delta x_3 = x_3^+ - x_3^-$. Since u is not periodic in the x_2 or x_3 variables, this expression will not coincide with u outside the box, but this does not matter for the present purpose.

Because u satisfies the unperturbed wave equation (1.4) in the box, the Fourier coefficient $\tilde{u}_{l,p}$ satisfies the ordinary differential equation

$$(\partial_{x_1}^2 - (\frac{l\pi}{\Delta x_2})^2 - (\frac{p\pi}{\Delta x_3})^2 + k^2 n_-^2 + ikm_-)\tilde{u}_{l,p} = 0, \qquad (A1.21)$$

whose solutions are linear combinations of exponentials that either grow or decay for large x_1. Because u is in $H^{1,-s}$, the coefficients of the growing exponentials must be zero. The solution u can therefore be written

$$u(x) = \sum_{l,p} \tilde{u}_{l,p}(x_1^-) \exp\left(ix_1\sqrt{k^2 n_-^2 + ikm_- - (\frac{l\pi}{\Delta x_2})^2 - (\frac{p\pi}{\Delta x_3})^2}\right) e^{il\pi x_2/\Delta x_2} e^{ip\pi x_3/\Delta x_3}. \qquad (A1.22)$$

To show that the right side decays exponentially in the x_1 variable, we note that the imaginary part of the square root is bounded below by $m_-/2$. A factor of $e^{-m_- x_1/4}$ can thus be pulled out of each term, and the remaining series converges.

Because (1.4) is isotropic outside the support of V, any direction can be chosen as the x_1 direction.

QED

Proposition A1.3. Suppose V is a bounded function of compact support, and assume m is strictly positive in the lower half-space. Then if E^0 is in $H^{1,-s}$, (A1.9) has a unique solution in $H^{1,-s}$ for $s > 1/2$. Similarly, (A1.10b) has a unique solution in the same space.

Proof. For (A1.10b), we check that the inhomogeneous term $G_0 V G_0$ is in $H^{1,-s}$ for $s > 1/2$. The Green's function G_0, being a fundamental solution of the Helmholtz equation, has no singularities worse than the $1/|x-y|$ singularity for x near y. This singularity, however, is square-integrable in three dimensions. The product VG_0 is therefore in $L^{2,s}$, so by Proposition A1.1, $G_0 V G_0$ is in $H^{1,-s}$.

By the Fredholm theorem, to show that (A1.9) and (A1.10b) each have unique solutions, we need to show that the homogeneous equation

$$\psi(x) = \int G_0(x,y) V(y) \psi(y) dy \qquad (A1.23)$$

has only the trivial solution. A solution to (A1.23), however, corresponds to a solution of (1.4) with no sources and no incoming wave. To show that such a solution must be identically zero, we use an energy identity, which we obtain by multiplying (1.4) by the complex conjugate $\bar{E}$ and integrating over a cylindrical region Ω_ρ of radius ρ, whose top is a disk in the $x_3 = x_3^+$ plane and whose bottom is a disk in the plane $x_3 = -h$. Here h is chosen so that the support of the perturbation V is contained between the planes $x_3 = -h$ and $x_3 = 0$. After an application of the divergence theorem, we have

$$\int_{\Omega_\rho} (|\nabla E|^2 - k^2 n^2 |E|^2 - ikm|E|^2) = \int_{\partial\Omega_\rho} \bar{E} \frac{\partial E}{\partial \nu}. \qquad (A1.24)$$

For E in (A1.24) we substitute a solution ψ of (A1.23), written in the form

$$\psi(x) = \frac{1}{(2\pi)^2} \int \hat{\psi}(\xi, x_3) e^{ix' \cdot \xi} d\xi. \qquad (A1.25)$$

¿From (A1.6) we see that for $x_3 > 0$,

$$\hat{\psi}(\xi, x_3) = A(\xi) e^{i\lambda_+ x_3}$$

and for $x_3 < -h$,

$$\hat{\psi}(\xi, x_3) = B(\xi) e^{-i\lambda_- x_3}$$

for some coefficients A and B. We use these expansions in (A1.25), which is then substituted into the integrals over the top and bottom of the cylinder on the right side of (A1.24). We then let ρ go to infinity; the integrals over the vertical sides of the cylinder go to zero as ρ goes to infinity by Lemma A1.2. Finally, in the integrals over the top and bottom, we perform the x' integration. The result is

$$\int_{\Omega_\infty} (|\nabla \psi|^2 - k^2 n^2 |\psi|^2 - ikm|\psi|^2) = i \int (|A(\xi)|^2 \lambda_+ e^{-2\mathrm{Im}\lambda_+ x_3^+} + |B(\xi)|^2 \lambda_- e^{-2h\lambda_-}) d\xi \qquad (A1.26)$$

If ψ is nonzero and k is positive, the left side of (A1.26) has negative imaginary part, whereas the imaginary part of the right side is nonnegative. This shows that ψ is identically zero for k positive.

QED

If m were identically zero in some region in the lower half-space, the above argument does not rule out the possibility that ψ might be nonzero there. This could happen, for example, if $k^2 n^2$ were equal to a constant that happened to be a Dirichlet eigenvalue for the region in which m is identically zero. In this case, there could exist a nonzero solution in that region with zero boundary values. This possibility can be ruled out by assuming smoothness of n^2 and m, so that the unique continuation principle of [RS4] holds.

Next we investigate the invertibility of the integral operators defined in (3.6). For this, we need to define the following subspaces of $L^{2,s}$ and H^s:

$$\tilde{L}_k^{2,s} = \{\sqrt{k^2 - |\cdot|^2} f : (1 + |\cdot|^2)^{(s+1)/2} f(\cdot) \in L^2\}$$

and

$$\tilde{H}_k^s = \{f : \hat{f} \in \tilde{L}_k^{2,s}\}.$$

Proposition A1.4. If m is strictly positive in the lower half-space, then the integral operators Γ and Γ_0 are both invertible operators from $H^{-1/2}(\mathbf{R}^2)$ to $\tilde{H}_k^{1/2}(\mathbf{R}^2)$.

Proof. The result for Γ_0 is clear from expression (A1.6) with $x_3 = y_3 = 0$.

To show that Γ is invertible, we write (following [N])

$$\Gamma = \Gamma_0 \left(I + \Gamma_0^{-1}(\Gamma - \Gamma_0)\right),$$

so that invertibility of Γ follows from invertibility of $I + \Gamma_0^{-1}(\Gamma - \Gamma_0)$. The difference $\Gamma - \Gamma_0$ is a compact operator on $H^{1/2}$ because it can be written in terms of the composition of the compact operator $G_0 V$ with G (see Proposition A1.1). Since $\Gamma_0^{-1}(\Gamma - \Gamma_0)$ is compact, invertibility of $I + \Gamma_0^{-1}(\Gamma - \Gamma_0)$ follows from its injectivity, which in turn follows from the injectivity of Γ.

To see that Γ is injective, we write $u(x) = \int_{y_3=0} G(x, y')f(y')dy'$, where we assume $u(x) = 0$ for $x_3 = 0$. The Lemma of section 3 shows that u satisfies (3.8) with zero boundary values; the argument of Proposition A2.2 shows that u must be identically zero in the lower half-space. We next multiply (A1.10a) by f, integrate with respect to y', and let y_3 and x_3 approach zero through negative values. We obtain

$$u(x') - \Gamma_0 f(x') = \int G_0((x', 0), z)V(z)u(z)dz,$$

which, since u is identically zero, reduces to $\Gamma_0 f = 0$. The injectivity of Γ_0, however, is clear from (A1.6).

QED

APPENDIX 2. CONSTRUCTION OF THE OUTGOING SOLUTION TO THE BOUNDARY VALUE PROBLEM

In this appendix, we will construct an outgoing solution to the boundary value problem with the help of the outgoing Green's function that is zero on the boundary $x_3 = 0$. This Green's function is then used to convert the boundary value problem to an integral equation, which will be shown to have a unique solution.

The outgoing Dirichlet Green's function. In the lower half-space $\mathbf{R}^3_-$, the Green's function $g(x, y) = g(x_1 - y_1, x_2 - y_2, x_3, y_3)$ satisfies an outgoing radiation condition and the boundary value problem

$$(\nabla^2 + k^2 n_-^2 + ikm_-)g(x, y) = -\delta(x - y), \qquad (A2.1)$$

$$g(x, y)|_{x_3=0} = 0. \qquad (A2.2)$$

This Green's function can be constructed by two methods. The first method is that used in Appendix 1; in particular, equation (A2.1) can be Fourier transformed in the x_1 and x_2 variables, which yields

$$(\partial_{x_3}^2 + \lambda_-^2)\hat{g}(\xi, x_3, y_3) = -\delta(x_3 - y_3), \qquad (A2.3)$$

where we have written $\lambda_-^2 = -|\xi|^2 + k^2 n_-^2 + ikm_-$. For $y_3 < x_3 < 0$, the general solution of (A2.3) is

$$\hat{g}^+(\xi, x_3, y_3) = A^+(\xi) e^{i\lambda_- x_3} + B^+(\xi) e^{-i\lambda_- x_3}; \tag{A2.4}$$

for $x_3 < y_3 < 0$, it is

$$\hat{g}^-(\xi, x_3, y_3) = A^-(\xi) e^{i\lambda_- x_3} + B^-(\xi) e^{-i\lambda_- x_3}. \tag{A2.5}$$

The condition that $\hat{g}$ be downgoing as $x_3 \to -\infty$ implies that $A^- = 0$; the boundary condition (A2.2) implies that $A^+ + B^+ = 0$; $\hat{g}$ is continuous at $x_3 = y_3$ but the derivative $\partial\hat{g}/\partial x_3$ jumps by 1. Solving for the As and Bs, we obtain

$$\hat{g}(\xi, x_3, y_3) = \frac{i}{2\lambda_-}\left(e^{i\lambda_- |x_3 - y_3|} - e^{-i\lambda_-(x_3 + y_3)}\right). \tag{A2.6}$$

Written in this form, it is clear that when λ_- has positive imaginary part, $\hat{g}(\xi, x_3, y_3)$ decays exponentially as $x_3 \to -\infty$. Moreover, for fixed $x_3 \neq y_3$, $\hat{g}$ decays exponentially as $|\xi| \to \infty$. This Fourier transformed Green's function can also be written as

$$\hat{g}(\xi, x_3, y_3) = \frac{-1}{\lambda_-} \begin{cases} e^{-i\lambda_- y_3} \sin \lambda_- x_3, & \text{for } y_3 \leq x_3 \leq 0; \\ e^{-i\lambda_- x_3} \sin \lambda_- y_3, & \text{for } x_3 \leq y_3 \leq 0. \end{cases} \tag{A2.7}$$

The Green's function itself is then

$$g(x, y) = \frac{1}{(2\pi)^2} \int e^{i(x' - y')\cdot\xi} \hat{g}(\xi, x_3, y_3) d\xi. \tag{A2.8}$$

This same Green's function can also be constructed by the method of images. For a point $y = (y_1, y_2, y_3)$ in the lower half-space, the corresponding image point is $\tilde{y} = (y_1, y_2, -y_3)$. Then we can write the Green's function as

$$g(x, y) = \frac{1}{4\pi}\left(\frac{e^{i(k^2 n_-^2 + ikm_-)^{1/2}|x-y|}}{|x - y|} - \frac{e^{i(k^2 n_-^2 + ikm_-)^{1/2}|x-\tilde{y}|}}{|x - \tilde{y}|}\right). \tag{A2.9}$$

It is clear from this expression that g decays exponentially at infinity.

To see that these two representations are the same, we recall that the free space Green's function can be Fourier transformed as

$$\frac{e^{i\gamma|x|}}{4\pi|x|} = \frac{1}{(2\pi)^3} \int \frac{e^{ix\cdot\zeta}}{|\zeta|^2 - |\gamma|^2} d\zeta. \tag{A2.10}$$

In this Fourier transform integral, we can do the ζ_3 integral first; it is

$$\frac{1}{2\pi} \int \frac{e^{ix_3\zeta_3}}{\zeta_3^2 - (\gamma^2 - |\xi|^2)} d\zeta_3, \tag{A2.11}$$

where we have written $\xi = (\zeta_1, \zeta_2)$. This one-dimensional integral can be done by contour integration; it is equal to

$$\frac{i \exp(i|x_3|\sqrt{\gamma^2 - |\xi|^2})}{2\sqrt{\gamma^2 - |\xi|^2}}. \qquad (A2.12)$$

To relate (A2.12) to (A2.6), we let $\gamma = (k^2 n_-^2 + ikm_-)^{1/2}$; we then substitute $x_3 - \tilde{y}_3$ for x_3 in (A2.12) and subtract the resulting expression from the one obtained by substituting $x_3 - y_3$ for x_3.

Construction of the outgoing solution to the boundary value problem. We construct the outgoing solution to the boundary value problem as the solution to an integral equation. This integral equation is obtained by multiplying (2.4) by g and (A2.1) by u, subtracting the resulting equations, and applying Green's theorem. After using the boundary conditions at infinity and (2.5), we obtain

$$u(x) = -\int_{y_3<0} g(x,y)V(y)u(y)dy - \int_{y_3=0} f(y)\frac{\partial g(x,y)}{\partial y_3}dy, \qquad (A2.13)$$

where we have written $V(y) = k^2(n^2(y) - n_-^2) + ik(m(y) - m_-)$. We can write this equation in more compact notation by writing the first term on the right-hand side in operator notation as gVu. This equation can be used to define u.

First, we show that a solution u of (A2.13) has the desired properties. It is clearly outgoing. To see that u satisfies the correct boundary condition, we evaluate (A2.13) at $x_3 = 0$. From (A2.2) or (A2.7) we see that the Green's function is zero when $x_3 = 0$. Thus the entire contribution to u comes from the second term on the right side of (A2.13). Again from (A2.7) and (A2.8) we see that the normal derivative of g on the surface $y_3 = 0$ is

$$\left.\frac{\partial g(x,y)}{\partial y_3}\right|_{x_3=0} = \frac{-1}{(2\pi)^2}\int e^{i(x'-y')\cdot\xi} e^{-i\lambda_- x_3} d\xi, \qquad (A2.14)$$

which, as $x_3 \to 0$, becomes a negative delta function supported at $x' = y'$.

QED

Next we show that equation (A2.13) has a unique solution in H^1.

Proposition A2.1. If V is a bounded function of compact support, the operator gV is compact in $H^1(\mathbf{R}^3_-)$.

Proof. We follow the ideas of [Ag]: first we show that multiplication by V is a compact operator mapping H^1 into L^2; then we show that the operator g is a bounded operator mapping L^2 into H^1. Hence the product operator gV is a compact operator on H^1.

To see that multiplication by V is a compact mapping from H^1 into L^2, we simply invoke the Sobolev imbedding theorem [Ad].

To show that the operator g maps L^2 into H^1, we begin by writing $\phi = g\psi$. The two-dimensional Fourier transform of this is $\hat{\phi} = \hat{g}\hat{\psi}$. From (A2.6) we see that $\hat{g}$ is bounded and decays for large $|\xi|$ like $1/|\xi|$; this shows immediately (with the help of the Plancherel theorem) that $\|\phi\|_{L^2(\mathbf{R}^3_-)} \le c\|\psi\|_{L^2(\mathbf{R}^3_-)}$ and $\|\partial\phi/\partial x_i\|_{L^2(\mathbf{R}^3_-)} \le c\|\psi\|_{L^2(\mathbf{R}^3_-)}$ for $i = 1, 2$.

To show the same thing for the x_3 derivative, we write $\hat{g} = i(2\lambda)^{-1}(h_1 - h_2)$, where $h_1(\xi, x_3, y_3) = \exp(i\lambda_-|x_3 - y_3|)$ and $h_2(\xi, x_3, y_3) = \exp(-i\lambda_-(x_3 + y_3))$. With this notation, we have $\hat{\phi} = \hat{\phi}_1 + \hat{\phi}_2$, where

$$\hat{\phi}_1(\xi, x_3) = \frac{i}{2\lambda_-} \int_{-\infty}^{0} h_1(\xi, x_3, y_3)\hat{\psi}(\xi, y_3)dy_3 \qquad (A2.15)$$

and

$$\hat{\phi}_2(\xi, x_3) = \frac{i}{2\lambda_-} \int_{-\infty}^{0} h_2(\xi, x_3, y_3)\hat{\psi}(\xi, y_3)dy_3. \qquad (A2.16)$$

Differentiation of ϕ_2 with respect to x_3 gives

$$\frac{\partial\hat{\phi}_2(\xi, x_3)}{\partial x_3} = \frac{i}{2}e^{-i\lambda_- x_3} \int_{-\infty}^{0} e^{-i\lambda_- y_3}\hat{\psi}(\xi, y_3)dy_3; \qquad (A2.17)$$

since both exponentials in this expression are decaying, we have

$$\|\frac{\partial\hat{\phi}_2(\xi, \cdot)}{\partial x_3}\|^2_{L^2(\mathbf{R}_-)} \leq c\|\hat{\psi}(\xi, \cdot)\|^2_{L^2(\mathbf{R}_-)}.$$

Using the Plancherel theorem and integrating over x_1 and x_2 then shows that

$$\|\partial\phi_2/\partial x_3\|_{L^2(\mathbf{R}^3_-)} \leq c\|\psi\|_{L^2(\mathbf{R}^3_-)}.$$

Differentiation of ϕ_1 with respect to x_3 gives

$$\frac{\partial\hat{\phi}_1(\xi, x_3)}{\partial x_3} = \frac{i}{2} \int_{-\infty}^{0} \mathrm{sgn}(x_3 - y_3)e^{i\lambda_-|x_3 - y_3|}\hat{\psi}(\xi, y_3)dy_3 \qquad (A2.18)$$

We extend $\hat{\psi}$ to the whole real line by defining it to be zero for $y_3 > 0$. This allows us to extend the region of integration on the right side of (A2.18) to the whole real line, so that the right side becomes a convolution. We then Fourier transform in the x_3 variable, obtaining

$$\hat{\Phi}(\xi, \eta) = \frac{2i(\alpha - \eta)}{\beta^2 + (\eta - \alpha)^2}\hat{\Psi}(\xi, \eta), \qquad (A2.19)$$

where $\hat{\Phi}$ and $\hat{\Psi}$ are the one-dimensional Fourier transforms of $\partial\hat{\phi}_1/\partial x_3$ and $\hat{\psi}$, respectively, and where we have have used $\alpha = \alpha(\xi)$ and $\beta = \beta(\xi)$ for the respective real and imaginary parts of λ_-. Taking L^2 norms of both sides of (A2.19), in the η variable, we see that $\|\hat{\Phi}(\xi, \cdot)\|_{L^2(\mathbf{R}_-)} \leq c\|\hat{\Psi}(\xi, \cdot)\|_{L^2(\mathbf{R}_-)}$. Using the Plancherel theorem and integrating over x_1 and x_2 then shows that

$$\|\frac{\partial\phi_1}{\partial x_3}\|_{L^2(\mathbf{R}^3_-)} \leq c\|\psi\|_{L^2(\mathbf{R}^3_-)}. \qquad (A2.20)$$

QED

Proposition A2.2. If m is strictly positive, equation (A2.13) has a unique solution in $H^1(\mathbf{R}^3_-)$.

Proof. The Fredholm alternative guarantees that (A2.13) has a unique solution provided that the corresponding homogeneous equation has only the zero solution. A solution of the homogeneous equation is also a solution u of (2.4) and (2.5) with $f = 0$. To show that such a u must be identically zero, we use an energy argument. The procedure for obtaining this energy identity is to multiply (2.4) by the complex conjugate $\bar{u}$ and integrate over C_h, a cylindrical region with radius $|x'| = h^2$ and extending from $x_3 = 0$ to $x_3 = -h$. After using Green's theorem, we obtain

$$\int_{C_h} (|\nabla u|^2 - q|u|^2) = \int_{\partial C_h} \bar{u} \frac{\partial u}{\partial \nu}, \qquad (A2.21)$$

where ν is the outward unit normal to C_h.

The right side of (A2.21) has three parts, corresponding to the parts of the boundary of C_h. The integral over the circle on the plane $x_3 = 0$ contributes nothing because u is zero there. Similarly, the integral over the circle on the plane $x_3 = -h$ goes to zero in the limit $h \to \infty$ because of the radiation condition in the lower half-plane. The integral over the side of the cylinder also vanishes because of the large-ρ asymptotics of u. Thus the right side of (A2.21) vanishes as $h \to \infty$. Thus, in the limit, we have

$$\int_{x_3<0} (|\nabla u|^2 - q|u|^2) dx = 0. \qquad (A2.22)$$

Both the real and imaginary parts of the left side of (A2.22) must be zero; since for k positive, q has positive imaginary part km, $|u|$ must be zero.

QED

As discussed in Appendix 1, the hypothesis that m be strictly positive can be replaced by smoothness assumptions on n^2 and m.

APPENDIX 3. PROPERTIES OF THE SCATTERING OPERATOR

In Appendix 1 we saw that an incident field in $H^{1,-s}(\mathbf{R}^3)$, $s > 1/2$, gives rise to a scattered field in the same space. Because these spaces are weighted only in the x_3 variable, the restriction of a function in such a space to any horizontal (i.e., fixed x_3) plane is in $H^{1/2}(\mathbf{R}^2)$ [Ad]. The Fourier transform of this space is

$$L^2_{1/2}(\mathbf{R}^2) = \{u(\xi) : (1 + |\xi|^2)^{1/4} u \in L^2(\mathbf{R}^2)\}.$$

Thus the operator $\hat{S}$ maps $L^2_{1/2}(\mathbf{R}^2)$ to itself.

With this information, equation (3.3) can be interpreted as follows. Since both $\hat{\Lambda}$ and multiplication by $i\lambda_+$ are maps from $L^2_{1/2}$ to $L^2_{-1/2}$, each side of equation (3.3) is a map on $L^2_{1/2}$ followed by a map from $L^2_{1/2}$ to $L^2_{-1/2}$.

Theorem. The projection $P\hat{S}P$ of the scattering operator onto $\{f : (k^2 - |\xi|^2)^{1/4} f \in L^2(|\xi| < k)$ has norm less than one.

Proof. We use the energy identity (A1.24) applied to a region that in the limit becomes the entire lower half-space. In the right side we use expression (A1.25), where, on the surface $x_3 = 0$,

$$\hat{\psi}(\xi, 0) = (\hat{S}f)(\xi) + f(\xi). \qquad (A3.1)$$

The energy identity thus becomes

$$(2\pi)^2 \int_{x_3<0} (|\nabla\psi|^2 - k^2 n^2 |\psi|^2 - ikm|\psi|^2) =$$
$$i \int_{|\xi|<k} \left[(|\hat{S}f(\xi)|^2 - |f(\xi)|^2) + 2iIm(\bar{f}\hat{S}f) \right] \sqrt{k^2 - |\xi|^2} d\xi - \qquad (A3.2)$$
$$\int_{|\xi|>k} \left[(|\hat{S}f(\xi)|^2 - |f(\xi)|^2) + 2iIm(\bar{f}\hat{S}f) \right] \sqrt{|\xi|^2 - k^2} d\xi.$$

Here we assume that f is zero for $|\xi| > k$. Thus the right side of (A3.2) reduces to

$$i \int_{|\xi|<k} \left[(|\hat{S}f(\xi)|^2 - |f(\xi)|^2) + 2iIm(\bar{f}\hat{S}f) \right] \sqrt{k^2 - |\xi|^2} d\xi - \int_{|\xi|>k} |\hat{S}f(\xi)|^2 \sqrt{|\xi|^2 - k^2} d\xi. \qquad (A3.3)$$

The imaginary part of the expression is $\int_{|\xi|<k} (|\hat{S}f(\xi)|^2 - |f(\xi)|^2) d\xi$, which must be negative since the left side of (A3.2) is negative.

QED

ACKNOWLEDGMENTS

This work was supported in part by the Office of Naval Research grant N00014-93-1-0048, by the National Science Foundation Faculty Award for Women in Science and Engineering DMS 9023630, by Rensselaer Polytechnic Institute, and by the Institute for Mathematics and Its Applications at the University of Minnesota. We are grateful to Dale Winebrenner for sending us his notes on the TE and TM polarizations, to Julian Cole for suggesting the use of polar coordinates in (A2.8), and to John Sylvester for sending us copies of [Chj] and [M].

REFERENCES

[A] G. Arfken, Mathematical Methods for Physicists, Academic Press, New York, 1985.

[Ad] R.A. Adams, Sobolev Spaces, Academic Press, New York, 1975.

[Ag] S. Agmon, "Spectral properties of Schrödinger operators and scattering theory", Annali della Scuola Normale Superiore di Pisa, Classe di Scienze, serie IV, vol. II, 2 (1975) 151–218.

[BLK] A. M. Bruckstein, B. C. Levy, and T. Kailath, "Differential methods in inverse scattering", SIAM J. Appl. Math. 45 (1985) 312–335.

[C] M. Cheney, "Stability analysis of the Yagle-Levy multidimensional inverse scattering algorithm", J. Math. Phys. 31 (1990) 2141–2144.

[Ca] F. D. Carsey, ed., Microwave Remote Sensing of Sea Ice, Geophysical Monograph 68, American Geophysical Union, 1992.

[CB] B.J. Chaderjian and K. Bube, "Recovery of perturbations in an acoustic medium with attenuation from several plane wave responses", SIAM J. Appl. Math. 53 (1993) 829–846.

[CH] R. Courant and D. Hilbert, Methods of Mathematical Physics, vol. 2, Wiley, NY, 1962.

[Ch] Y. Chen, "On the inverse scattering problem for the Helmholtz equation in one dimension", Yale University Research Report YALEU/DCS/RR-913, 1992.

[Chj] B.J. Chaderjian, "Determination of a stratified acoustic medium with attenuation from its response to a point source", Ph.D. Dissertation, UCLA, 1989; "A uniqueness theorem for a lossy inverse problem in reflection seismology", SIAM J. Appl. Math. 54 (1994) 1224–1249 .

[CK] M. Cheney and G. Kristensson, "Three-dimensional inverse scattering: layer-stripping formulae and ill-posedness results", Inverse Problems 4 (1988) 625–642.

[CDK] J. P. Corones, M. E. Davison, and R. J. Krueger, "Direct and inverse scattering in the time domain via invariant imbedding equations", J. Acoust. Soc. Am. 74 (1983) 1535–1541.

[D] J.W. Dettman, Applied Complex Variables, Dover, New York, 1965.

[DG] Y. Dermenjian and J.C. Guillot, "Scattering of elastic waves in a perturbed isotropic half space with a free boundary. The limiting absorption principle", Math. Meth. in the Appl. Sci. 10, 87-124 (1988); "Théorie spectrale de la propagation des ondes acoustiques dans un milieu statifié perturbé", J. Diff. Eq. 62 (1986) 357–409.

[DH] M. DeHoop, 'Invariant imbedding in laterally varying, anisotropic media: an admittance operator approach', preprint, 1995.

[E] C. Elachi, Spaceborne Radar Remote Sensing: Applications and Techniques, IEEE Press, New York, 1988.

[GX] R. Gilbert and Y. Xu, "Generalized Herglotz functions and inverse scattering problem in a finite depth ocean", in Invariant Imbedding and Inverse Problems, ed. J. Corones, G. Kristensson, P. Nelson, and D. Seth, SIAM Proceedings in Applied Mathematics 63, Philadelphia, 1992.

[J] J.D. Jackson, Classical Electrodynamics, 2nd Ed., Wiley, New York, 1975.

[Jz] K. Jezek, "Laboratory Studies of Electromagnetic Properties of Saline Ice", Office of Naval Research Report, available from Goldthwait Polar Library, Byrd Polar Research Center, Ohio State Univ.

[KK] G. Kristensson and R.J. Krueger, "Direct and inverse scattering in the time domain for a dissipative wave equation, Part 4", Inverse Problems 5 (1989) 375–388.

[KV] R. Kohn and M. Vogelius, "Determining conductivity by boundary measurements", Comm. Pure Appl. Math. 37 (1984) 113–123.

[LP] P.D. Lax and R.S. Phillips, "Scattering theory for dissipative hyperbolic systems", J. Functional Analysis 14 (1973) 172–235.

[LU] J. Lee and G. Uhlmann, "Determining anisotropic real analytic conductivities by boundary measurements", Comm. Pure Appl. Math. 42 (1989) 1097–1112.

[M] N. J. Marechal, "Inverse problems for lossy hyperbolic equations", Ph.D. dissertation, UCLA, 1986.

[N] A. Nachman, "Reconstructions from boundary measurements," *Annals of Math.* **128** (1988), pp. 531-556.

[OPS] P. Ola, L. Päivärinta, and E. Somersalo, "An inverse boundary value problem in electrodynamics", Duke Math. J. 70 (1993) 617–653.

[OS] A.V. Oppenheim and R.W. Schafer, Digital Signal Processing, Prentice-Hall, Englewood Cliffs, NJ (1975).

[PSS] "Inverse Problems of Acoustic and Elastic Waves" by Yih-Hsing Pao, Fadil Santosa and William W. Symes, in Inverse Problems of Acoustic and Elastic Waves, Editors:Fadil Santosa, William W. Symes and Charles Holland, SIAM,Philadelphia, 1984, pp.274-302

[RS4] M. Reed and B. Simon, Methods of Modern Mathematical Physics, IV. Analysis of Operators, Academic Press, New York, 1978.

[S] M. Schecter, Spectra of Partial Differential Operators, 2nd ed., North-Holland, New York, 1986.

[Sm] E. Somersalo, "Layer stripping for time-harmonic Maxwell's equations with fixed frequency", Inverse Problems 10 (1994) 449–466.

[SCII] E. Somersalo, M. Cheney, D. Isaacson, and E. Isaacson, "Layer Stripping: A Direct Numerical Method for Impedance Imaging," Inverse Problems, 7 (1991) 899–926 ; 8 (1992), 493.

[SU] J. Sylvester and G. Uhlmann, "A uniqueness theorem for an inverse boundary value problem in electrical prospection", Comm. Pure Appl. Math. 39 (1986) 91-112; "A global uniqueness theorem for an inverse boundary value problem in electrical prospection", Ann. of Math., 125 (1987) 153-169; "Inverse boundary value problems at the boundary—continuous dependence", Comm. Pure Appl. Math. 41 (1988) 197–221.

[SU2] J. Sylvester and G. Uhlmann, "Inverse problems in anisotropic media", in Inverse Scattering and Applications, ed. D.H. Sattinger, C.A. Tracy, and S. Venakides, Contemporary Mathematics vol. 122, Am. Math. Soc., Providence, RI (1991).

[Sym] W. W. Symes, "On the relation between coefficient and boundary values for solutions of Webster's horn equation", SIAM J. Appl. Math. Anal. 17 (1986) 1400–1420.

[Syl] J. Sylvester, "A convergent layer stripping algorithm for the radially symmetric impedance tomography problem", to appear, Comm. Partial Diff. Eqs.

[SWG] J. Sylvester, D. Winebrenner, and F. Gylys-Colwell, "Layer stripping for the Helmholtz equation", preprint.

[T] F. Treves, Basic Linear Partial Differential Equations, Academic Press, New York, 1975.

[To] D. H. Towne, Wave Phenomena, Addison-Wesley, Palo Alto, 1967.

[TKS] L. Tsang, J.A. Kong, and R.T. Shin, Theory of Microwave Remote Sensing, Wiley, New York, 1985.

[W] V.H. Weston, "Invariant imbedding for the wave equation in three dimensions and applications to the direct and inverse problems", Inverse Problems 6 (1990) 1075; "Wave splitting and the reflection operator for the wave equation in $\mathbf{R}^3$", J. Math. Phys. 30 (1989) 2545.

[We] R. Weder, Spectral and Scattering Theory for Wave Propagation in Perturbed Stratified Media, Springer, New York, 1991.

[Wi] C. Wilcox, Sound Propagation in Stratified Fluids, Springer, New York, 1984.

[Xu] Y. Xu, "Scattering of acoustic wave by obstacle in stratified medium", in Partial Differential Equations with Real Analysis, ed. H. Begehr and A. Jeffrey, Pitman Research Notes in Mathematics Series 263, Longman Sc. &Tech., Essex, UK (1992) 147-168.

[YL] A. Yagle and B. Levy, "Layer stripping solutions of multidimensional inverse scattering problems", J. Math. Phys., 27 (1986) 1701–1720.

Imaging in Optical Turbid Media with Diffusive Waves of Light

Arjun G. Yodh
Department of Physics and Astronomy
University of Pennsylvania
Philadelphia, PA 19104-6396

Visually opaque media are ubiquitous in nature. While some materials are opaque because they strongly absorb visible light, others such as tissue may be opaque because photons traveling within these media are predominantly scattered rather than absorbed. A vanishingly small number of photons travel straight through such substances: instead, light is transported through these materials in a process similar to heat diffusion. In the biophysics and medical communities, diffusing photons are now used to view body function and structure [1]. This is a result of a spectral window within tissues in the 700-900 nm region, in which photon transport is dominated by scattering rather than absorption. Thus, to a very good approximation, near infrared photons diffuse through human tissues. The use of light to create images of turbid media is an attractive idea whose roots can be traced to diaphonagraphy [2]. There have been many developments since then that make the possibilities of light-based images of turbid media eminently realistic at the present time [1]. On the technological side, the development of small and efficient light sources, detectors, and control electronics, along with the continual improvements in computational capabilities, make possible rapid, repeatable, and sensitive noninvasive optical instruments. On the fundamental side, as a result of advances in our understanding of photon and correlation transport, particularly with regard to their connection to material properties, we are now able to consider these problems with unprecedented theoretical sophistication and clarity. Light offers new image contrast specificities that distinguish it from other techniques such as X-Ray, magnetic resonance, thermography, and sound. Spectroscopic information is available as a result of the intrinsic absorption's of the materials probed, or as a result of the absorption of contrast agents (chemicals) that may be introduced externally into the system. Spectroscopic and lifetime information from fluorophores (intrinsic or extrinsic) can provide sensitive information about local environments in the turbid media. Furthermore recent work [3] suggests that information about

the higher order diffusing light field correlation functions such its temporal correlations, appear capable of providing maps of motions within turbid media. In this contribution I will discuss results from my laboratory wherein we use diffusing light to probe turbid media. The elementary disturbances we use are generated by point sources of light, whose amplitudes are modulated sinusoidally at angular frequency w. Microscopically, individual photons undergo a random walk within the medium, but collectively, a spherical wave of photon density is produced and propagates outward from the source. We refer to these waves as diffuse photon density waves (DPDWUs) or diffusive waves. There are a variety of ways to generate diffuse photon-density-waves [4-8]. Typically amplitude modulated light is delivered into the turbid sample through a source fiber optic cable, and the scattered photons are collected through a detector fiber optic cable. The source radiation is derived from a diode laser, LED, or more complex laser system. The oscillating portion of the detected diffuse light-energy-density is separated from all other light by standard phase-sensitive methods. Both the phase and amplitude of the diffuse photon-density-wave can be determined in this way. Although these waves are overdamped, it is feasible to utilize them as probes of biological samples whose extent is of the order of 10 cm, or about 100 transport mean free pathlengths. The measurements will necessarily be in the near field of the diffuse photon-density-wave, but analogies from optics are often useful as a guide to understand the variation of the amplitude and phase of the diffuse photon-density-waves brought about by absorption and scattering changes within the sample. For example, the diffusive waves have been observed to exhibit other properties one normally associates with conventional electromagnetic radiation such as refraction [6], diffraction [7,9], interference [5,7], and dispersion [8]. Contrast in these cases is brought about by variations in absorption and scattering which combine to produce effective dielectric constants for the diffusive waves. Our earliest experiments we aimed to elucidate the physical properties of these disturbances, demonstrating the refraction [6], diffraction [7,9], and fluorescent reemission [7] of these waves. The focus of the present talk however, will be on research we have done more recently that is more oriented towards the application of these probes for imaging purposes. In particular we will describe experiments that demonstrate the tomographic reconstruction of absorptive and scattering heterogneieties in tissue phantoms [10]. We will indicate how to reconstruct lifetime and con-

centration of fluorophores in tissues using secondary, reradiated DPDWUs [11], and we will discuss our experiments with diffusing temporal correlation in heterogeneous fluctuating media [3]. Finally we explicitly consider the scattering of diffusive waves from small spherical heterogneities (absorbing, scattering, and fluorescing [12]), analyzing the limits of detection and characterization with diffusive waves [13] in real systems.

References

1. A. Yodh and B. Chance, Physics Today , Volume 48, No. 3, 34-40 (1995) and references therein.

2. Kaneko et al, Radiation Medicine 6, 61 (1988) and references therein.

3. D.A. Boas, L. Campbell, and A.G. Yodh, Physical Review Letters 75, 1855-58 (1995).

4. E. Gratton, W. Mantulin, M. J. van de Ven, J. Fishkin, M. Maris, and B. Chance, in Proceedings of The Third International Conference: Peace through Mind/Brain Science, August 5-10, 1990, Hamamatsu, Japan, p. 183; J. Fishkin and E. Gratton, J. Opt. Soc. Am. A 10, 127 (1993).

5. J. M. Schmitt, A. Knuttel, and J. R. Knudsen, J. Opt. Soc. Am. A 9, 1832 (1992); A. Knuttel, J.M. Schmitt, and J. R. Knutson, Appl. Opt. 32, 381 (1993); A. Knuttel, J.M. Shmitt, R.Barnes, and J.R. Knutson, Rev. Sci. Instr. 46, 638 (1993).

6. M.A. O'Leary, D.A. Boas, B. Chance, and A.G. Yodh, Phys. Rev. Lett. 69, 2658 (1992).

7. D.A. Boas, M.A. O'Leary, B. Chance, and A.G. Yodh, Phys. Rev. E 47, R2999 (1993); M.A. O'Leary, D.A. Boas, B. Chance, and A.G. Yodh, Journ. of Luminescience 60-61, 281 (1994).

8. B.J. Tromberg, L. O. Svaasand, T.T. Tsay, and R.C. Haskell, Appl. Opt. 32, 607 (1993); E.M. Sevick, J. Lakowicz, H. Szmacinski, K. Nowacyzk, and M.L. Johnson, J. Photochem. Photobiol. B 16, 169 (1992).

9. D.A. Boas, M.A. O'Leary, B. Chance, and A.G. Yodh, Proc. Nat. Aca. Sci. USA 91, 4887 (1994); similar calculations and measurements for small objects and cw sources is found in P.N. den Outer, Th. M. Nieuwenhuizen, and A. Lagendijk, J. Opt. Soc. Am. A 10, 1209 (1993).

10. M.A. O'Leary, D.A. Boas, B. Chance, and A.G. Yodh, Optics Letters 20, 426 (1995).

11. M.A. OULeary, D.A. Boas, X. Li, B. Chance, and A.G. Yodh, Optics Letters 21, 158-60 (1996).

12. X. Li, M.A. OULeary, D.A. Boas, B. Chance, and A.G. Yodh, to be published July 1, 1996 Applied Optics.

13. D.A. Boas, M.A. OULeary, B. Chance, and A.G. Yodh, submitted to Journal of Optical Society A (1996).

Electromagnetic Wave Scattering from a Body Buried Near a Random Rough Surface

A. Madrazo and M. Nieto-Vesperinas
Instituto de Ciencia de Materiales,
Consejo Superior de Investigaciones Cientificas,
Campus de Cantoblanco. Madrid 28049. Spain.

Abstract

By using the extinction theorem for multiply connected scattering domains[1], we perform numerical calculations on the scattering of light and other electromagnetic waves by a $2-D$ system consisting of a cylinder behind a very rough random dielectric surface. Recently, the above configuration is receiving increasing interest due to the possibility of detecting hidden bodies behind rough surfaces[2, 3, 4].

It is shown that the presence of a small body buried behind a random surface dramatically enhances the backscattering peak effect, even for surfaces that do not exhibit a backscattering peak in the absence of the cylinder. In order for this to occur, the surface must be very rough, and the dielectric contrast between the body and the medium in which it is inmersed has to be appreciable.

Results of numerical calculations on the dependence of the backscattering peak on the cylinder-surface distance are shown. Also, the influence of others parameters such as the incident polarization, cylinder size, and angle of incidence is discussed.

References

[1] A. Madrazo and M. Nieto-Vesperinas, J. Opt. Soc. Am. A **12**, 1298 (1995).

[2] L. Tsang, G. Zhang and K. Pak, Microwave and Optical Technology Letters **11**, 300 (1996).

[3] L. Wang, P.P. Ho, C. Liu, G. Zhang and R.R. Alfano, Science **253**, 769 (1991).

[4] S.K. Gayen and R.R. Alfano, Optics and Photonics News **7:3**, 17 (1996).

Scattering of Infrared Radiation by Heterogeneous Medium under a Rough Surface

L. Hespel, D. Boutin, S. Mainguy and B. Capbern
Centre d'Etudes Scientifiques et Techniques d'Aquitaine
Commissariat á l'Energie Atomique
BP 2, 33114 Le Barp - FRANCE

We present in this paper the optical scattering of a rough semi-transparent heterogeneous medium. The goal of this work is to study the behavior of a paint deposited on an absorbing or reflective structure and to evaluate, in the scattering diagram, the contribution of the roughness.

To calculate the scattered field we use a phenomenological equation of radiation transfer solved with a discrete ordinate method which allows us to model the propagation of both the collimated component (coherent) and the diffuse component (incoherent) of the light. We take into account the scattering radiation from the rough surface by a boundary condition. The scattered and transmitted fields are calculated with a numerical simulation based on a Rayleigh hypothesis and the extinction theorem (the iterative series solutions introduced by J. J. Greffet: DIFF3D code).

We shall present the coupling method, the first results, and an analytical study that fits the relevant parameters of the physical problem.

The Stokes Matrix in Conical Scattering From One-Dimensional Perfectly Conducting Random Surfaces

A. A. Maradudin and I. V. Novikov

Department of Physics and Astronomy

and Institute for Surface and Interface Science

University of California

Irvine, CA 92717, U.S.A.

E. R. Méndez

División de Fisica Aplicada

Centro de Investigación Superior de Ensenada

Apartado Postal 2732

Ensenada, Baja California 22800, Mexico

If, in the scattering of electromagnetic waves from a one-dimensional, randomly rough surface, the plane of incidence is not perpendicular to the generators of the surface, the diffuse scattering of the electromagnetic waves that occurs in this case is called *conical scattering*, because the scattered radiation appears on the surface of a cone, rather than in a plane, due to the translational invariance of the scattering surface parallel to its generators. In this work we have determined formally the elements of the Stokes matrix describing such scattering in terms of the second-order moments of the scattered field for the scattering of a Guassian beam from a one-dimensional perfectly conducting random surface, defined by the equation $x_3 = \zeta(x_1)$. The surface profile function $\zeta(x_1)$ is assumed to be a single-valued function of x_1 that constitutes a zero-mean, stationary, Gaussian random process, characterized by a Gaussian surface height autocorrelation function. The region $x_3 > \zeta(x_1)$ is vacuum, while the region $x_3 < \zeta(x_1)$ is a perfect conductor. In obtaining expressions for the elements of the Stokes matrix we have used the geometry adopted by Luna and Méndez [1] in their experimental study of conical scattering. In this geometry the plane of incidence is defined by the wave vector of the incident electromagnetic field and the unit vector parallel to the generators of the surface. The plane of scattering is defined in an analogous fashion. This contrasts with the usual definitions of these planes, viz. that

they are defined by the wave vectors of the incident and scattered electromagnetic fields and the normal to the mean scattering plane, respectively. If we write the components of the electric and magnetic fields in the vacuum region in the forms $E_\alpha^>(\vec{x};t) = \hat{E}_\alpha(x_1, x_3|\omega)$ $\times \exp(ik_2x_2 - i\omega t)$ and $H_\alpha^>(\vec{x};t) = \hat{H}_\alpha(x_1, x_3|\omega)\exp(ik_2x_2 - i\omega t)$, respectively, the components parallel to the generators of the surface, $\hat{E}_2(x_1, x_3|\omega)$ and $\hat{H}_2(x_1, x_3|\omega)$, satisfy the Helmholtz equations

$$\left[\frac{\partial^2}{\partial x_1^2} + \frac{\partial^2}{\partial x_3^2} + \left(\frac{\omega^2}{c^2} - k_2^2\right)\right] \left\{ \begin{array}{c} \hat{E}_2(x_1, x_3) \\ \hat{H}_2(x_1, x_3) \end{array} \right\} = 0.$$

The remaining four field components are all obtained by differentiating $\hat{E}_2(x_1, x_3|\omega)$ and $\hat{H}_2(x_1, x_3|\omega)$. By applying Green's second integral identity to the vacuum region $x_3 > \zeta(x_1)$, we obtain the inhomogeneous integral equations satisfied by the values of $(-\zeta'(x_1)(\partial/\partial x_1) + (\partial/\partial x_3))\ \hat{E}_2(x_1, x_3|\omega)$ and $\hat{H}_2(x_1, x_3|\omega)$ on the random surface, in terms of which all components of the scattered electromagnetic field can be expressed. These equations are solved numerically for each of 1000 realizations of the surface profile function [2], and the elements of the Stokes matrix are averaged over the results obtained for these realizations. For the scattering geometry assumed in the present work, we obtain the same nonzero elements of the Stokes matrix as in an earlier determination of these elements in the case that the plane of incidence was assumed to be perpendicular to the generators of a one-dimensional random surface [3], although, of course, the expressions for the elements are different in the two cases. We have calculated the nonzero elements of the Stokes matrix and have plotted the contributions to them from the coherent (specular) and incoherent (diffuse) components of the scattered light. The results of this study provide complete information about the scattering properties of one-dimensional randomly rough surfaces.

[1] R. E. Luna and E. R. Méndez, Optics Lett. **20**, 657 (1995).

[2] A. A. Maradudin, T. Michel, A. R. McGurn, and E. R. Méndez, Ann. Phys. (N.Y.) **203**, 255 (1990).

[3] T. R. Michel, M. E. Knotts, and K. A. O'Donnell, J. Opt. Soc. Am. A**9**, 585 (1992).